

## THÈSE

Pour obtenir le grade de

### DOCTEUR DE L'UNIVERSITÉ GRENOBLE ALPES

École doctorale : CSV- Chimie et Sciences du Vivant

Spécialité : Biologie Structurale et Nanobiologie

Unité de recherche : Institut de Biologie Structurale

## Outils et méthodes pour la visualisation interactive et l'analyse des assemblages biologiques supramoléculaires par cryo-ET : une étude de cas sur *Deinococcus radiodurans*

## Tools and methods for interactive visualization and analysis of superstructural biological assemblies by cryo-ET: a *Deinococcus radiodurans* case study.

Présentée par :

**Lorenzo GAIFAS**

### Direction de thèse :

**Irina GUTSCHE**  
CNRS

Directrice de thèse

**Joanna TIMMINS**  
DIRECTRICE DE RECHERCHE, CNRS

Co-directrice de thèse

### Rapporteurs :

**Slavica JONIC**  
DIRECTRICE DE RECHERCHE, CNRS délégation Paris Centre

**Charles KEVRANN**  
DIRECTEUR DE RECHERCHE, CNRS délégation Bretagne et Pays de la Loire

Thèse soutenue publiquement le **24 octobre 2024**, devant le jury composé de :

**Marc JAMIN**,  
PROFESSEUR DES UNIVERSITES, Université Grenoble Alpes

Président

**Irina GUTSCHE**,  
DIRECTRICE DE RECHERCHE, CNRS délégation Alpes

Directrice de thèse

**Slavica JONIC**,  
DIRECTRICE DE RECHERCHE, CNRS délégation Paris Centre

Rapporteure

**Charles KEVRANN**,  
DIRECTEUR DE RECHERCHE, CNRS délégation Bretagne et Pays de la Loire

Rapporteur

**Gabor PAPAI**,  
CHARGE DE RECHERCHE HDR, CNRS délégation Alsace

Examinateur

**Leandro FARIAS ESTROZI**,  
CHARGE DE RECHERCHE, CNRS délégation Alpes

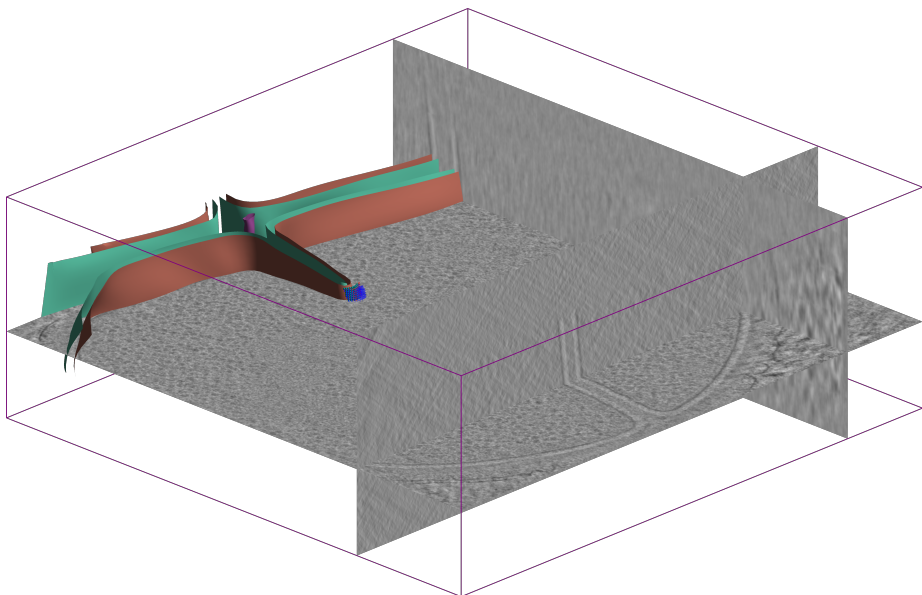
Examinateur

### Invités :

**Joanna TIMMINS**  
DIRECTRICE DE RECHERCHE, CNRS Alpes

# **Tools and methods for interactive visualization and analysis of superstructural biological assemblies by cryo-ET**

a *Deinococcus radiodurans* case study



**Lorenzo Gaifas**

directed by Irina Gutsche and Joanna Timmins

**November 8, 2024**

Université de Grenoble Alpes — Institute de Biologie Structurale

### III

The place they go towards is a place even less imaginable  
to most of us than the city of happiness. I cannot  
describe it at all. It is possible that it does not exist.  
But they seem to know where they are going,  
the ones who walk away from Omelas.

---

*The ones who walk away from Omelas*

— Ursula K. Le Guin

## Abstract

Cryo-electron tomography (cryo-ET) is an imaging technique that allows to reconstruct the three-dimensional volume of whole biological samples — such as cells and tissues — *in situ*, in near-native conditions and within their biological context. With the development of direct electron detectors and increased computing power, in recent years cryo-ET has rapidly become a powerful and ubiquitous tool in the arsenals of structural biologists, sometimes capable of reaching sub-nanometer resolution. Due to the yet immature software ecosystem and the complexity of the workflows, working with cryo-ET data is still error-prone and requires constant human supervision, especially when it comes to subtomogram averaging pipelines attempting to reach high resolution reconstructions. This thesis presents the development of blik, a tool aimed at simplifying working with cryo-ET data by providing interactive visualisation, analysis and annotation that are both powerful and customizable, with a focus on the analysis of superstructural systems such as filaments and membranes. Using blik and other tools, we investigate the cell wall composition and septation mechanism in the radiation resistant bacterium *Deinococcus radiodurans*, and study the structure and role of FtsZ, a tubulin homologue which plays a key role in cell division.

## Keywords

Cryo-electron tomography, superstructure, blik, *D. radiodurans*, FtsZ

## Résumé

La tomographie cryo-électronique (cryo-ET) est une technique d'imagerie qui permet de reconstruire le volume tridimensionnel d'échantillons biologiques entiers — tels que les cellules et les tissus — *in situ*, dans des conditions proches de l'état natif et dans leur contexte biologique. Avec le développement de détecteurs directs d'électrons et l'augmentation de la puissance de calcul des ordinateurs, la cryo-ET est rapidement devenue, ces dernières années, un outil puissant et omniprésent dans l'arsenal des biologistes structuraux, parfois capable d'atteindre une résolution sous-nanométrique. En raison de l'écosystème logiciel encore immature et de la complexité des flux de travail, travailler avec des données cryo-ET est encore sujet à des erreurs et nécessite une supervision humaine constante, en particulier lorsqu'il s'agit de pipelines de moyennation de sous-tomogrammes qui visent à atteindre des reconstructions à haute résolution. Cette thèse présente le développement de blik, un outil conçu pour simplifier le travail sur les données cryo-ET en fournissant une visualisation interactive, une analyse et une annotation qui sont à la fois puissantes et personnalisables, en se concentrant sur l'analyse d'assemblages supramoléculaires tels que les filaments et les membranes. En utilisant blik et d'autres outils, nous examinons la composition de la paroi cellulaire et le mécanisme de septation chez *Deinococcus radiodurans*, une bactérie résistante particulièrement aux radiations , et nous étudions la structure et le rôle de FtsZ, un homologue de la tubuline qui joue un rôle clé dans la division cellulaire.

## Mots clés

Tomographie cryo-électronique, superstructure, blik, *D. radiodurans*, FtsZ

# Acknowledgements

This manuscript and my journey as a PhD student wouldn't have been the same without the steady presence and contribution of many wonderful people.

I'm extremely grateful to the members of my jury — Slavica Jonic, Charles Kervrann, Gabor Papai, Leandro Estrozi, and Marc Jamin — for offering their time and expertise in reading this manuscript and for the following discussion at the thesis defense.

Many thanks to GRAL for providing the funding and resources that gave me a smooth PhD experience. In particular, heartfelt thanks to Anne-Mathilde Thierry for her rare ability to make interactions with the cumbersome french bureaucracy quick and pleasant.

There are many people I have worked with and learned from, at IBS and outside, that have helped me during these years.

My most heartfelt thanks go to my supervisors Irina and Joanna. I'm truly grateful for your continued support towards my independence and self-determination, all while managing to direct my (admittedly often unfocused) efforts towards useful goals. I was incredibly lucky to work with scientists who so value collaboration, curiosity, open discussion, and good scientific and work ethic. You created a stimulating and friendly environment that I will forever crave going forward.

I'm deeply indebted to Alister, for his inexhaustible willingness to share knowledge, for the long discussions on software design, and for giving me a head-start in the world of Cryo-ET. Thank you also for introducing me to

the napari community, which so much shaped the next few years of both of our careers.

Special thanks to Leandro, for being always ready to explain and re-explain complex image processing topics, and for easily sharing his no-nonsense yet lighthearted attitude towards pretty much anything.

Thanks Ambroise, for all the technical discussions on cryo-EM processing and its nuances, especially regarding helical assemblies, and for the occasional evening party.

Many thanks also to the MICA and GenOM teams for performing many of the experiments and data collections that contributed to this thesis; I couldn't have done this without you!

I also had great pleasure working with Linda Sandblad and everyone else at the Centre for Electron Microscopy in Umeå. I had a great time there, doing both lots of science and sport with such a friendly group!

I'm extremely grateful to everyone in the napari community — particularly the core developers, with whom I worked closely by now for several years. You've been an endless source of new ideas and of personal growth both as a developer and as a scientist. I look forward to continue working with you.

My deepest thanks to everyone who loves me and shared these last few years with me.

A big thanks to my parents Tiziana and Giancarlo and my sister Valentina, who always encouraged my studies unconditionally — even when I suddenly chose to move abroad and through any financial challenges — and who remain unwaveringly supportive of who I am and of everything I do.

Thanks to Moritz for always joining in and enabling my unnecessary pedantry, and for readily accepting to be my first test subject whenever I developed something new.

Thank you Alessio, for always preventing me from indulging in too much unnecessary pedantry, and for readily accepting to be my first test subject whenever I developed something new.

Thanks to Eymeline, for all that we shared at work and outside, and for showing me a plethora of new shiny nerdy things I didn't know about. Thank you for being so stubbornly selfless with everyone around you.

Thank you Paco, for being my trusty board games companion, even when you're exhausted from work. Thanks for being always openhearted, and for unfailingly joining me in the fight against the System.

Thanks Lorene, for all the philosophical discussions and for the good times in Grenoble and Umeå. I'm constantly inspired by your hard work and determination, all while maintaining a relaxed attitude that makes it easy to be around you.

Thank you Jahnavi, for the always thoughtful gifts and for being a steady, quiet and friendly presence in the office. Good luck with finishing up!

Thank you Maaike, for always showing me by example how to have a more positive impact on the world and the people around me, and for navigating uncharted territories with me.

Thanks to all my friends back in Rovereto, for providing a safe haven at the Stube whenever I needed to take a break and unwind while playing games and eating pizza.

Thank you all!

# Preface

This thesis is the result of interdisciplinary work at the interface of computer science, image processing, structural biology and microbiology. The primary driving force of this work has been the development of open-source, user-friendly and reusable data analysis and visualization software for the cryo-electron microscopy community and the scientific image community at large. The tools and software developed during my thesis stemmed from the need to overcome the various challenges encountered while working on the several structural biology projects I undertook or contributed to, mostly involving cryo-electron tomography data.

Coming from a master's degree specialized in molecular dynamics, I was often faced with the problem of attempting to simulate biological systems, with only the structural knowledge from experiments done in not-so-native conditions, always doubting the effect of initial model bias on my simulations. Cryo-ET offered an exciting prospect, promising quasi-native structures, *in situ*, at resolutions increasingly approaching those of single particle cryo-EM.

My thesis started in October 2020 in the MICA group at the Institute de Biologie Structurale (IBS) in Grenoble, under the supervision of Irina Gutsche and co-supervision of Joanna Timmins, leader of the GenOM team, with the ambitious project of developing cryo-ET visualization and analysis tools with the goal of understanding the 3D structural organization of the highly compact and yet dynamic chromatin of the radiation resistant bacterium *Deinococcus radiodurans*.

During the first year of my PhD, I realised that the chromatin model we planned to investigate was actually two-dimensional, due to its strong

adsorption to the air-water interface. Thus, I ended up using single particle cryo-EM instead of cryo-ET, whereby I confronted the problem of trying to pick and process very small proteins (the nucleoid associated protein HU) in single particle cryo-EM data collected by my supervisors, with nothing but DNA filaments as a guide, while learning the workflows and intricacies of cryo-EM and cryo-ET data processing. In the first part of this manuscript, I lay out the theoretical foundations of cryo-electron microscopy and single particle analysis ([Chapter 1: Cryo-EM and SPA](#)), as well as tomography and subtomogram averaging ([Chapter 2: Cryo-ET and STA](#)), contextualized within typical data collection and processing workflows.

After a year of working on this 2D model of *Deinococcus radiodurans* chromatin, my thesis committee and I concluded that this project required more work and careful redesign of the sample preparation strategy in order to be feasible in single particle, let alone in cryo-ET. The goal of my thesis thus shifted to new biological targets in *D. radiodurans*, while continuing my work on the development of software tools for cryo-ET.

One of such tools was blik, a cryo-ET-oriented plugin for napari, a rapidly growing scientific visualization tool designed for interactivity, ease of use, and customizability. We started working on blik — together with Alister Burt, another PhD student in MICA in his last year — out of the need to not only visualize cryo-ET data in its native 3D space, but also to be able to create custom tools to annotate, select, or otherwise manipulate the data in a way that acted less like a black-box and more like an exploratory experience. In particular, blik is aimed at the study of superstructural complexes — such as membrane lattices and filaments — whose investigation is often the reason why researchers turn to cryo-ET. With my growing contributions to napari, I was soon asked to join the core-developers of the project, whose development and maintenance I continued throughout my PhD, and which is now used by hundreds of researchers from several different fields. The work on blik resulted in a publication, which is included and contextualized within this thesis ([Chapter 3: blik: a cryo-ET visualisation and analysis tool](#)).

While the original thesis project about bacterial chromatin went to the

back burner, together with the GenOM group we continued to study *D. radiodurans*, fascinated by its incredible radiation resistance and its odd cellular structure which sets it apart from most bacteria. In my second year, I spent three months with my supervisor visiting Linda Sandblad's group at the Centre for Electron Microscopy in Umeå, where Irina collected the first set of tomograms of the bacterium from cryo-FIB-milled samples, revealing a host of new interesting features that we hadn't seen before. Among many, two captured our interest and became the main focus of my subsequent data analysis work: the distinctive arch-shaped FtsZ — a protein involved in bacterial septation that we were already working on using single particle analysis — and the multi-layered cell walls and septa — already under investigation by the GenOM team with fluorescence microscopy and other techniques. A publication about our work on the cell wall and septation mechanism of *D. radiodurans* is underway, and is attached to this manuscript in its current form (**Chapter 4: *D. radiodurans*: cell division and septation**).

Throughout the years of my PhD, I worked on several other projects worthy of inclusion in this manuscript. This includes my original PhD project on HU and bacterial chromatin, the ongoing work on *D. radiodurans* FtsZ combining the use of single particle cryo-EM on purified samples and of subtomogram averaging on the aforementioned tomograms, and a few computational tools I developed along the way (**Chapter 5: Bacterial chromatin, FtsZ, and other projects**).

In the final chapters of this thesis, I discuss the state of the cryo-ET software ecosystem in academia (**Chapter 6: Software in cryo-ET**), and the future of the projects in this thesis and of the cryo-ET field as a whole (**Chapter 7: Future perspectives**).

# Contents

<b>Abstract</b>	<b>IV</b>
<b>Acknowledgements</b>	<b>VI</b>
<b>Preface</b>	<b>IX</b>
<b>Contents</b>	<b>XII</b>
<b>I Introduction</b>	<b>1</b>
<b>1 Cryo-EM and SPA</b>	<b>2</b>
Contents .....	3
1.1 Cryo-EM: basic concepts .....	4
1.2 Sample preparation .....	5
Preferential orientation .....	5
1.3 Data collection .....	6
Image formation .....	7
Contrast Transfer Function .....	8
1.4 Preprocessing .....	13
Cross-correlation .....	13
Filtering and denoising .....	14
Dataset cleaning .....	15
1.5 Particle picking .....	15
1.6 2D classification .....	17
1.7 3D reconstruction .....	18

FSC and gold standard .....	20
Map post-processing .....	21
1.8 Refinement .....	21
1.9 Model building .....	22
<b>2 Cryo-ET and STA</b>	<b>23</b>
Contents .....	24
2.1 Cryo-ET: basic concepts .....	25
2.2 Sample preparation .....	25
FIB milling .....	26
Fiducials .....	26
2.3 Data collection .....	27
2.4 Preprocessing .....	29
Tilt series alignment .....	29
Tomogram Reconstruction .....	29
2.5 Annotation and segmentation .....	31
2.6 Particle picking .....	32
2.7 Subtomogram averaging .....	33
2.8 Pros and cons .....	34
<b>II Results</b>	<b>36</b>
<b>3 blik: a cryo-ET visualisation and analysis tool</b>	<b>37</b>
Contents .....	38
3.1 Abstract .....	39
3.2 Introduction .....	40
3.3 Results .....	43
Visualisation .....	44
Input/Output .....	47
Image segmentation .....	48
Filament and surface generation .....	50
Particle picking .....	53
Scipion Integration .....	54

3.4	Discussion .....	55
3.5	Conclusion .....	58
3.6	Materials and methods .....	59
	cryotypes and cryohub .....	59
	morphosamplers .....	60
	napari plugins .....	61
	napari and vispy .....	61
	blik .....	62
3.7	Acknowledgements .....	62
3.8	Data availability .....	62
3.9	Funding .....	62
3.10	Addendum .....	64
4	<b>D. radiodurans: cell division and septation</b>	65
	Contents .....	66
4.1	Abstract .....	67
4.2	Introduction .....	68
4.3	Results .....	71
	Cell wall composition and maturation .....	71
	Structure of septal tips .....	76
	Septation through a “sliding doors” mechanism .....	79
	PG synthesis machineries .....	83
	FtsZ is present at the tips of septa .....	86
4.4	Discussion .....	88
4.5	Materials and methods .....	94
	Bacterial cultures .....	94
	Cell labelling for confocal and SMLM microscopy .....	95
	Confocal data acquisition and processing .....	97
	SMLM (PAINT/dSTORM) data acquisition and processing .....	97
	Sample preparation for Cryo-ET .....	98
	Cryo-ET data acquisition .....	99
	Cryo-ET data processing .....	100
4.6	Acknowledgements .....	100

4.7	Funding .....	101	
4.8	Supplemental figures .....	102	
<b>5</b>	<b>Bacterial chromatin, FtsZ, and other projects</b>	<b>110</b>	
	Contents .....	110	
	5.1	Bacterial chromatin and HU .....	111
	5.2	FtsZ function and structure .....	116
		State of the art .....	116
		Structural study by SPA .....	118
		Tomography and STA .....	123
	5.3	Tools and scripts .....	128
		waretomo .....	128
		emscan .....	128
		Other napari tools .....	130
		cs2star .....	131
		stemia .....	131
	<b>III Discussion</b>	<b>133</b>	
<b>6</b>	<b>Software in cryo-ET</b>	<b>134</b>	
	Contents .....	134	
	6.1	Monolithic vs modular: an academia paradox .....	134
		Metadata wrangling .....	135
	6.2	Good software practices and human-in-the-loop .....	136
		Interactive visualization .....	137
<b>7</b>	<b>Future perspectives</b>	<b>139</b>	
	Contents .....	139	
	7.1	blik .....	140
		STA visualisation <i>in situ</i> .....	140
		3D interactivity .....	140
		Multicanvas .....	141
	7.2	napari .....	141

7.3 Teamtomo .....	142
7.4 <i>D. radiodurans</i> : FtsZ, HU, and more .....	143
Chromatin and HU .....	143
FtsZ SPA .....	143
FtsZ STA .....	144
Effects of stress and radiation .....	145
7.5 Cryo-ET .....	146
Hardware .....	146
Software .....	146
Applications .....	147
<b>List of Figures</b>	<b>149</b>
<b>Glossary</b>	<b>152</b>
<b>Bibliography</b>	<b>153</b>

# **Part I**

# **Introduction**

# Chapter 1

## Cryo-electron microscopy and single particle analysis

Knowing the structure of macromolecular complexes is often crucial to understand — and potentially take control of — the function and behavior of biological systems. To this end, structural biologists employ several techniques to unveil the structure of biomolecules and their complexes: typically proteins, nucleic acids and their ligands.

Arguably, the three giants in the field are X-ray crystallography, Nuclear Magnetic Resonance (NMR) and cryo-electron microscopy (cryo-EM), with several other techniques playing complementary, more specialized or niche roles (such as mass spectroscopy and small-angle neutron or X-ray scattering). In recent years, machine-learning (ML) structure prediction tools such as AlphaFold<sup>1,2</sup> and RoseTTAFold<sup>3</sup> have also conquered their way into the forefront of structural biology techniques, computationally predicting protein structures with unprecedented precision and without the wait and costs of experimental approaches. Each technique has pros and cons, making it suited to different samples and applications.

In X-ray crystallography — in many ways the predecessor to cryo-EM as the all-purpose structural biology technique — crystals are grown from the sample of interest; the crystals are then illuminated by an X-ray beam, and the diffraction pattern thus created can be detected and used to reconstruct

the three-dimensional (3D) structure of the sample. Thanks to the short wavelength of X-rays — as opposed to visible light — it is possible to localize the positions of atoms with sub-angstrom precision. X-ray crystallography has played a major role in the development of structural biology, and is still the primary source of protein structures on the Protein Data Bank<sup>4,5</sup>. However, the need for crystallization constitutes a major bottleneck: it requires very pure and homogeneous samples, and the procedure is often hard to devise and reproduce, requiring time, resources and some luck. Moreover, the protein is forced into a specific crystalline lattice, restricting the conformational freedom of the molecule and potentially limiting the biological significance of the obtained structures<sup>6</sup>.

## Contents

Contents .....	3
1.1 Cryo-EM: basic concepts .....	4
1.2 Sample preparation .....	5
Preferential orientation .....	5
1.3 Data collection .....	6
Image formation .....	7
Contrast Transfer Function .....	8
1.4 Preprocessing .....	13
Cross-correlation .....	13
Filtering and denoising .....	14
Dataset cleaning .....	15
1.5 Particle picking .....	15
1.6 2D classification .....	17
1.7 3D reconstruction .....	18
FSC and gold standard .....	20
Map post-processing .....	21
1.8 Refinement .....	21
1.9 Model building .....	22

## 1.1 Cryo-EM: basic concepts

Cryo-EM improves on these aspects by forgoing crystallization in favor of sample vitrification, which allows to capture the sample in a near-native state. This requires analysing many individual particles in different orientations, in a procedure known as single particle analysis (SPA).

In simple terms, the electron microscope works by shooting a coherent electron beam at the sample, and using a camera to detect the scattered electrons and form an image. Thanks to the small wavelength of electrons, cryo-EM can reach much higher resolution than light microscopy. In the last decade, the development of direct electron detectors made it possible to reach atomic resolutions, jump-starting to the so-called resolution revolution and the rise of cryo-EM as one of the primary methods for high resolution structure determination<sup>7</sup>.

Instead of relying on amplitude contrast for image formation, transmission electron microscopy uses phase contrast, which is caused by elastic scattering events affecting the electrons traversing the sample. Some electrons, however, are inelastically scattered; these electrons are no longer coherent, and therefore add to the noise of the image. Increasing the electron dose can help improve the signal-to-noise ratio (SNR), but comes at the cost of radiation damage, which denatures the sample and rapidly destroys high-resolution information. For these reasons, a significant limitation — and thus optimization target — of cryo-EM is the low SNR.

The cryo-EM workflow is well established, and usually consists of the same principal components: sample preparation and vitrification, data collection, preprocessing (cleaning, motion and CTF correction), particle picking and classification, three-dimensional (3D) reconstruction, and model building. This chapter describes such typical workflow ([Figure 1.1](#)), expanding on the theoretical bases underlying each step.

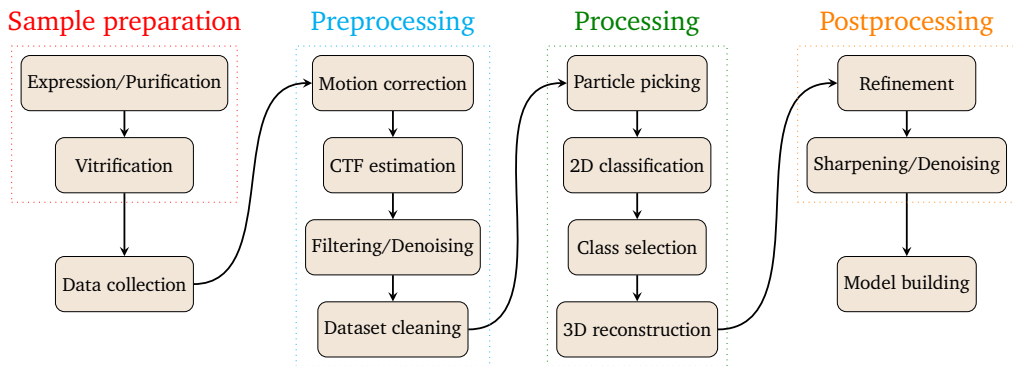


**FIGURE 1.1:** Cryo-EM workflow. Schematic of a typical cryo-EM workflow.

## 1.2 Sample preparation

Cryo-EM samples for SPA are usually prepared *in vitro* by expressing and purifying the protein or complex of interest to create a minimal system. Sample concentration and purity are important variables to control, as they will affect vitrification and data processing complexity. The sample solution is then deposited on a cryo-EM grid and vitrified via plunge freezing in liquid ethane or other methods (Figure 1.2)<sup>8</sup>. Vitrification allows to fix the sample in near-native, hydrated conditions while avoiding the formation of crystalline ice, which would damage the sample. When vitrifying, the thickness of the ice is crucial: a thinner layer will result in fewer inelastically scattered electrons during data collection and better SNR. However, too-thin ice can crack and increase issues with preferential orientation or particle distribution.

Novel approaches are beginning to use jets, sprays and microfluidics in order to obtain uniform, thin and more rapidly vitrified samples<sup>10</sup>.

### Preferential orientation

A common issue with sample preparation for cryo-EM is non-uniform orientation distribution of the protein in the vitrified sample, often due to particles being adsorbed to the air-water interface<sup>11</sup>.

Strong preferential orientation may completely preclude the ability to

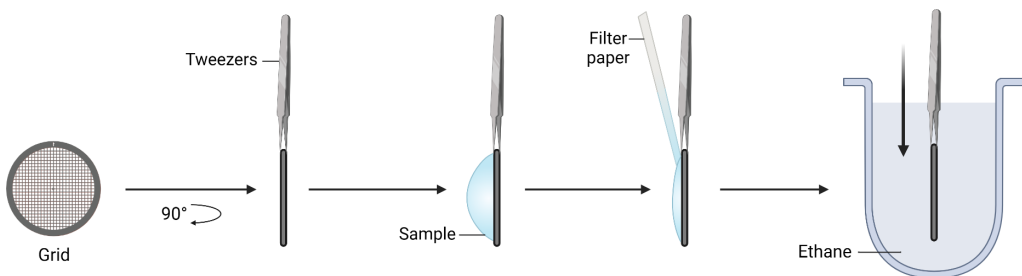


**FIGURE 1.2:** Vitrification via plunge freezing. Typical vitrification procedure via plunge freezing. A drop of sample is placed on the grid, blotted with a filter paper to reduce its thickness to a thin layer, and then plunged into liquid ethane. Figure adapted from Chung and Kim<sup>9</sup>.

do a 3D reconstruction, due to the lack of a wide distribution of orientations ([Section 1.7: 3D reconstruction](#)). When this problem arises, there are a few ways to tackle it during sample preparation. The most common is the addition of small amounts of detergents to occupy the air-water interface and prevent particles from preferentially orienting hydrophobic surfaces out of the water. Other methods are a bit more involved, such as the use of functionalized graphene grids<sup>12</sup>, streptavidin-coated affinity support grids<sup>13,14</sup>, but can offer more control over the orientation of the particles in the sample.

Alternatively, preferential orientation can be partially dealt with by collecting a tilted dataset, effectively forcing the target object into a different orientation. This method comes at the cost of worse SNR due to the thicker sample, increased motion due to doming, and worse CTF estimation. However, it was recently shown that the effect of these issues on the final resolution can be rendered negligible with careful preprocessing<sup>15</sup>.

### 1.3 Data collection

The vitrified sample is loaded into the electron microscope (under cryogenic conditions and vacuum, in order to maintain the sample vitrified and uncontaminated), and suitable positions on the grid are chosen for imaging, prioritizing for: presence of the target protein or complex, less

contamination, and lower ice thickness. In modern workflows and software, this step and the subsequent data collection are increasingly automated, allowing for higher throughput (up to a dozen-thousand images per day) and lower human intervention<sup>16</sup>.

During collection, the sample stage and/or electron beam are moved to each position to collect micrographs. At each position, a short movie is recorded, consisting of a few low-dose, short-exposure frames: this allows to reduce the blur caused by intra-frame motion (induced by external factors among which the electron beam itself); the frames will later be aligned and averaged to produce a single higher-contrast image. Direct detectors are therefore crucial not only for their raw improvement in achievable resolution, but also for their high speed, contributing to the reduction of yet another source of noise.

An important concept to be mindful of when setting up a data collection is defocus; in order to better understand how defocus affects later processing steps, we first need to understand image formation in the electron microscope, and the importance of estimating and correcting the Contrast Transfer Function (CTF).

## Image formation

In electron microscopy, image contrast derives almost entirely from phase contrast. The electron beam generated by the microscope is initially coherent, that is the phases of all the electrons in the beam are correlated. When electrons traverse the sample, they have a chance to undergo elastic scattering by the sample nuclei; this results in a shift in the electron's phase, leading to interference with the unscattered wave at the image plane (**Figure 1.3**). It's this interference that creates phase contrast, which the camera detects to generate the image. Because the fraction of scattered electrons is very low, the resulting beam has nearly the same amplitude as the non scattered beam, resulting in low contrast images.

Some electrons are also inelastically scattered by the electron clouds of the sample: these electrons lose energy — which is transferred to the

sample — and coherence, and are therefore adding to the noise of the image because the lenses no longer focus them to the right place. To mitigate the effect of loss of coherence, inelastically scattered electrons are filtered out using an energy filter, which removes electrons with energy that differs significantly from the unscattered ones (**Figure 1.3**). Unfortunately, the energy lost by inelastic scattering events is deposited on the sample, which denatures and deforms during imaging, further affecting the SNR; this process is what we call **radiation damage**.

Because of this, control over sample thickness is of crucial importance for image formation: higher thickness results in higher chance for collision, increasing the chance of inelastic scatterings. Additionally, a thicker sample may result in multiple elastic scattering events, which further alter the phase but cannot be distinguished from single scattering events, contributing to image noise.

## Contrast Transfer Function

The shift induced in the phase of the electron wave by elastic scattering events is closely related to the spatial frequency of features in the sample: smaller details which contain information at higher spatial frequency (such as the relative positioning of neighboring  $\alpha$ -helices), will scatter to higher angles; bigger features (such as biological membranes) will scatter to lower angles. Depending on the angle, the interference at the image plane will be constructive or destructive, resulting in certain spatial frequencies being damped or lost.

The CTF is a function that describes exactly this: how signal is transmitted through the sample and onto the image, as a function of spatial frequency. Where the CTF reaches a value of 0, no signal is transferred; a value of 1, on the other hand, is a perfect signal transfer.

The CTF has a close relationship with the Fourier transform (FT) of a micrograph: the 1D rotational average of the power spectrum (PS) of the image (the square of the amplitude of the FT of the image) forms the curve used to estimate the CTF (**Figure 1.4**). The image of a point source —

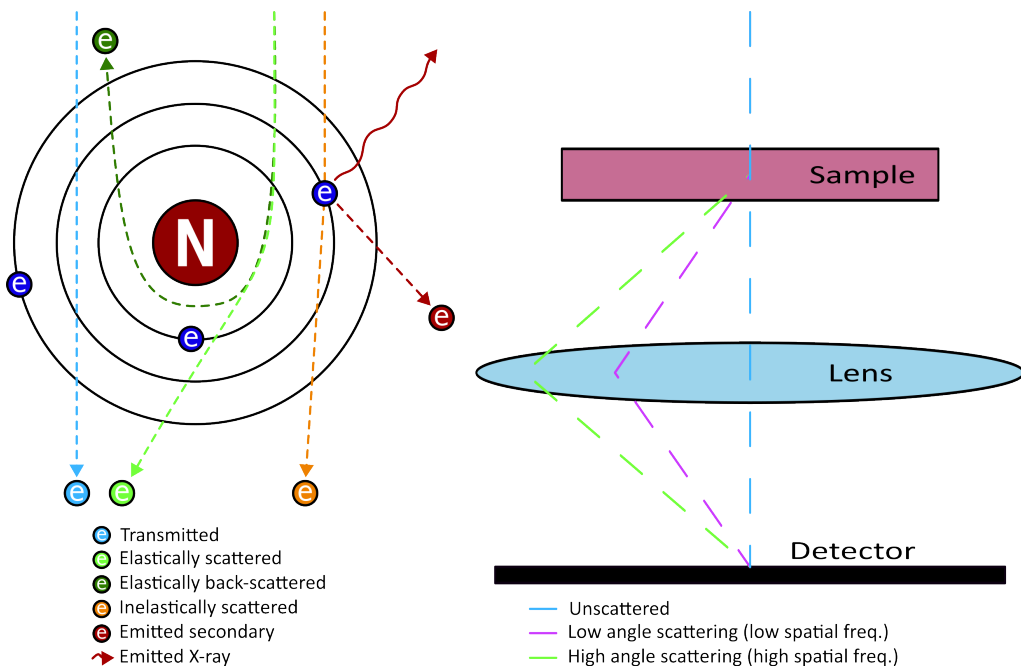


**FIGURE 1.3: Image formation.** Electron scattering and diffraction are the physical processes at the core of cryo-EM image formation. Electrons can scatter in several different ways (left), but only elastic scattering contributes to image formation via phase contrast with the transmitted electrons. Features contained in the sample that present different spatial frequencies result in scattering at different angles (right); depending on the difference in path travelled and the wavelength of the electron beam, this results in interference between differently scattered waves. In this figure where wave oscillations are visualized as dashed lines, we can see that the unscattered and low-angle scattered waves result in constructive interference, while the high-angle scattered waves interfere destructively.

which has no sample, no atoms, and therefore no Fourier components — would produce a 1D PS identical to its theoretical CTF.

The CTF is usually described as composed of two main elements. The first one is a sinusoidal component caused by the periodicity of destructive and constructive interference of electron phases at different spatial frequencies. It is visible in the PS of cryo-EM images as a set of concentric rings called Thon rings ([Figure 1.4A](#)). The exact shape of the Thon rings depends on several factors, first among which the defocus: changing defocus affects the oscillation frequency, thus shifting the zeros of the CTF and boosting or nullifying different spatial frequencies ([Figure 1.4B](#)).

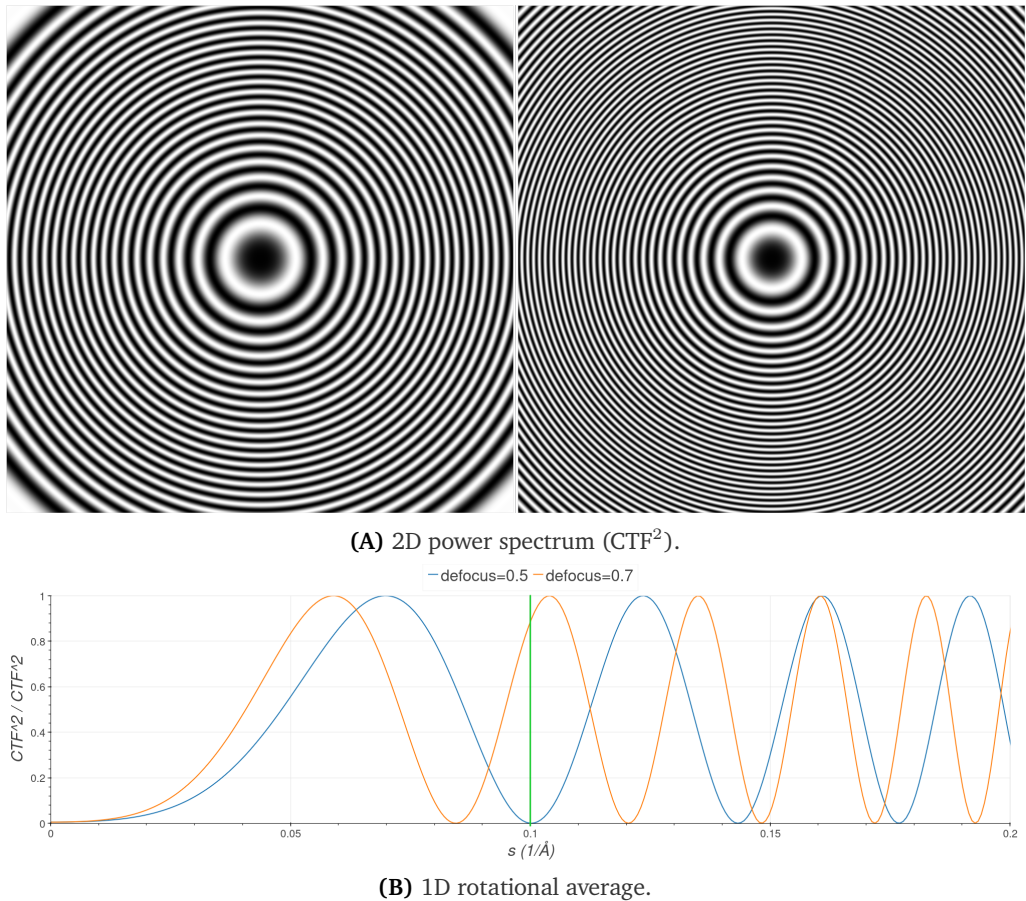


**FIGURE 1.4: CTF: effect of defocus.** Simulated CTF of two images at different defoci. (a) 2D power spectrum ( $CTF^2$ ). (b) 1D rotational average, highlighting in green the spatial frequency of  $0.1 \text{ \AA}^{-1}$ , where the blue line (CTF at defocus  $0.5 \mu\text{m}$ ) is close to 0, whereas the orange line (CTF at defocus  $0.7 \mu\text{m}$ ) is close to 1. Images generated with: <https://ctfsimulation.streamlit.app/><sup>17</sup>.

To ensure all spatial frequencies are sampled, a data collection must include many images collected at a range of different defoci.

Of note is that since the CTF value starts at 0, low spatial frequencies are always damped; in practical terms, this results in images where low resolution features (such as membranes and big objects) are harder to see, making it harder to distinguish objects from the noise, pick particles (Section 1.5: Particle picking) and do further processing. For this reason, a certain amount of defocus is always used, which “compresses” the CTF thus improving the low frequency contrast transfer; this comes unfortu-

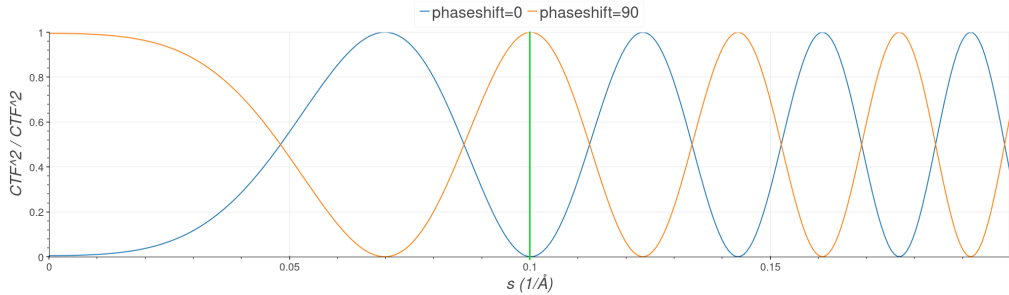


**FIGURE 1.5:** CTF: effect of phase shift. 1D rotational average of a simulated CTF of two images at different phase shifts. Note how the phase-shifted CTF (orange) has a peak at spatial frequency 0, boosting low-resolution features. Image generated with: <https://ctfsimulation.streamlit.app/><sup>17</sup>.

nately at the cost of jumbling up the high frequency information with more CTF oscillations, making it harder to correctly estimate the CTF at high resolutions (**Figure 1.4B**).

Alternatively, a phase plate can be used to shift the phase of the electrons by 90° and acquire images on focus (**Figure 1.5**). While phase plates are in theory an ideal solution to this problem, there are still some engineering and physical limitations that limit their use; several groups are currently working to overcome such hurdles<sup>18,19</sup>.

The second component of the CTF is broadly called “envelope function”, a dampening effect which attenuates the signal at higher resolutions. It depends on many factors, such as lens aberrations, limitations of the electron gun, frame alignment imprecision, etc. This effect is visible in the PS as an attenuation of the signal at higher resolutions (**Figure 1.6**). Since the PS (what we actually measure) is equivalent to the CTF<sup>2</sup>, the dampening is exacerbated because values closer to 0 become even smaller and harder to detect. Importantly, this effect is worse at higher defocus, contributing the worse high-resolution information transfer of higher defocus images.

This signal decay, combined with the low SNR of the images, poses a resolution limit beyond which it is impossible to estimate (and therefore correct) the effect of the CTF on the image.

In all the examples above, we assumed the CTF to be rotationally invariant. However, a small amount of astigmatism — which causes the PS to be

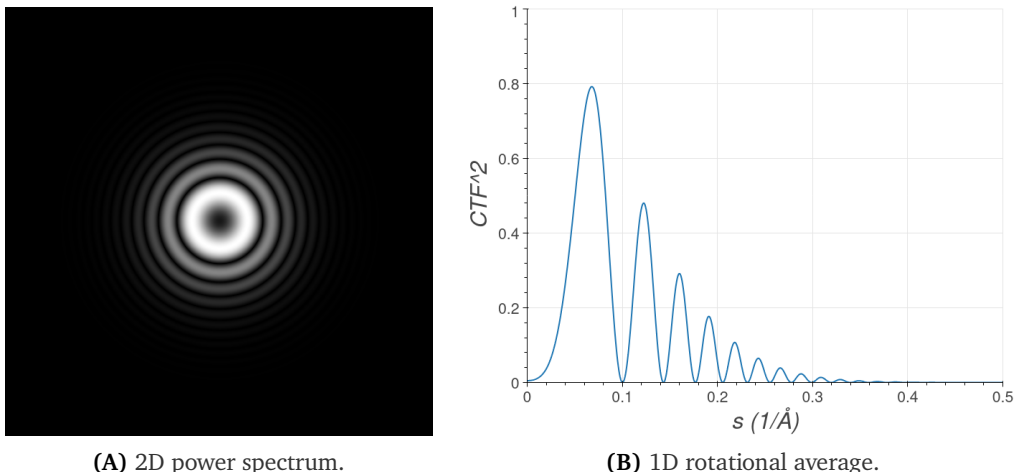


**FIGURE 1.6: CTF: effect of the envelope function.** 2D power spectrum (left) and 1D rotational average (right) of a simulated CTF, including some envelope function effects (such as beam convergence and energy spread). As a result, higher resolution frequencies are damped, reducing the signal available for CTF estimation and high resolution reconstruction. Images generated with: <https://ctfsimulation.streamlit.app/><sup>17</sup>.

stretched in one direction, resulting in elliptical Thon rings — is typically present in all cryo-EM images, due to the imprecisions of microscope lens adjustement. For this reason, astigmatism must be estimated and corrected, before a 1D rotational average can be computed for CTF estimation, and later accounted for during correction.

So far we discussed what happens to the Fourier transform or PS of an image, that is in **Fourier space**; in practice, the CTF has visible effects also in **real space**. The signal becomes delocalized, blurring the image; as explained by the convolution theorem<sup>20</sup>, this delocalization is the result of the convolution of the Fourier transform of the CTF (known as Point Spread Function or PSF) with the image. Delocalization of signal directly affects how image processing is performed; for example, particle picking should account for it by extracting bigger image patches to ensure delocalized signal can be deconvolved when CTF correcting ([Section 1.5: Particle picking](#)).

## 1.4 Preprocessing

Before particle picking, classification, and 3D reconstruction can be performed, the collected data must undergo a few preprocessing steps.

First, each movie generated during data collection must be aligned and averaged. In state of the art applications, this alignment is typically done not only on a full frame level, but also in a localized fashion, by aligning image patches or by describing the system with a smooth deformation field<sup>21-23</sup>.

In state of the art software, similarly to how motion correction is treated, defocus (and thus CTF) is estimated at a local level, accounting for variability in the positioning of the sample with respect to the detector. The parameters thus obtained are later used to correct for the CTF during classification and reconstruction ([Section 1.6: 2D classification](#) and [Section 1.7: 3D reconstruction](#)). Modern workflows also offer the ability to later refine the deformation parameters as part of the refinement process ([Section 1.8: Refinement](#)).

Both motion correction and CTF estimation — as well as many other steps and techniques in image processing — rely on the ability to quantify the similarity of two signals; this is typically done by calculating the cross-correlation (CC) of the images or signals.

### Cross-correlation

The CC of two signals (such as two images) is a measure of how similar the two signals are at all possible relative shifts. The CC function of two signals will be higher for signals that present more similar features, and have a peak at the relative shift where the signals present strongest similarity ([Figure 1.7](#)). This is a useful feature for most applications, because we often care about where exactly the similarity is high (e.g. for motion correction, particle picking and alignment ([Section 1.5: Particle picking](#))).

In the case of 2D data, calculating the cross-correlation of two images often also includes the additional step of a rotational search, to account for

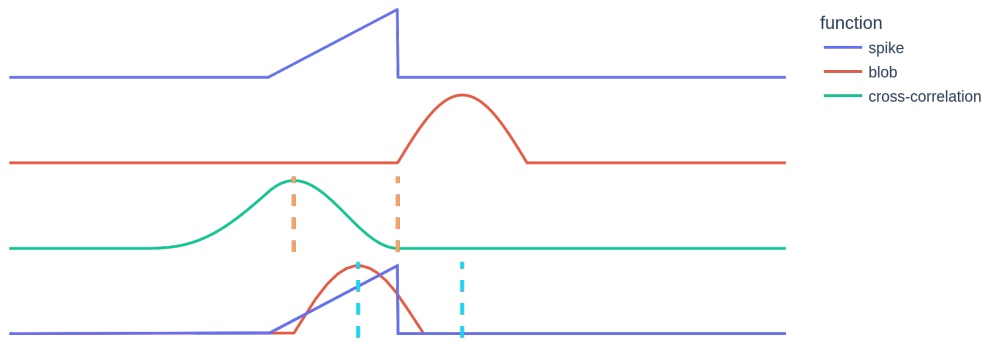


**FIGURE 1.7: Cross-correlation of 1D signals.** Cross-correlation of two 1D signals, spike and blob. The position of the peak of the resulting cross-correlation indicates relative shift at which blob presents maximal similarity with spike. Shifting blob by the same amount shows the best overlap between the two signals.

the different in-plane rotation of particles that would otherwise be missed by simple CC.

## Filtering and denoising

Due to the low SNR of cryo-EM data, even motion-corrected micrographs can be surprisingly hard to interpret. To enhance the contrast of biological features and better judge the quality of the data — as well as improve the ability to distinguish particles from the background and from one another for the purposes of picking ([Section 1.5: Particle picking](#)) — micrographs often undergo a round of filtering and/or denoising.

The simplest — and most commonly used — type of filtering is Fourier masking; by reducing or zeroing the values inside a disc or annulus in Fourier space, the respective spatial frequencies are damped in the image. In practice, this is often used to remove high-frequency components (low-pass filter), but there are also sometimes benefits to the removal of other ranges of spatial frequencies ([Figure 1.8](#)).

In the last few years, denoising using ML tools has become standard practice, with algorithms such as noise2noise and noise2void<sup>24,25</sup> being implemented in several cryo-EM software suites<sup>23,26,27</sup>.

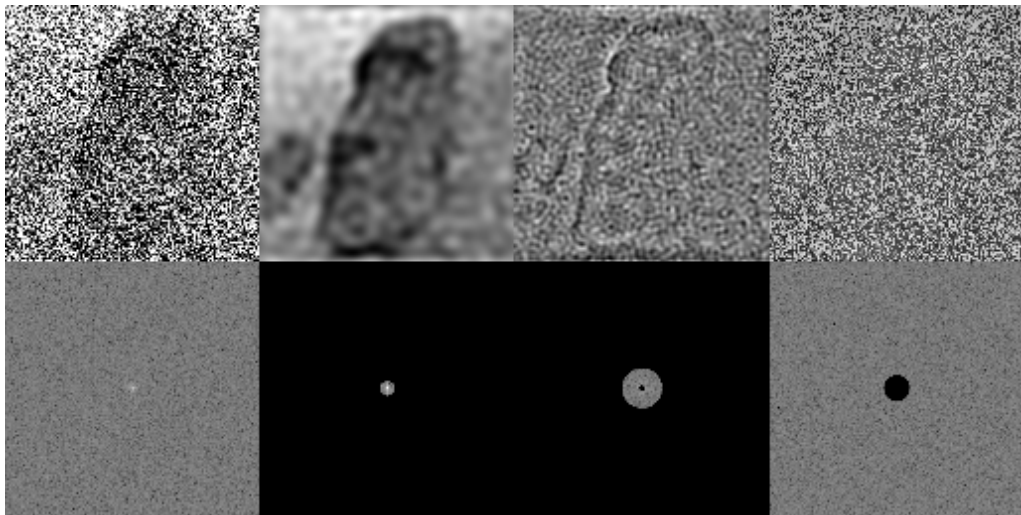


**FIGURE 1.8: Fourier filtering.** Examples of how filtering a noisy image (top left image) with different kinds of Fourier masks (bottom row) produces different results (top row). From left to right: no filtering, low-pass, band-pass, high-pass. Low-pass filtering can restore interpretability of highly noisy images. As highlighted by the difference between the low-passed (second column) and high-passed (last column) images, a very small range of low spatial frequencies is actually responsible for the majority of our perception of the general shape of an object. Noise, on the other hand, more strongly affects high resolution information.

## Dataset cleaning

The dataset often contains bad images for various reasons: bad CTF estimation, too high motion, issues with autofocus, too thick or cracked ice, etc. During preprocessing, these micrographs are usually discarded, either manually or by using batch automated tools which estimate the data quality.

Once the data is clean, motion corrected and CTF-estimated, the particles of interest can be picked for further processing.

## 1.5 Particle picking

In order to reconstruct the 3D map of particles of interest, one first needs to locate them on the micrograph. This procedure is called particle picking, and can be performed with varying levels of automation, and using several

different techniques. The most commonly used are variations of: manual picking, template matching, and ML tools.

Manual picking is generally more intuitive and can be very precise, but is also tedious and time-consuming. Data may also be too noisy for humans to distinguish particles from one another and from the background, leading to missed particles or wrong picks. To aid with manual picking, preprocessed micrographs are often filtered and denoised to improve the contrast ([Section 1.4: Filtering and denoising](#)).

To improve the picking speed and precision, template matching is often used to automate searching for a recognizable object. This picking method requires a template, a small image of a 2D projection of the object of interest. This can be obtained in a few ways: synthetically (by using a generated shape), by projecting a known map or model from previous work, or by using the results of a first round of 2D classification ([Section 1.6: 2D classification](#)) from a preliminary manual picking. While the exact details of the algorithm may vary, at its core template matching relies on calculating the CC ([Section 1.4: Cross-correlation](#)) function between the template and the micrographs in order to locate putative particles positions in the whole dataset.

More recently, template matching is often being replaced with machine learning, which serves a similar purpose but can have a more nuanced understanding of surrounding context which helps reduce the false negatives and positives that are intrinsically present with template matching of noisy data.

There are also “structured” variants of all these picking methods, where some existing geometric and structural knowledge about the system is used to inform the picking in some way. For example, filament picking is quite commonly used due to how widespread helical assemblies are in biology; it can be done manually<sup>28,29</sup>, with template-based methods<sup>22</sup>, and using ML<sup>30,31</sup>.

Regardless of the picking method, it is important to ensure that the target object is represented with projections from many different orientations; this will be crucial to properly reconstruct a 3D map of the object ([Section 1.7](#):

3D reconstruction).

## 1.6 2D classification

Even with the best data and most advanced methods, picked particles typically contain a variety of several different objects, conformations, and spurious background or contamination picks; before moving on to reconstruction, the wheat should be separated from the chaff. To do so, particles are split into groups based on similarity, in a process called 2D classification.

Once again, some form of cross-correlation ([Section 1.4: Cross-correlation](#)) is involved in the process, since the goal is to cluster together similar particles and separate different ones. The algorithm is typically iterative: after generating an initial set of classes by averaging random particles, particle poses are progressively refined to find the best CC score. Based on this score, each particle is assigned to a class (or a score for each class, in probabilistic models<sup>28</sup>), and for each class a class average is computed, combining the signal from all the particles belonging to that class. The more poses are refined, the more the signal that's shared by similar particles is boosted, improving the SNR of the class average. Class averages are used to calculate the CC at each iteration, and used at the end of the process to inspect the dataset and select only the useful particles.

With this information, particle classes can be split into groups for further processing or discarded. This is typically done manually by inspecting class averages and assigning each class to a group, depending on the goals of the project and the following processing steps. For a uniform purified dataset, classification might only serve the purpose of discarding spurious picks. For trickier samples (protein complexes, high conformational variability, non-uniform orientation distribution, cell-extract cryo-EM<sup>32,33</sup>), multiple groupings and several rounds of classification may be necessary to isolate each relevant state.

Once reasonably sure that each group contains only particles representing projections of different orientations of copies of the same object the 3D map of this object can be reconstructed — though conformational

variability might still be present and will need to be dealt with at a later stage.

## 1.7 3D reconstruction

3D reconstruction is the process by which a volumetric map of an object can be reconstructed from 2D projections. This is possible thanks to the central slice theorem<sup>34</sup>, which provides a bidirectional mathematical relationship between a volume and its projections.

The theorem states that the Fourier transform of the 2D projection of a volume at a certain orientation, is equal to the central slice through the Fourier transform of the volume at the orientation perpendicular to the projection ([Figure 1.9](#)).

It's worth noting that the algorithms used by reconstruction software, while based on this principle, are often in practice not based on Fourier-domain reconstruction, but use different methods such as weighted back-projection or iterative approaches like Simultaneous Algebraic Reconstruction Technique (SART) and Simultaneous Iterative Reconstruction Technique (SIRT)<sup>35-37</sup>.

In the case of SPA, the central slice theorem allows us to combine the projection of many different particles, under the assumption that they come from near-identical copies of the same object.

It is crucial in this process that as many different orientations as possible are represented in the dataset. This is because, in order to have an isotropically well-resolved reconstruction, we need to fill the 3D Fourier space as much as possible (or, as needed according to the Crowther criterion<sup>39</sup>) with differently oriented central slices.

Similarly to 2D classification, 3D reconstruction is an iterative process where each particle is correlated to templates to find the best match. This time, however, the templates are obtained by projecting a 3D model at different orientations, in a process called projection matching ([Figure 1.10](#)). Instead of assigning classes, projection matching refines the relative (3D) orientations of each particle relative to the original 3D object. The 3D

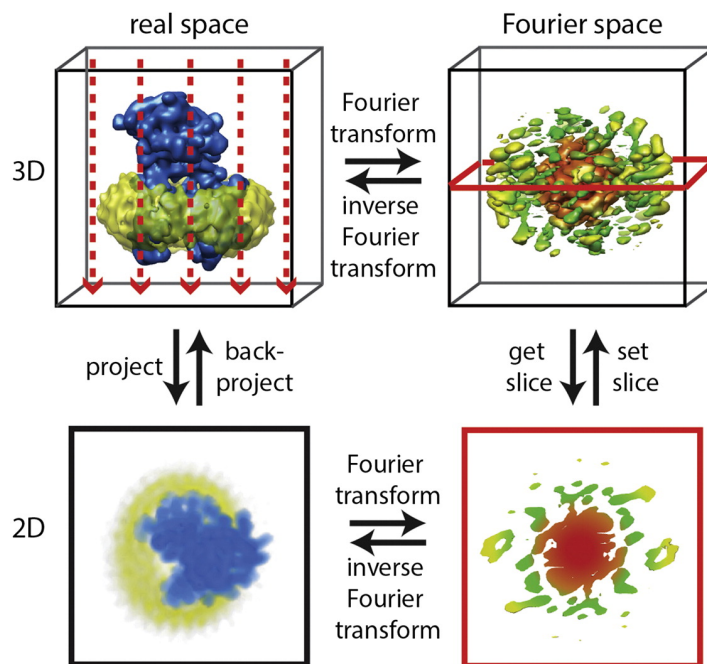


**FIGURE 1.9: Central slice theorem.** Showcase of how the central slice theorem is used for 3D reconstruction in cryo-EM. A 2D projection of a 3D volume in real space at a certain orientation is equivalent to the 2D slice perpendicular to that orientation in Fourier space. Figure adapted from Nogales and Scheres<sup>38</sup>.

model is initially either derived from previous work, or generated *ab initio* from the particles themselves. During each iteration, particles' FTs are used to fill a 3D FT according to central slice theorem, which allows to generate a new 3D model. The assigned orientations are progressively refined in order to improve the model resolution. Once there is no longer significant improvement ([Section 1.7: FSC and gold standard](#)), the process stops, and the final 3D map is generated.

In some cases, it might be useful to go one step further and do 3D classification; this is essentially the same procedure, but using multiple 3D models at the same time to not only assign orientations, but also split particles into different classes. This may be useful — especially combined with some kind of mask to isolate areas of interest — in cases where 2D classification was unable to separate out very similar objects.

When classification is too categorical to capture nuanced systems (such as continuous conformational ensembles), other kinds of procedures able to

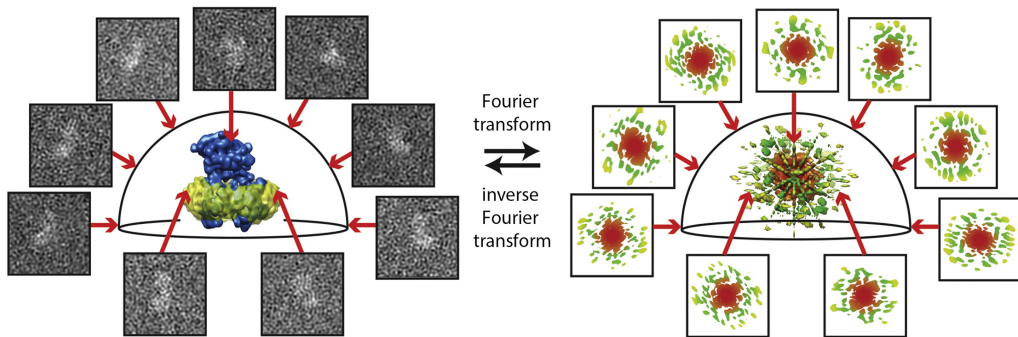


**FIGURE 1.10: Projection matching.** Projection matching in cryo-EM. Particle picks are assigned progressively better orientations that most closely match synthetic 2D projections generated from the current 3D model. By inserting the FT of each particle at the assigned orientation into the 3D Fourier space, and then doing the inverse Fourier transform to go back to real space, a new updated model is generated. Figure adapted from Nogales and Scheres<sup>38</sup>.

capture more variability may be used, such as principal component analysis (PCA)<sup>40,41</sup>, multibody refinement<sup>42</sup>, 3D flexible refinement<sup>43</sup>, etc.

## FSC and gold standard

For most procedures that attempt to refine parameters in order to improve a 3D classification or reconstruction, a method is needed to estimate the quality (resolution) of the current model.

The established approach is called **gold standard** and relies on calculating the Fourier shell correlation (FSC) of two independent halves of the data. At the cost of halving the amount of data we can use at once to make a map, we gain the ability to estimate how trustworthy our reconstruction is.

At the beginning of the process, the dataset (which in the case of 3D reconstruction is the ensemble of picked particles) is randomly split in two halves. At each iteration of the refinement, each half is used to generate an independent 3D reconstruction. The Fourier transforms of the two maps are then cross-correlated as a function of spatial frequency, giving a plot such as the one in Figure 1.11. A high correlation between Fourier shell at the same spatial frequency indicates a high degree of reproducibility of

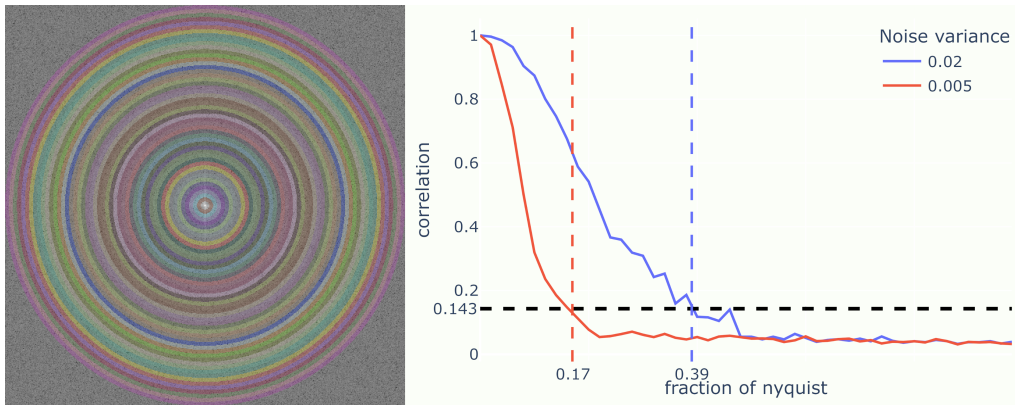


**FIGURE 1.11: Fourier shell correlation.** Showcase of a 2D version of Fourier shell correlation. Gaussian noise was applied to two identical images, which were then compared by gradually cross-correlating concentric shells (left). The resulting plot (right) is a measure of the similarity as a function of spatial frequency. As spatial frequency increases, noise becomes dominant, degrading correlation and thus the trustworthiness of the data. The threshold of 0.143 is used to determine the final resolution, which is higher for the less noisy image.

those frequency components: that is, up to that resolution, the map can be trusted. The threshold typically used to formally determine the “resolution of the map” is 0.143, for both mathematical and historical reasons related to the interpretability of X-ray crystallography maps<sup>44</sup>.

## Map post-processing

Reconstructed maps are normally post-processed to improve interpretability and usability in model building procedures.

Different types of masking, filtering, and denoising can be applied, depending on the downstream steps.

## 1.8 Refinement

Once a 3D model is obtained, several state of the art software pipelines offer the ability to refine previously-defined parameters. The parameters that can be refined range from particle positions and orientations, to CTF estimation and motion correction, to more complex artifact-inducing factors such as

lens aberrations and Ewald sphere curvature<sup>22,28,45</sup>. While resolution of the resulting 3D reconstruction is the most obvious parameter used to validate the improvements, there are several other criteria that may be considered, such as local resolution, angular distribution of views, map continuity, etc.

The implementation details of refinement procedures are often quite different between software, but are generally based on an iterative process where parameters are adjusted on a per-particle basis, and a new 3D reconstruction is generated and validated via FSC to estimate the effects of the correction applied.

These procedures can have dramatic effects on the final resolution of a map, especially when pushing for sub-nanometer resolution where small aberrations and artifacts can have significant effects on the achievable resolution.

## 1.9 Model building

If a map reaches high enough resolution, it is possible to build an atomic model based on the volume density. This process is called model building, and is typically done with a mix of manual and automated tools.

Models are built by placing amino acids (or other structural components) so that their theoretical electron scattering matches the density map obtained from 3D reconstruction. Some recent tools manage to fully automate this process for maps of high enough resolution ( $\lesssim 4 \text{ \AA}$ ), even without knowing the protein's sequence<sup>46</sup>.

# Chapter 2

## Cryo-electron tomography and subtomogram averaging

Compared to X-ray crystallography, SPA sample preparation is a strong selling point: it can be much faster and simpler, not requiring crystallization and needing small quantities of sample, and being less sensitive to contamination. Thanks to the fast vitrification, SPA is also better for studying the sample at near-native state, and for capturing rare or dynamic states (though the analysis in these cases becomes trickier). However, due to the unknown particle orientations and low SNR, SPA data analysis is trickier and more error-prone, especially for small particles ( $\lesssim 100$  kDa), where X-ray crystallography is usually the better choice.

On the other hand, bigger particles or complexes are usually better handled by cryo-EM: with larger molecular size, crystallization gets increasingly difficult, and NMR can no longer be effectively used for structural determination. Conversely, NMR allows to gather some information on the dynamics of the sample, even large ones and even directly in solution, since there's no need for crystallization or vitrification. This, however, requires appropriate isotope or methyl labeling and very high concentrations, which may cause aggregation or non-native conformations.

All these techniques rely on drawing information about an ensemble of molecules, typically with an *in vitro* purified sample. However, macro-

molecular systems can often be fully understood only by accounting for their biological context, which is partly or fully lost in the expression and purification process. When studying biological systems that form larger, heterogenous mesoscale complexes — spanning hundreds of nanometers, often called superstructures — having a three-dimensional understanding of individual events within their cellular context becomes paramount.

While ML tools such as AlphaFold3<sup>2</sup> have recently become powerful enough to accurately predict even large protein complexes, they still suffer from the same decontextualization problem as all these experimental techniques.

A method that promises to solve these problems is cryo-electron tomography (cryo-ET): a technique that can look not only at purified macromolecules, but at entire cells and tissues, *in situ* in near-native conditions, with the ability to reach higher resolutions via subtomogram averaging, while retaining contextual information and providing a 3D view into single events.

## Contents

Contents .....	24
2.1 Cryo-ET: basic concepts .....	25
2.2 Sample preparation .....	25
FIB milling .....	26
Fiducials .....	26
2.3 Data collection .....	27
2.4 Preprocessing .....	29
Tilt series alignment .....	29
Tomogram Reconstruction .....	29
2.5 Annotation and segmentation .....	31
2.6 Particle picking .....	32
2.7 Subtomogram averaging .....	33
2.8 Pros and cons .....	34

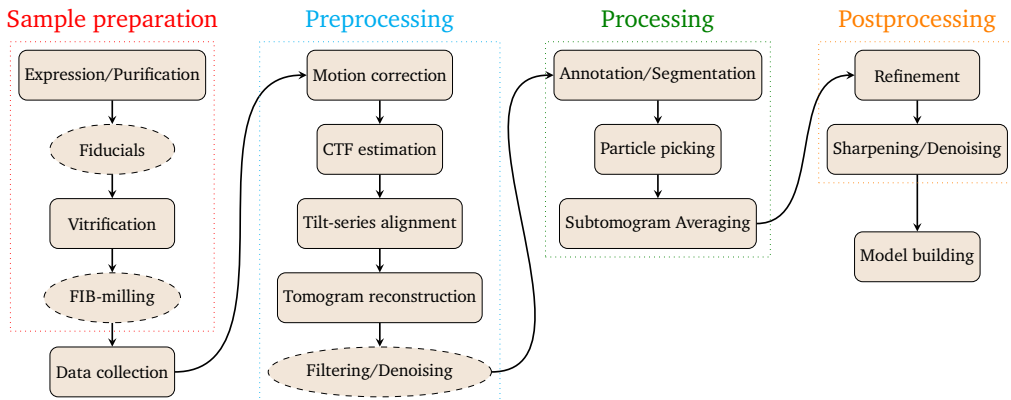


**FIGURE 2.1:** Cryo-ET workflow. Schematic of a typical cryo-ET workflow. Dashed ellipses are situational/optional steps.

## 2.1 Cryo-ET: basic concepts

Tomographic reconstruction is not a recent invention: the first appearance goes back more than a century<sup>47</sup>; its successful application to cryo-EM, however, is only a recent development closely linked to the resolution revolution, which allowed to finally overcome the biggest overarching limitation of cryo-ET — poor signal-to-noise ratio — enough to reach subnanometer resolutions<sup>48,49</sup>.

At its core, cryo-ET is just cryo-EM with extra steps; they share much of the theory, hardware and software. The key difference is that, where single particle cryo-EM uses projections from different *copies* of the same object to reconstruct a 3D map, cryo-ET images the same location from multiple orientations in order to reconstruct a 3D map from multiple projections of the *same* object. This chapter describes the theory of cryo-ET, how it deviates from SPA in its workflow (**Figure 2.1**), and the current state of the art with its limitations and upcoming developments.

## 2.2 Sample preparation

As with SPA, vitrification remains the key step of sample preparation for cryo-ET. Due to the intrinsically worse SNR — caused by the lower electron dose

used during data collection, necessary to preserve the sample (**Section 2.3: Data collection**) — cryo-ET sample preparation requires extra care to reduce any possible source of additional noise.

One such source is the thickness of the sample; while this problem can be avoided by preparing thinner model systems *in vitro*, it's otherwise unavoidable for samples such as entire cells or organelles, where the *in situ* benefits of cryo-ET really shine. A thick sample poses also another problem: with thickness higher than a few  $\mu\text{m}$  (most mammalian cells), plunge freezing does not have a fast enough cooling rate to prevent the formation of crystalline ice. For these reasons, a combination of two techniques is often used: high-pressure freezing (HPF) and cryo-ultramicrotomy. In HPF, the sample is put under great pressure ( $>200$  MPa) before ultrarapid freezing, preventing expansion and thus lowering the cooling rate needed for vitrification, without the need for potentially cell-disrupting cryoprotectant<sup>50,51</sup>. Then, cryo-ultramicrotomy uses a diamond knife to cut from the sample very thin slices, that are then deposited on a grid for imaging<sup>52</sup>. In recent years, focused ion beam (FIB) milling — a technique already well established in material sciences — has found widespread use in cryo-ET sample preparation, allowing to slice thin lamellae from a vitrified sample without incurring in the shear and surface deformations of cryo-ultramicrotomy<sup>53</sup>.

## FIB milling

FIB milling typically makes use of a gallium ion beam — or, more recently, xenon or oxygen plasma — to ablate thick samples, which can be thus thinned to below 150 nm. Preparing lamellae via FIB milling is becoming standard procedure in cryo-ET, and many cryo-ET facilities are automating much of the process, increasing reliability, speed and reproducibility.

## Fiducials

During data collection, despite vitrification, samples undergo different kinds of deformations. Moreover, due to the intrinsic imprecision of controlling the hardware of the microscope, there will always be some shift and angle

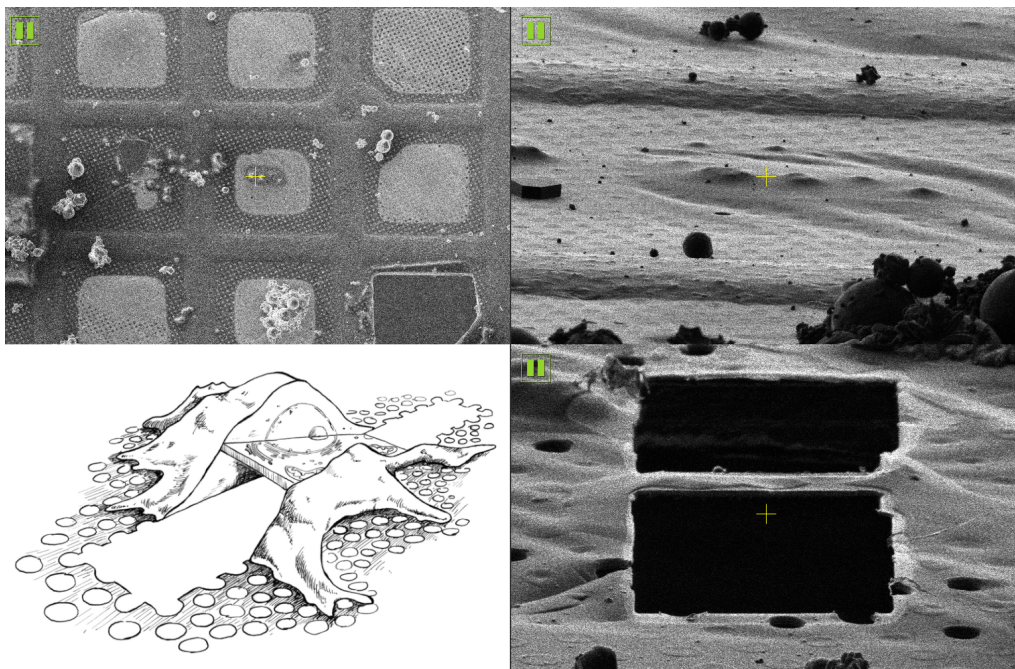


**FIGURE 2.2: FIB milling.** Microscope snapshots from FIB milling procedure on *Deinococcus radiodurans*. A cluster of cells, visible as a bump on the SEM, is selected from the grid (top left). From a shallow angle of around  $15^\circ$  from the grid (top right) the FIB is used to ablate material above and below the area of interest. This leaves a thin lamellae suitable for cryo-ET (bottom). Milled cell drawing (bottom left) taken from Villa et al.<sup>54</sup>.

mismatch between different tilts during a tilt series collection ([Section 2.3: Data collection](#)).

To help with correcting these errors, it is often useful to add to the sample some fiducials: small high-contrast, round objects (typically 10 nm gold beads) that can be easily located in the images and later used to estimate sample shift, rotation, and deformations ([Section 2.4: Tilt series alignment](#)).

## 2.3 Data collection

In order to acquire a sequence of images at different tilts (termed **tilt series**) for tomographic reconstruction, the same area of the sample needs to be imaged multiple times, at a range of different angles. During collection,

the sample is rotated around a tilt axis perpendicular to the electron beam, in small angular increments so as to expose a different view to the electron beam. It's important to position the sample at **eucentric height** — the height at which a rotation of the sample results neither in a change in focus nor a lateral movement — so that the area of interest remains at the same focus and at the center of the field of view.

Due to the multiple exposures, in order to preserve the specimen from radiation damage the electron dose must be fractionated to much lower than typical in SPA, but still high enough to capture enough signal to allow motion correction<sup>55</sup>.

Each subsequent exposure further damages the sample, which degrades the high resolution information first. This, in combination with the fact that in cryo-ET the electron beam has to traverse a thicker sample at high tilts — leading to worse SNR — created the need for optimized collection schemes. The most commonly used nowadays is the Hagen (or dose-symmetric) scheme<sup>56</sup>: it collects the first image at 0° tilt, and then alternates between negative and positive tilts until it reaches the maximum tilt. This minimizes the radiation damage when SNR is best, allowing to capture high resolution information at its prime, before it is degraded by cumulative exposures.

Due to the geometry of the sample and its support within the microscope, there is a limit to how high an angle can be reached when tilting the sample. This angle is typically around 60-70°, beyond which the sample becomes too thick for imaging at such low doses, and the grid bars come into view obscuring part of the sample. This will result in a **missing wedge** of information in Fourier space during tomographic reconstruction ([Section 2.4: Tomogram Reconstruction](#)).

Conventional wisdom sets the interval between subsequent tilts at around 3° to ensure enough Fourier space filling while limiting radiation damage, though depending on the application — especially where certain spatial frequencies are considered important or over-represented in the sample — it might be worth considering smaller, wider, or non-linear increments<sup>57</sup>.

## 2.4 Preprocessing

Cryo-ET data undergoes similar preprocessing steps as SPA data ([Section 1.4: Preprocessing](#)), albeit with less precision due to the low electron dose.

While at this point single particle data is ready for particle picking and other downstream work, cryo-ET data must still undergo tomographic reconstruction in order to obtain the 3D volumetric reconstruction of the sample.

To do so, tilt series alignment parameters must first be estimated in order to correct for equipment imprecision and sample deformations, and then used for 3D volume reconstruction.

### Tilt series alignment

The most basic alignment procedures require at least full-frame alignment; similar to motion correction, tilt images are rotated and shifted in order to maximize their CC score. Where fiducials are present ([Section 2.2: Fiducials](#)), these can be treated as static points within the sample and used instead as anchors to mathematically estimate the geometric transformation between different tilts<sup>[58–60](#)</sup>.

In state of the art software, alignment procedures (with or without fiducials) can also account for spatio-temporal deformations of the sample, either already during tilt series alignment<sup>[61](#)</sup>, or later during refinement<sup>[45,62–64](#)</sup>.

### Tomogram Reconstruction

Similarly to how 3D reconstructions are obtained from 2D particles in SPA based on the central slice theorem ([Section 1.7: 3D reconstruction](#)), the aligned tilt series can be used to reconstruct the full tomogram. Depending on the software suite and workflow, full tomogram reconstructions may be used only for template matching ([Section 2.6: Particle picking](#)) and

segmentation purposes, or also to extract subtomograms at small pixel sizes for subtomogram averaging (**Section 2.7: Subtomogram averaging**).

Differently from SPA, cryo-ET has the advantage of knowing the 3D positioning of each point in the tomogram. This allows to bring defocus estimation and CTF correction to the next level: not only is CTF locally estimated depending on the in-plane position of features, but also accounting for the defocus difference between the top and bottom of the sample. While this idea was around for a long time, only in recent years tools were developed that can run in reasonable time and significantly improve the final resolution<sup>23,65</sup>. Depending on the software, 3D-CTF might be estimated and corrected at different levels (tilt image, full tomogram or subtomogram), and may be able to be refined during refinement.

Due to the limited range of tilt angles collected in typical cryo-ET workflows, not all views of the sample are represented; when reconstructing the 3D FT of the sample, this is clearly visible in Fourier space as a wedge of missing information (**Figure 2.3**). The missing wedge introduces several problems in downstream processing: it blurs the tomogram in the Z direction, biases subtomogram alignment, and leads to anisotropic resolution for objects with preferential orientation.

If fiducials (or other high-contrast objects of no real interest) are present in the sample, it is often useful to mask them during reconstruction, in order to avoid the high-contrast artifactual streaks caused by the missing wedge, which can impair the interpretability of the tomogram<sup>23,66</sup>.

The high contrast artifacts and information void caused by the missing wedge can make visualisation and annotation of the data difficult. For this reason, tools have been developed that are able to “fill in” the missing information, improving the visual quality of the tomograms<sup>67,68</sup>. While such tools may drastically improve the experience when visualising or annotating data, it’s important to not over-interpret the outputs or use them for later steps, lest introducing generated data into the processing.

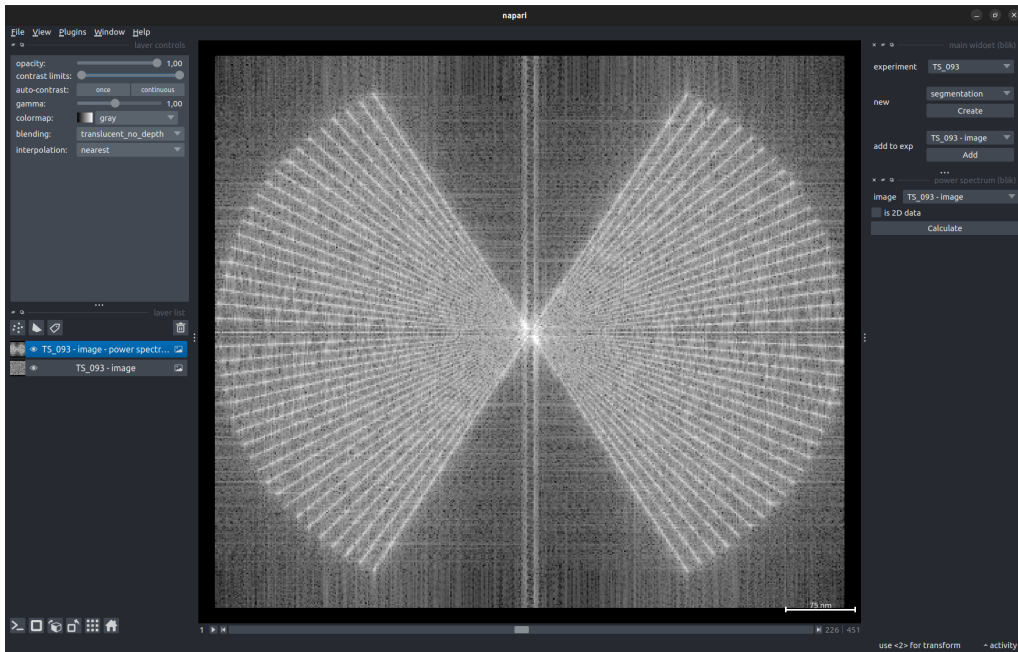


**FIGURE 2.3: Missing wedge.** 2D slice through the 3D FT of a tomogram, perpendicular to the tilt axis. The 2D FT of images of the tiltseries are visible as lines at regular angular spacing; at the top and bottom they are not present, creating the missing wedge.

## 2.5 Annotation and segmentation

Thanks to the *in situ* and quasi-native nature of tomography data, it is often useful to annotate or segment tomograms in order to get a better view of the morphology of the sample, or to find areas and particles of interest more easily.

One of the most common approaches is to do semantic segmentation (aka labeling), where individual voxels are assigned a type — “membrane”, “ribosome”, and so on, though usually in the form of a integer — either by manually painting over the sample, or automatically via image processing algorithms or ML tools. Labeling helps with visualisation by boiling down the sample to its most fundamental components, while also serving as a powerful tool for quantitative and morphological analysis of complex mesoscale objects. To this end, segmentations are often used as starting point for other kinds of annotations, such as abstracting membranes or

filaments to mathematical objects like splines and skeletons<sup>69</sup> in order to calculate properties such as membrane curvature, filament branch length, and so on.

In some projects, morphology is all that matters, with no need to reach high resolution; in such cases, the cryo-ET pipeline can stop after annotation. Where high resolution molecular structures are the goal, segmentations and other annotations may also be used as a starting point for particle picking.

## 2.6 Particle picking

Picking particles in tomograms is not so different from picking particles from 2D micrographs, other than having an extra dimension. Manual picking and template matching are still the preferred methods, though more and more software is developed for ML-based or hybrid methods<sup>30,31,70,71</sup>.

As with most things in cryo-ET, low SNR is the main obstacle to overcome; this is why some picking tools — such as the one developed during this thesis (**Chapter 3: blik: a cryo-ET visualisation and analysis tool**) — attempt to use as much prior knowledge about the system as possible in order to limit the degrees of freedom when searching for particles<sup>31,60,72</sup>.

Having a 3rd dimension also contributes to making visualisation and annotation harder: particles and structures don't simply lay on a flat plane, and the user interface in software becomes trickier. Additionally, the missing wedge constitutes an obstacle to annotation, especially for features that are oriented along the microscope axis.

Whenever possible, segmentation or other kinds of annotation can be used as baseline for particle picking: either by masking areas of interest — such as picking only inside a certain cellular structure — or by seeding particle picks based on the annotation geometry — such as distributing particles on the surface of a membrane. Such information may also be used to initialize the particle orientation to something self-consistent (e.g: all perpendicular to the membrane); this can affect drastically the initial model generation and subsequent refinement, where 3D rotational search may otherwise not overcome the SNR.

## 2.7 Subtomogram averaging

In cryo-ET, the equivalent to SPA's 2D classificatin and 3D refinement is subtomogram averaging (STA). The idea at the core is the same: by combining the data from many subvolumes extracted from the tomogram (subtomograms) which contain copies of the same object, the SNR can be drastically improved. The basic procedure is also very similiar to SPA, only in 3D: subtomograms are extracted from the full reconstructed tomogram based on the positions of the particle picks; then, rounds of cross-correlation and refinement (and/or classification) improve the model until convergence ([Section 1.6: 2D classification](#)).

In recent years, however, the field is moving away from this naive approach where “rigid” subtomograms are extracted from a full 3D reconstruction, in favor of what is sometimes called **per-particle tilt series**<sup>23,64,73,74</sup>. Differently from the naive method, subtomograms are reconstructed on-the-fly directly from the 2D data, using spatio-temporally adjusted parameters (such as CTF and tilt-series alignment) at the subtomogram level. This opens up many avenues for optimization — such as 3D-CTF correction ([Section 2.4: Tomogram Reconstruction](#))<sup>65</sup>, multi-particle refinement<sup>45</sup> or bayesian polishing<sup>74</sup> — by allowing the subtomogram reconstruction parameters to be tweaked after the first reconstruction ([Section 1.8: Refinement](#)).

A significant obstacle during alignment is caused by the missing wedge; it is such a prominent feature that during cross-correlation, it would normally overpower everything else in the subtomograms. Because of this, subtomograms would end up being rotationally aligned based on how they are rotated relative to the missing wedge, instead of their relative rotation to each other. For this reason, missing wedge compensation is a crucial step for the success of STA procedures<sup>75</sup>.

## 2.8 Pros and cons

Cryo-ET has seen a rapid development in recent years, bringing it to the forefront of structural biology techniques.

By providing a high resolution, *in situ* view of biological systems, it brings insights that other *ex situ* techniques like X-ray crystallography and SPA cannot provide. At the same time, thanks to STA, cryo-ET is able to bridge the gap with single particle analysis, reaching in some cases sub-nanometer resolution for single particle structures, while maintaining the ability to contextualize such structures within the complex biological system they belong to.

A distinctive strength of cryo-ET is the ability to explore mesoscale systems or superstructures — such as folded 2D lattices and filaments — without trivializing them for bottom up, *in vitro* reconstitution, and instead observing their structural arrangement as it behaves *in situ*.

Many of cryo-ET's limitations are ultimately ascribable to the low SNR; some of them can be overcome with hardware improvements (better sample preparation, detectors and phase plates), and others with software advances (chromatic aberration correction, better alignment and refinement procedures). In recent years, several groups are working on developing new hardware and software for cryo-EM and cryo-ET, steadily improving the attainable resolution ([Figure 2.4](#))<sup>76</sup>.

Another common hurdle, especially for researchers new to cryo-ET or programming, is presented by the budding, messy and fragmented software ecosystem.

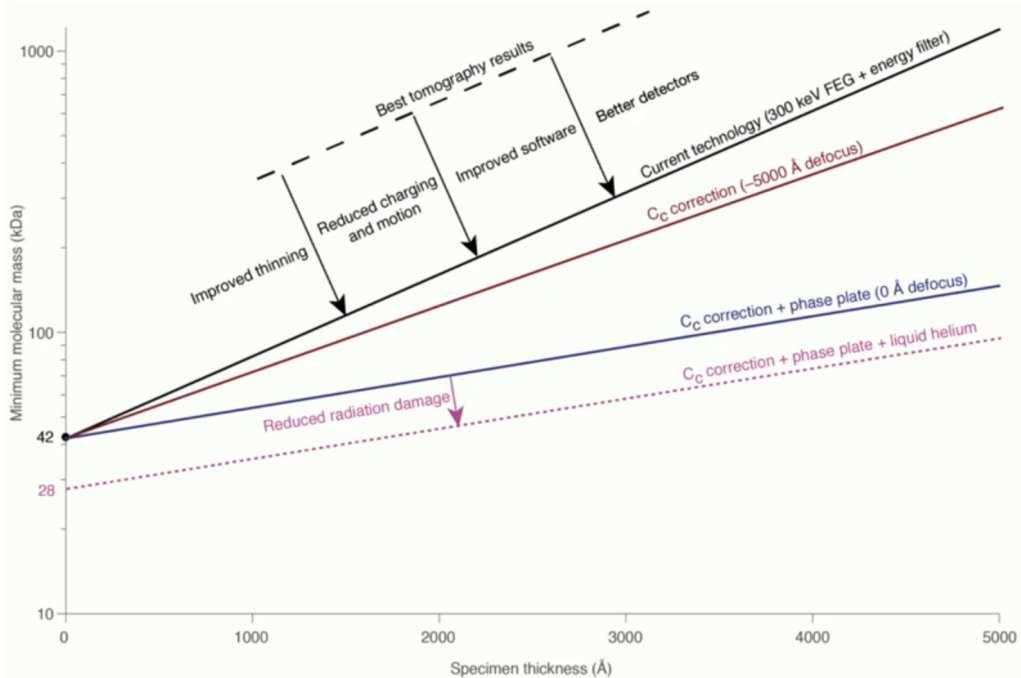


**FIGURE 2.4: Particle size limit versus sample thickness.** Theoretical lower limit of particle size that can be resolved from cryo-EM data, depending on the sample thickness. Currently, even the best tomography results are far from the theoretical limits due to lack of optimization in sample preparation and hardware. The current theoretical limits can yet be improved by implementing some additional methods. Figure taken from Russo<sup>77</sup>.

# **Part II**

# **Results**

# Chapter 3

## blik: a cryo-ET visualisation and analysis tool

In most scientific fields, the ability to visualize and interactively explore one's data is crucial to forming an understanding of the analysed system, and for hypothesis generation. Fields working with higher dimensional data, such as cryo-ET, benefit especially from interactive visualisation, as static plots and 2D images are often unfit to capture the full scope of the system.

Unfortunately, as cryo-ET workflows become more and more automated and software tools become more abstracted from the data itself, it is easy — and tempting — to follow entire processing workflows while rarely looking at the data other than through summaries or final results. This is often encouraged by the monolithic software suites currently dominating the field, making it harder to implement and use custom tools to inspect or intervene at any one point of the workflow.

The development of blik and my ongoing contribution to the napari community<sup>78</sup> started as a way to address these issues and enable myself and others to ergonomically and visually interact with the data at any point of the processing pipeline.

What follows is our paper published in PLOS Biology on April 30 of 2024, which summarizes the capabilities of blik and the development that went

into it and the surrounding ecosystem. Following the paper is a summary of more recent developments and uses of blik ([Section 3.10: Addendum](#)).

## Contents

Contents .....	38
3.1 Abstract .....	39
3.2 Introduction .....	40
3.3 Results .....	43
Visualisation .....	44
Images and Volumes .....	44
Particles .....	46
Input/Output .....	47
Image segmentation .....	48
Filament and surface generation .....	50
Filaments .....	50
Surfaces .....	51
Resampling .....	52
Particle picking .....	53
Scipion Integration .....	54
3.4 Discussion .....	55
3.5 Conclusion .....	58
3.6 Materials and methods .....	59
cryotypes and cryohub .....	59
morphosamplers .....	60
napari plugins .....	61
napari and vispy .....	61
blik .....	62
3.7 Acknowledgements .....	62
3.8 Data availability .....	62
3.9 Funding .....	62
3.10 Addendum .....	64

# blik is an extensible 3D visualization tool for the annotation and analysis of cryo-electron tomography data

Lorenzo Gaifas<sup>1\*</sup>, Moritz A. Kirchner<sup>1</sup>, Joanna Timmins<sup>1</sup> & Irina Gutsche<sup>1,2\*</sup>

<sup>1</sup> Institut de Biologie Structurale, Université Grenoble Alpes, CEA, CNRS, IBS, Grenoble, France.

<sup>2</sup> Department of Chemistry, Umeå University, Umeå, Sweden.

\* Corresponding authors.

## 3.1 Abstract

Powerful, workflow-agnostic and interactive visualisation is essential for the ad-hoc, human-in-the-loop workflows typical of cryo-electron tomography (cryo-ET). While several tools exist for visualisation and annotation of cryo-ET data, they are often integrated as part of monolithic processing pipelines, or focused on a specific task and offering limited reusability and extensibility. With each software suite presenting its own pros and cons and tools tailored to address specific challenges, seamless integration between available pipelines is often a difficult task. As part of the effort to enable such flexibility and move the software ecosystem towards a more collaborative and modular approach, we developed blik, an open-source napari plugin for visualisation and annotation of cryo-ET data (source code: <https://github.com/brisvag/blik>). blik offers fast, interactive, and user-friendly 3D visualisation thanks to napari, and is built with extensibility and modularity at the core. Data is handled and exposed through well-established scientific Python libraries such as numpy arrays and pandas dataframes. Reusable components (such as data structures, file read/write, and annotation tools) are developed as independent Python libraries to encourage reuse and community contribution. By easily integrating with established image analysis tools – even outside of the cryo-ET world – blik provides a versatile platform for interacting with cryo-ET data. On top of core visualisation features – interactive and simultaneous visualisation

of tomograms, particle picks and segmentations – blik provides an interface for interactive tools such as manual, surface-based and filament-based particle picking and image segmentation, as well as simple filtering tools. Additional self-contained napari plugins developed as part of this work also implement interactive plotting and selection based on particle features, and label interpolation for easier segmentation. Finally, we highlight the differences with existing software and showcase blik’s applicability in biological research.

## 3.2 Introduction

Cryo-electron tomography (cryo-ET) is a powerful three-dimensional (3D) cryo-electron microscopy (cryo-EM) imaging technique for visualisation and structural analysis of biological samples *in situ*<sup>49</sup>. In recent years, rapid development of software for cryo-ET data processing and analysis has brought great advances in tools for tilt series alignment<sup>61</sup>, particle picking<sup>30,70</sup>, averaging and classification routines<sup>23,45,74</sup>, denoising<sup>26,27</sup>, and more<sup>63</sup>. Thanks to subtomogram averaging, cryo-ET is now routinely used to determine the structure of biological macromolecules *in situ*, achieving in the most favorable cases sub-nanometer resolutions<sup>65,79</sup>.

While more and more powerful, existing workflows still rely on extensive human intervention due to the high heterogeneity of requirements and samples<sup>80,81</sup>. Powerful and user-friendly visualisation tools are needed for effective human-in-the-loop pipelines to minimise the friction at the human-machine interface, and should be composed of modular and extensible software, to maximise reusability and simplify integration of different existing toolkits.

A common practical challenge encountered by scientists working on cryo-ET data is indeed the (in)compatibility between different software tools. Some of the most widespread cryo-ET software suites (such as IMOD<sup>82</sup>, PEET<sup>58,59</sup>, Relion<sup>28</sup>, Dynamo<sup>40</sup>, emClarity<sup>73</sup>, and PyTom<sup>83,84</sup>) all use different file formats for particle poses and tilt series metadata. This constitutes a barrier for users who need to use features from different tools

on the same data: at best, users might miss out on important features from other software; at worst, integration may silently go wrong and cause issues in later steps. Entire software suites such as Scipion<sup>85</sup> are devoted to integrating normally incompatible cryo-EM and cryo-ET software into pipelines.

With useful features scattered among different programs (e.g: Are-Tomo’s unsupervised alignment<sup>61</sup>, Topaz’s denoising<sup>26</sup>, CrYOLO’s filament picking<sup>30</sup>, EMAN2’s trainable segmentation<sup>63</sup>), and numerous small custom scripts developed by researchers tailored to a specific project’s needs (distributing or selecting particles, improving alignments, etc), software integration is a real and common concern.

Even when a compatible tool is available or conversion possible, it is often hard to tell when it worked properly due to lack of generalised visualisation tools for inspecting and validating data throughout the pipeline. Due to the aforementioned compatibility restrictions, popular software suites (such as IMOD and Dynamo) often provide built-in visualisation tools, duplicating development efforts and further deepening the separation between pipelines.

Finally, many existing visualisation tools are not easily hackable by users to extend them with custom functionality. Even those that offer ways to extend their functionality (such as ChimeraX<sup>86</sup> through its Python API or Dynamo with MATLAB<sup>87</sup> code), provide limited interface to data and rendering code, or require considerable programming skills to do so.

To address these issues, we present blik, a new software for interactive visualisation, manipulation and analysis of cryo-ET data. The code is open-source and welcomes community contributions at <https://github.com/brisvag/blik>. blik is a plugin for napari<sup>78</sup> (<https://napari.org/>), a visualisation software focused on scientific imaging, with data segmentation and annotation available as core features. It has both a programmatic and a graphical interface, allowing for seamless integration of interactive visualisation and scripted pipelines. napari offers great customisation options, powerful built-in tools and a growing plugin ecosystem, which

allows blik to focus on specific cryo-ET needs.

To address the challenges listed above, blik’s design choices, features, and architecture reflect the following primary goals:

- **Compatibility:** blik can read and write data in file formats from a variety of different software suites, including IMOD, Relion, and Dynamo. This makes it easy to switch between tools or to integrate custom scripts into a workflow.
- **Interactivity:** blik provides interactive visualisation that allows users to explore data programmatically and visually at the same time. Data is always accessible through a standard Python console and in simple, well established formats such as numpy arrays and pandas dataframe. This makes it easy to validate data during processing and to identify problems as soon as they arise, as well as to provide a framework for quicker prototyping and debugging of new workflows.
- **Hackability:** blik is open-source and easy to extend with custom functionality. This allows users to tailor the software to their specific needs. The napari plugin ecosystem also allows taking advantage of many existing analysis tools, even from different imaging fields. Additionally, blik’s Input/Output (IO) capabilities are easily extensible by users to include new custom formats.
- **User-friendliness:** blik’s, and most of napari’s, functionality are also exposed in the Graphical User Interface (GUI), making it also easy to use for non-programmers.
- **Performance:** thanks to napari’s visualisation backend vispy, blik has performant rendering which can handle large 3D (and more) datasets, even larger-than-memory thanks to dask.
- **Community:** to foster community contribution, code reuse, and jumpstart other projects, many contributions were upstreamed to napari, vispy, or extracted into simple single-use libraries usable by other projects ([teamtomo](#)).

The use of Python for the development of blik and napari is crucial to further these goals. In the last years, the integration of scientific Python in high school and university educational curricula played a pivotal role in its democratisation. The surge of popularity of the scientific Python ecosystem with modular and reusable tools is largely due to its versatility, readability, simplicity, extensive documentation and a wide community support.

This makes blik a convenient entry point for cryo-ET-interested newcomers and lowers the barrier for the creative leveraging of basic programming skills for their everyday research and applications, enabling individuals with varying levels of programming experience to quickly grasp and implement solutions.

Moreover, the scientific Python ecosystem is well-established in many imaging fields, and is becoming a player in the cryo-EM and cryo-ET world. By adhering to the practices and conventions of this ecosystem, blik allows to easily integrate many available field-agnostic tools (e.g: scikit-image and scipy for image and annotation processing, pytorch and the plethora of Python machine-learning (ML) tools for several types of analysis), take advantage of existing solutions and avoid the tendency to “reinvent the wheel” that scientific software can often be prone to.

Finally, to help users to seamlessly integrate blik into their existing workflow, blik is currently being integrated into Scipion as a plugin (<https://github.com/scipion-em/scipion-em-blik>).

### 3.3 Results

The following sections describe all the features provided by blik and their implementation details. To help users get started with blik, we provide a supplementary tutorial that explains the blik user interface and offers practical guidance on using each tool in a cryo-ET workflow. This tutorial, together with a more comprehensive and up-to-date documentation, is hosted at <https://brisvag.github.io/blik/>.

## Visualisation

blik relies on napari for performant visualisation. The napari core is field-agnostic, and requires the development of custom readers and writers to convert specific file formats into a napari visualisation. This has been an important focus of blik so far, through the development of cryohub and the napari representation of particle poses as oriented points.

Data in napari is exposed as layers that can be controlled individually (similarly to general image processing software like GIMP or Adobe Photoshop). There are several types of layers; the main ones used by blik for visualisation purposes are Image for images and volumes, and Points and Vectors for particle poses.

### Images and Volumes

Images, image stacks and volumes in the most common formats (.tif, .mrc, .em, .hdf) can be opened and viewed both in 2D as slices (**Figure 3.1A**) and in 3D as volumetric projections (**Figure 3.1B**), isosurfaces (**Figure 3.1C**) and more. It is possible to change colormaps, contrast limits, gamma and other basic image visualisation parameters. 3D visualisation also allows for slicing the volumes at arbitrary planes (**Figure 3.1D**), similar to IMOD's slicer tool.

blik also provides some widgets with extra functionality to complement image visualisation:

- A basic GPU-accelerated filtering tool (gaussian blur) for 2D images and 2D slices that is computed on the fly and whose parameters can be regulated with sliders. Simple gaussian filters are frequently used in image visualisation, especially with noisy cryo-EM data. While generating a filtered image is a relatively fast procedure, it is rarely fast enough to be computed on the fly on a CPU. GPU-accelerated filtering allows switching on and off on the fly, as well as changing kernel size and sigma, without having to generate a new image. While blik exposes only gaussian filtering, the underlying logic was

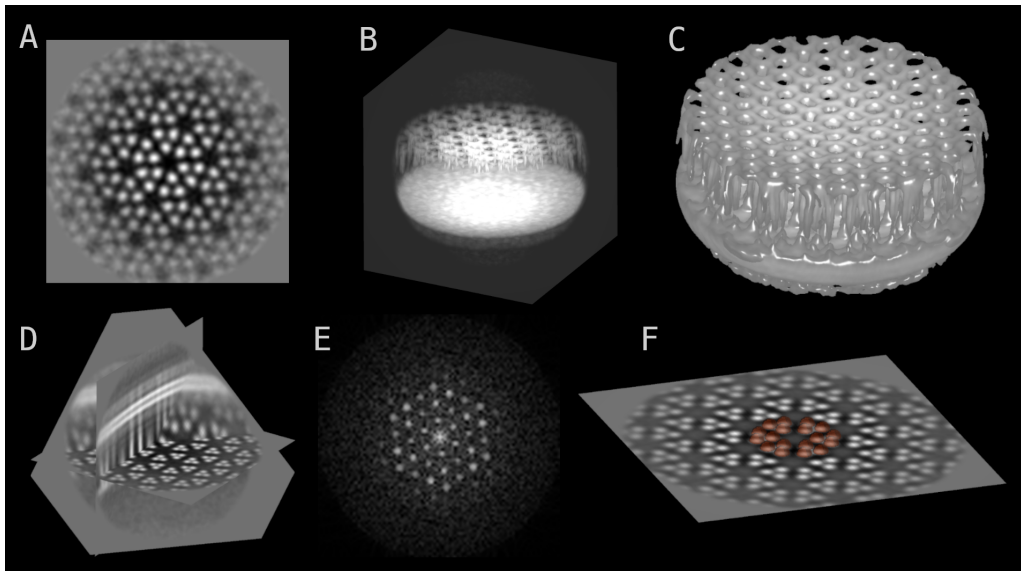


**FIGURE 3.1: Volume visualisations.** Showcase of the image visualisation capabilities of napari and blik. Chemoreceptor arrays of the *E. coli* minicells<sup>88</sup> are used for illustrative purposes throughout the figures. A. 2D slice through a 3D volume. B. Maximum intensity projection of the 3D volume. C. Isosurface. D. Arbitrary 3D plane slicing in 3D view. E. 2D slice through the 3D power spectrum of the volume. F. Segmentation (in semi-transparent brown) of 3D objects.

implemented in the vispy OpenGL shader allowing for arbitrary convolutional kernels. Firstly, the image texture is sampled in a NxM grid (for a kernel of shape NxM) centered around the texture coordinates. A weighted average is then computed based on the kernel weights and the resulting value is forwarded to the rest of the shader.

- A power spectrum widget, which quickly computes the power spectra of single images, stacks or volumes (Figure 3.1E). Power spectra are a fundamental tool for data inspection and validation in cryo-EM, from estimating resolution, to generating hypotheses about symmetry, to finding caveats in the data collection procedure. Like any other computation made by blik or napari, the power spectrum is then available as a normal numpy array for further use from within Python or to export to the available formats.

Additionally, masks and pixel-based segmentations (often called just

“segmentations”, or “labels” in napari jargon) are easily displayed (and modified with all the tools provided by napari, such as free-hand painting, even in 3D) by using the napari Labels layer, which is designed specifically to work with segmentation data (binary or integer arrays) ([Figure 3.1F](#)). Label processing is a particularly thriving area of the napari ecosystem, albeit mostly in the field of fluorescence and optical microscopy. This is a great opportunity for knowledge sharing and code reuse between fields that otherwise are typically relegated to separate software pipelines.

## Particles

Particle data (coordinates, orientations, and any additional features and metadata) can be loaded from common formats (.star, .tbl). Coordinates are visualised as spheres, and orientations as basis vectors centred on the spheres ([Figure 3.2](#)). Both components can be disabled or tweaked (such as color-coded or resized, labeled, etc.) for better visualisation. As with images, particles can be easily viewed in 3D.

Since particles are actually simple napari Points layers, everything in the napari ecosystem that works with points will work with particles, such as manual or automated selection based on features, editing and coloring, classification, etc. Once again, the wealth of cross-field contributions towards the napari ecosystem is a valuable asset for processing data.

For example, points (and thus particles) may hold extra metadata in their features data frame, such as classification results or quantitative values such as a confidence score. All such features can be used to encode visualisation parameters like color, rendered symbol (sphere, square, cross, etc.) and size, facilitating data inspection and selection of suitable candidates for further processing.

To fully take advantage of this, shipped as part of blik — but developed as a standalone field-agnostic napari plugin — is the napari-properties-plotter plugin, which allows interactive plotting of per-point features ([Figure 3.2, bottom widget](#)), such as Relion’s figure of merit, classification results, resolution estimates, etc. Distribution histograms or scatter plots

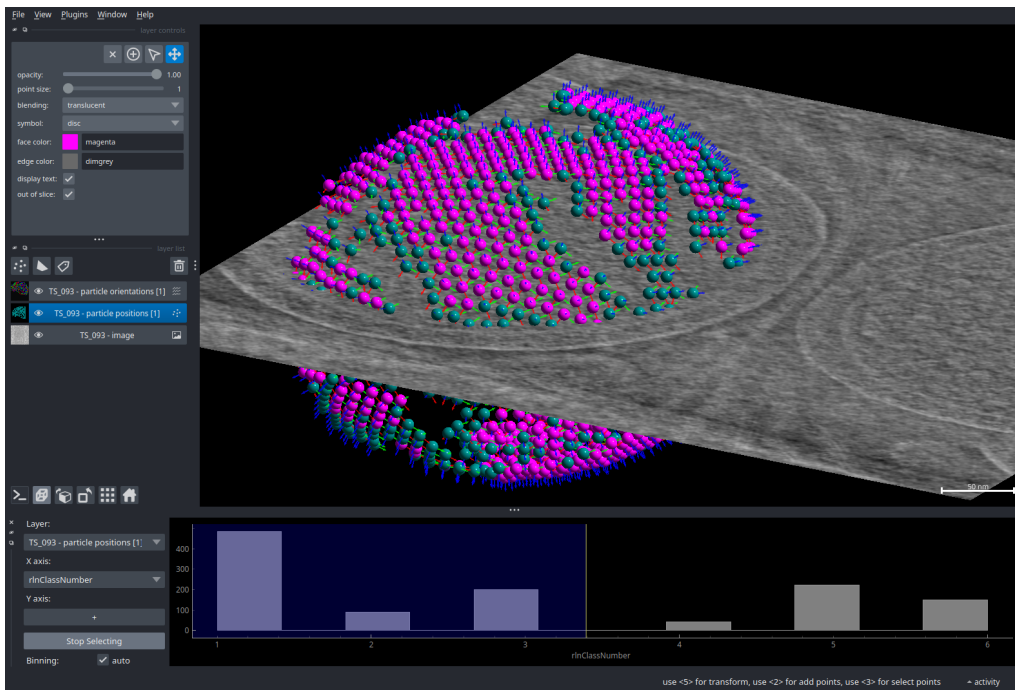


**FIGURE 3.2:** 3D particle visualisation and feature plotting. Particles are from a Relion 3D classification of chemoreceptor arrays of the *E. coli* minicells<sup>88</sup>. Orientations are displayed with the three basis vectors in red/blue/green. The properties-plotter widget (bottom) shows a plot of a Relion data column – in this case, the rInClassNumber – as a histogram. By selecting an area of this plot, the corresponding subset of particles is selected. This can be then used for further processing; in this case, selected particles are coloured differently (in magenta), showing that the selected classes contain mostly particles from the core of the chemoreceptor array lattice.

with any combination of features as axes can be automatically generated by simply selecting the desired features. Moreover, by picking subsections of such plots, particles can then be selectively rendered, modified, saved and otherwise processed.

## Input/Output

The reading, writing and conversion logic used by blik was developed as a standalone library, [cryohub](#). This library has a modular design to allow reuse in other applications and simplify the contribution of new formats. Currently, it supports the following formats for images and segmentations:

- .mrc (and the .mrcs, .st, .map, .rec variants)
- .tif(f)
- Dynamo .em
- EMAN2 .hdf

and the following formats for particles:

- Relion .star (Relion  $\geq$  3.0)
- Dynamo .tbl
- CrYOLO .cbox and .box
- EMAN2 .json

Where possible, blik makes use of lazy loading via dask<sup>89</sup>, which allows working with data that is larger-than-memory and loading full datasets at once for ease of browsing.

## Image segmentation

A few annotation and analysis tools were implemented as part of blik or standalone napari plugins.

The napari community has already developed numerous plugins for segmentation and annotation of 2D and 3D imaging data, spanning from manual annotation and traditional image-processing-based segmentation to AI tools. blik's current contributions to this ecosystem are in some cases general-purpose – such as utilities for manual annotation of volumetric segmentations – and in other cases focused on cryo-ET-specific issues that are not easily solved by existing methods – such as rigorous geometry-based particle picking on filaments and surfaces.

Pixel-based image segmentation is already natively supported in napari through the Labels layer, with mature tools for editing, data exploration and annotation. One previously missing feature is the ability to easily interpolate labels from sparsely annotated 2D slices of a 3D volume into full 3D volumetric labels. blik brings a standalone plugin for this purpose called napari-label-interpolator ([Figure 3.3](#)), which works with any

Image layer and interpolates n-dimensionally (e.g: it can interpolate 3D labels over a time series).

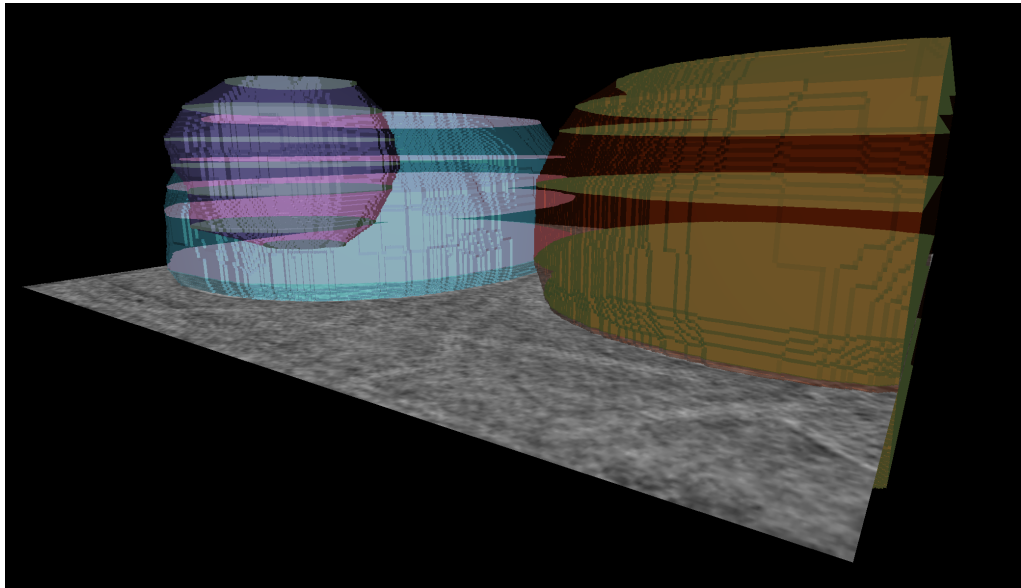


**FIGURE 3.3: Interpolated segmentations.** A tomogram is manually annotated on a few 2D slices using the napari labels painting functionality. These sparsely annotated 2D slices are then interpolated with the label interpolator widget to generate a volumetric segmentation of multiple objects.

The plugin works by interpolating Signed Distance Fields (SDF) across multiple n-dimensional slices. For each annotated slice along the interpolation dimension and for each label, the (n-1)-dimensional SDF is computed. SDF slices are then linearly interpolated with a simple weighted average, with weights proportional to the distance from the neighboring annotated slices. Where the weighted average is greater than zero, the voxel is considered to be part of the interpolated label.

This system plays very well with volumetric annotation, but has limits with thin labels such as filaments or surfaces. We plan to add different types of interpolation in order to widen the scope of application and usability of this tool.

## Filament and surface generation

A different kind of image segmentation uses mathematical representations such as filaments, surfaces and fields to describe morphological features. In this context, blik contributions were made to a general-purpose library at [morphometrics-morphosamplers](#), which aims to provide generalised morphological descriptions and sampling for scientific imaging. Specifically, we developed a helical filament model based on parametric splines, as well as a parametrised spline-grid surface model which allows to rigorously annotate surface-like objects such as membranes from simple point annotations.

The morphosamplers code was implemented with two main goals: keeping the manual annotation procedure simple and robust, and generating ordered, regularly spaced poses that can be used both for particle picking for subtomogram averaging and to allow volume resampling ([Section 3.3: Resampling](#)). Picking particles as a regularly spaced lattice can significantly improve the results of subtomogram averaging when it reflects the underlying geometry of the sample<sup>60,80</sup>. Model picking tools in Dynamo<sup>40</sup> had a strong influence on the purpose and functionality of blik; unlike the Dynamo mesh-based approach, the spline-based implementation aims to optimise regular Euclidean spacing and consistency in initial particle positioning and orientations.

### Filaments

Filament picking ([Figure 3.4](#)) uses a relatively simple single-spline approach:

- Points are picked manually in 3D space along the filament.
- A spline representation is generated, parametrised so that samples are equidistant in Euclidean space.
- Given a specific rise and twist, particles are generated along the spline in a helical pattern.
- If a radius is given, the particles are shifted away from the spline by that amount.

- If a symmetry group is given, symmetric copies are created around the filament axis.

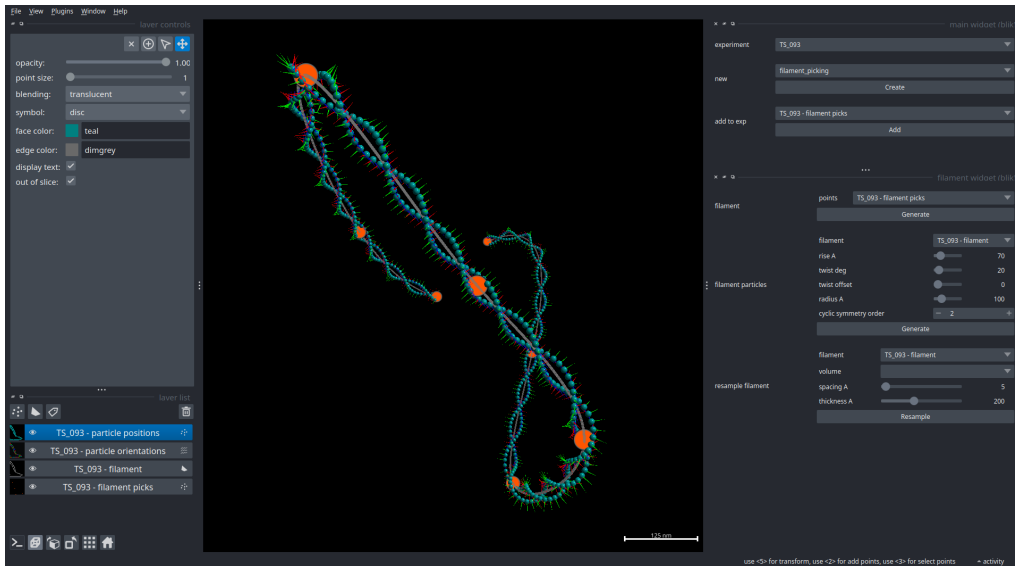


**FIGURE 3.4:** Filament-based particle picking. Particle picks along a helical filament generated by blik. Starting from simple points picked manually along the desired path (orange points) and using the filament widget (on the right), a spline representation is computed (grey) and used to generate particle poses (cyan spheres with basis vectors) according to the given helical parameters defined in the widget.

## Surfaces

The surface generation uses the same underlying parametric spline logic as filaments, but creates a grid of splines to capture the surface shape ([Figure 3.5](#)). The procedure can be broken down into the following steps:

- A few points are picked along the desired surface, repeating at different Z-slices.
- For each Z-slice annotated as such, a parametric spline (with desired interpolation order and smoothing) is computed.
- Points are distributed uniformly on these splines, ensuring equidistance in Euclidean (and not parametric) space.

- The resulting strips of points are then aligned by minimising index-wise distances, and padded to enforce a rectangular grid.
- New splines are then computed, by using the generated points as control points. This results in parallel splines, perpendicular to the first set and equidistant from each other.
- New points are then generated on this second group of splines, similarly to the first round, equidistant in Euclidean space. This results in a full rectangular grid of equidistant points.
- A third group of splines is generated in the same orientation as the first group.
- The second and third group of splines are used to compute the derivatives; this gives — for each point on the surface — two vectors tangent to the surface and perpendicular to each other. With these, normal vectors are calculated, giving the full orientation of each particle on the surface.

Parameters such as interpolation order, inter-particle distance, and smoothing can be controlled, allowing fine-tuning of the generated surface.

While this approach is advantageous for relatively regular surfaces, for which the generated grid of splines provides uniformly spaced and oriented points on the surface, its main downside is that complex surfaces will inevitably deform the grid. This method struggles especially with strongly irregular surfaces, such as membranes with numerous invaginations located at different Z-slices.

### Resampling

The grid-like, regularly spaced nature of these models can be additionally used to create visualisation aids (meshes and filaments) and to resample the annotated volume along the annotated object. Such volume resampling can be useful for quantitative and spatially consistent volume analysis of otherwise complex 3D objects; density profiles of a complex 3D surface can thus be generated while retaining spatial information. In practice, this can

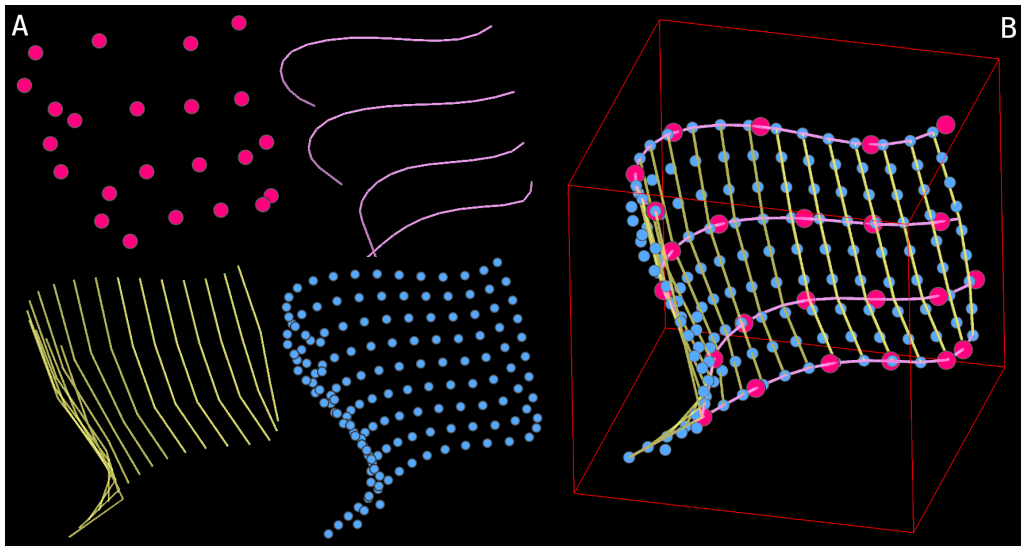


**FIGURE 3.5: Surface generation procedure.** A. Step-by-step procedure used by blik to generate surfaces. An initial set of points (magenta) is picked on a few Z-slices following the desired surface. A first set of splines (purple) is generated within each Z-slice, and then used to generate equidistant samples which become the nodes of the next set of splines, perpendicular to the first (yellow). The second set of splines is then resampled with the same spacing, thus generating a final set of grid-like, evenly spaced samples. B. All the steps combined.

also be used to aid visualisation, by “straightening” an otherwise curved surface.

## Particle picking

blik provides a few tools for picking particles for subtomogram averaging. All such particles can then be saved in the formats implemented by cryohub for further processing.

The most basic picking tool is a manual picker; simply clicking points on an image or volume slice will generate a particle in that position. Manually modifying the orientation is not yet implemented, but is planned for a future release.

For more complex picking, the aforementioned filament and surface models can also be used to generate particles ([Figure 3.7](#)). These will be regularly distributed on the surface with a provided inter-particle spacing,

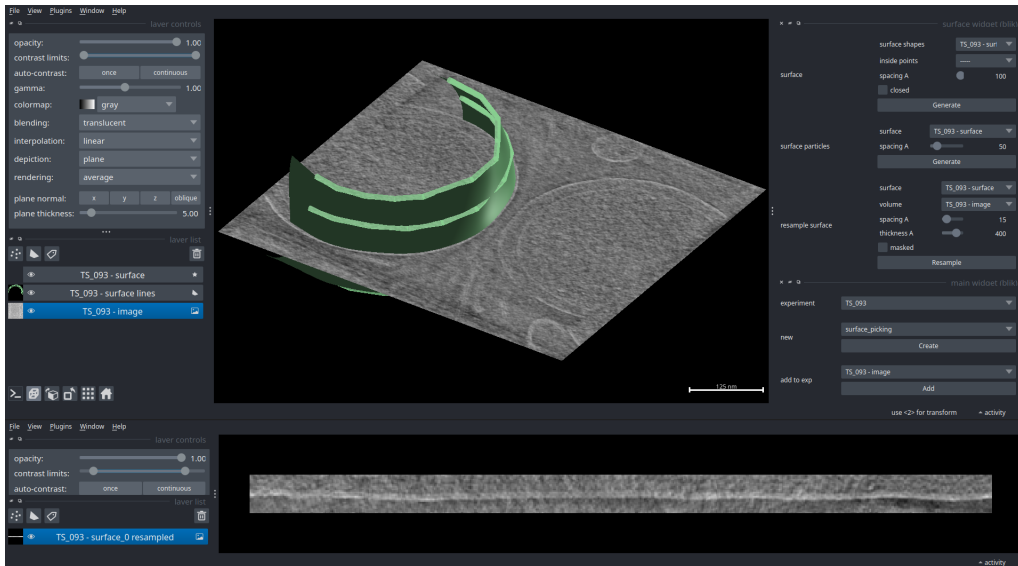


**FIGURE 3.6: Surface-based volume resampling.** **Top:** a surface is generated using the surface widget, following the shape of a minicell membrane. The tomogram volume is then resampled based on the picked surface and a few parameters set in the widget, such as sample thickness and pixel spacing. **Bottom:** the result is a 3D volume containing a “straightened” version of the picked surface, displayed here averaged along Z into a 2D image.

and oriented with their Z basis vector along the filament axis, or the normal of the surface. This is useful for initialising particle picks for objects following an underlying geometry, such as helical filaments and membrane proteins, and is particularly suited for dense lattices.

## Scipion Integration

To ease the integration of blik into existing workflows, we also release a **blik Scipion plugin**. This plugin exposes all of blik’s main functionalities (visualisation, segmentation and particle picking) as Scipion protocols which can be used in combination with all the existing tomography protocols provided by Scipion and other plugins.

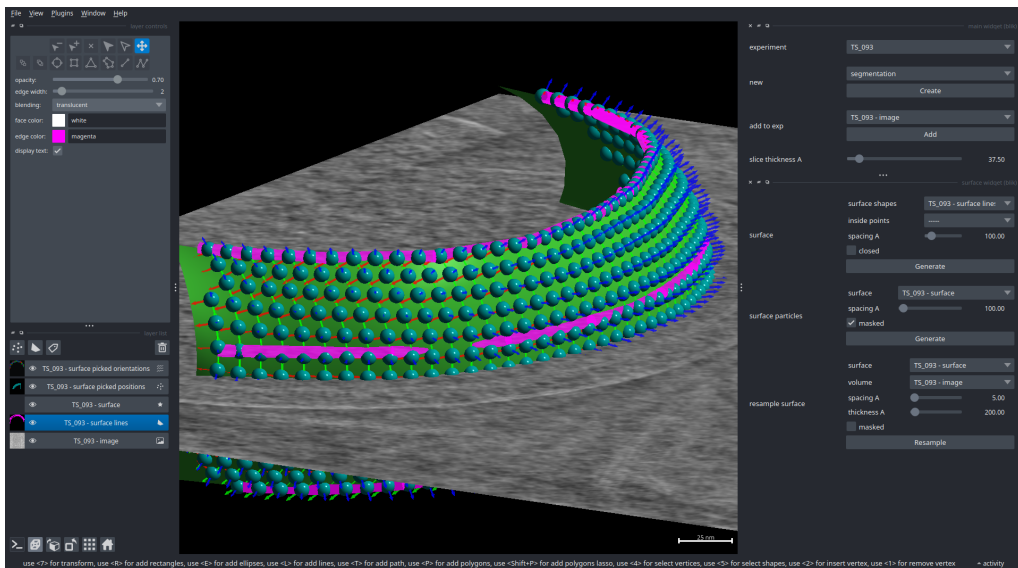


**FIGURE 3.7: Surface mesh and particle picks.** A surface is generated using the surface widget, starting from the manually picked lines (magenta) which follow the shape of a chemosensory array. The generated surface is displayed as a mesh (green). Particles for subtomogram averaging (cyan spheres and red/green/blue basis vectors) are then generated based on a few parameters set in the surface widget (on the right).

## 3.4 Discussion

With blik, we add to the cryo-ET software ecosystem an integratable and interactive data viewer, radicated in the Python ecosystem, and a reusable and extensible set of libraries and tools for annotation and picking. There are several existing tools with similar goals and functionality to blik; in this section, we discuss the most widely-used options known to us, examine their compatibility with blik and compare their features with our tool. This should provide a starting point for the reader to choose the appropriate tool for their project.

blik was tested primarily to work within the Relion&Warp pipeline<sup>28,45,80</sup>, but was designed to be workflow-independent and thanks to cryohub easily extensible with new data formats. Following this workflow, other than the ubiquitous .mrc image format and Relion's .star particle format, one of the first compatibilities to be developed was with image and particle data

from the MATLAB software suite Dynamo<sup>40</sup> and its processing pipeline. Dynamo provides its own visualisation and picking tools, which were also the main inspiration for the geometry-based filament and surface particle generation in blik. While particle picking in blik has currently a smaller scope compared to Dynamo, its implementation in Python is intended to be more easily maintained and extended in the future by users, while leveraging the full-featured napari visualisation.

IMOD<sup>82</sup> is arguably the giant in the field, with a long history of development and a wealth of features for image processing and annotation. Given its extensive capabilities and the constant development, it is usually the first choice when it comes to cryo-EM/ET processing, visualisation, and annotation. Many of these features are very useful, and we plan to add support for them in blik or napari in the future. Integration between blik and IMOD is seamless for most common operations, such as working with data processed through IMOD’s tomography pipeline etomo. IMOD’s 3d viewer 3dmod is full-featured and fast, and has several modes for 2D projection and slicing. It has however a more limited 3D renderer compared to napari (no volumetric projections, slicing planes in 3D view, or native particle pick viewer), which limits its applicability for the inherently 3D work of tomography. Being written in C, it is also non-trivial to extend for users with limited programming knowledge.

ThermoFisher’s Amira<sup>90</sup> is also a popular choice for image visualisation and annotation. It is particularly appreciated for its easy-to-use labeling tools to improve manual annotation and tracing, such as label interpolation, and image-guided picking. Amira’s label interpolation was the main inspiration behind napari-label-interpolator, and image-guided picking is in the future plans for blik development. Being an image-focused tool, Amira is more limited when it comes to particle coordinate generation although it has some model-based filament picking that can be repurposed for particle generation with the help of user scripts. However, Amira’s closed-source proprietary nature is a big downside for open science practices, making it hard or impossible to extend, contribute to, and freely share within the scientific community.

EMAN2<sup>63</sup> is a full software suite with an entire tomography pipeline from raw data to reconstruction. I/O compatibility between EMAN2 and blik is partially implemented, allowing to read particles and tomograms. EMAN2 has some tools for visualisation and picking, and is especially powerful for automated picking and segmentation thanks to machine learning tools. Its 3D visualisation is similar to IMOD in features.

Tomviz<sup>91</sup> is an open-source application focusing on tomogram reconstruction and visualisation, providing also a few segmentation and analysis tools.

When it comes specifically to particle picking and visualisation, a powerful tool recently developed is ArtiaX<sup>92</sup>, a ChimeraX<sup>86</sup> extension for cryo-ET. Thanks to ChimeraX’s beautiful ray-tracing renderer, ArtiaX is ideal to make figures for publications. Particle visualisation is also very convenient and allows even for visualising subtomogram averaging results (map isosurfaces) distributed on the tomograms thanks to a performant implementation with instanced rendering. ChimeraX also provides a Python API to control its visualisations, but doesn’t offer the same level of two-way and direct access to the visualised data as napari with its IPython console. ChimeraX’s features and ecosystem are also more focused on protein structure visualisation and analysis, whereas napari is first and foremost an imaging tool.

Another tool that blik already integrates with is CrYOLO<sup>30</sup>, which provides powerful machine-learning picking and segmentation routines. CrYOLO itself has recently adopted napari as its visualisation front-end.

A similar tool to the surface resampling widget in blik exists in Membranorama, which allows for visualising surfaces in a tomogram with the surrounding volume projected perpendicularly onto the surface, as well as extracting individual surface patches which can be “planarised” for easier inspection<sup>93,94</sup>. This tool is very useful for interactive visualisation and exploration of the projected surface *in situ*. blik, on the other hand, does not allow *in situ* projection, but instead focuses on generating a square-grid resampling which – differently from Membranorama – can be exported as an ordinary volume or reused immediately for further processing with

blik or other tools.

Given the popularity and fast growth of Cryo-ET, the field offers many other tools and software suites with features and goals compatible with blik. Some of them offer excellent opportunities of integration with the napari and blik ecosystem, such as TomoSegMemTV<sup>95</sup> and MemBrain<sup>96,97</sup>, which offer pixel-based and automated membrane segmentation (as opposed to the manual, surface-based annotation provided by blik) or pycurv<sup>98</sup> and surface-morphometrics<sup>99</sup>, which can compute meshes, measurements and statistics about pre-annotated membranes. With a collaborative and modular approach to software development, we strive for blik and teamtomo to become a starting point to enable such integrations in the future.

### 3.5 Conclusion

The work presented in this paper aims to reduce the friction of working with cryo-ET data, and to enable developers in the field to share, reuse and contribute as a community. The development of blik and its components is a stepping stone towards these goals.

Working within napari allows us to delegate (and share with other fields) many non-cryo-ET-specific components, while retaining interactivity and extensibility; napari is in rapid development, and direct contributions to the community-developed project are always welcome. Even where direct contributions are unfeasible, developers can take advantage of the plugin ecosystem (such as blik does) or simple scripting.

Now that blik's core features are established, we aim to reach out to other developers and cryo-ET software users and encourage reusing, adopting or contributing to the work here presented.

Future planned features for blik include:

- Exploit napari's nD visualisation, for example to easily view the progression of a particle refinement.

- Conclude the work on napari multicanvas, allowing multiple views on the data (e.g: picking in orthoviews).
- Implement instanced rendering in vispy to allow rendering full particle maps in the tomogram at high performance (like ArtiaX).
- Offer more geometric models for picking (e.g: spheres, 3D lattices).

## 3.6 Materials and methods

Not all the code contributions from this work live in the same place. Tools and implementations were split into standalone libraries or contributed to core napari when possible, in the interest of sharing and avoiding code duplication. Contributions from work in this paper are summarised below, and readers are encouraged to take advantage of all these open-source components for their own work.

Refer to the individual repositories for the most up-to-date and in-depth documentation.

### cryotypes and cryohub

The data structures and input/output (IO) functions used by blik are extracted into two usage-agnostic libraries: no assumptions from blik are carried over, which makes these libraries suitable for adoption by any Python software working with cryo-EM and cryo-ET data. Both libraries live in the github community project [teamtomo](#).

- [cryotypes](#): defines simple and extensible data structures for cryo-EM data types and metadata, and provides simple validation and checking functions to ensure a given object conforms to the specification.
- [cryohub](#): provides reading and writing functions for popular image formats and particle data, with both fine-grained controls and a higher level “magic” interface (`cryohub.open(<anything>)`). Data is read to and from cryotypes data structures, easily allowing for conversion between formats and integration in any third-party Python tool.

cryohub provides granular I/O functions such as `read_star` and `read_mrc`, which will all return objects following the cryotypes specification.

```
from cryohub.reading import read_star

poseset = read_star('/path/to/file.star')
```

A higher-level function called `read` adds some magic to the IO procedure, guessing file formats and returning a list of cryotypes.

```
from cryohub import read

data = read(
    '/path/to/file.star',
    '/path/to/directory/',
    lazy=False,
    name_regex=r'tomo_\d+'
)
```

See the help for each function for more info.

Similarly to the `read_*` functions, cryohub provides a series of `write_*` functions, and a magic higher-level `write` function.

```
from cryohub import write

write([poseset1, poseset2], 'particles.tbl')
```

## morphosamplers

Surface and filament picking and particle generation code are not specific to cryo-ET. They were developed as part of a field-agnostic library called [morphosamplers](#), which collects several tools for sampling image data with morphological objects. As part of this work, models for spline filaments and spline-based surfaces were developed, with their relative tools for particle generation and image resampling.

## napari plugins

Some of the napari-specific functionalities developed for blik were also not cryo-EM-specific, and could instead be useful for many other applications in the napari ecosystem. These were extracted into their own napari plugins, which can be installed separately.

- `napari-label-interpolator`: a simple utility to interpolate n-dimensional labels along a specified dimension. Its main use in the context of cryo-ET is to reduce the manual annotation necessary to fully segment a volume. However, such functionality can also be used for example to track objects such as cells over a 2D (or 3D) time series.
- `napari-properties-plotter`: several napari layers such as Points and Labels can hold features data for each of their items. This plugin allows to display any of such feature combinations in an interactive plot widget; users can then select a subset of the data items based on a selected section of the plot.

## napari and vispy

Where possible, napari-specific code was contributed upstream to the napari core repository (or vispy for rendering-related code). Much of this work was distributed and collaborative in nature; here are listed some highlights that were crucial for the proper development of blik and to which significant contributions were made as part of this work.

- Improvements to quality, performance and interactivity of 3D rendering for volumes and labels, including work such as proper depth buffer and blending usage, arbitrary plane slicing and clipping, additional 2D and 3D interpolation modes.
- Visualisation of points as spheres for more intuitive 3D visualisation.
- Improvements to surface mesh visualisation (shading).
- Projection of n-dimensional bounding box instead of simple point-slicing.

## blik

Any remaining functionality specific to napari and cryo-EM was implemented directly in blik by often wrapping the aforementioned tools.

Manual particle picking makes use of the simple point picker in napari, while automatically adding orientations and metadata needed for writing to file.

Surface and filament picking are mainly wrappers around morphosamplers, but add a GUI for setting parameters and use napari layers for picking. The manual picks can then be used to generate visualisations such as filaments and meshes, for particle picking for subtomogram averaging, and for volume resampling.

A few image filtering and processing tools are also provided with blik for ease of visualisation, such as bandpass filtering and a power spectrum generator.

## 3.7 Acknowledgements

We are particularly grateful to Alister Burt for stimulating discussions, suggestions, and initial guidance.

## 3.8 Data availability

The current version of blik at time of publication is available permanently at Zenodo (<https://doi.org/10.5281/zenodo.10894490>). The source code is maintained at <https://github.com/brisvag/blik>.

## 3.9 Funding

This project received funding from GRAL, the Grenoble Alliance for Integrated Structural and Cell Biology, a programme of the Chemistry Biology Health Graduate School of Université Grenoble Alpes (ANR-17-EURE-0003),

and from the Agence Nationale de la Recherche (grant ANR DecRisp ANR-19-CE11-0017-01 to I.G.). The funders had no role in study design, data collection and analysis, decision to publish, or preparation of the manuscript.

## 3.10 Addendum

Since this paper was finalized, blik continued to receive regular updates and new features, and has increasingly been used in production by a few colleagues.

An exciting addition is the ability to now use membrane segmentation — coming from any other software — to seed the surface picking more precisely and without the need for manual intervention. With the increasingly better surface segmentation tools available to the community, this feature enables a faster and more robust way to resample surfaces or distribute particles on membranes. This feature was the result of a productive hackathon in collaboration with several core developers of napari and members of Ben Engel’s group at the University of Basel, which also resulted in another tool called Surforama<sup>100</sup>.

Other ways to pick particles are also being added, such as a sphere-based picking for particles on vesicles, and more refined controls for setting the 3D orientation of picked particles.

blik is now being regularly used by our team and others to visualise and annotate tomograms, and pick particles for STA, and was used extensively for our work on *D. radiodurans* ([Chapter 4: \*D. radiodurans\*: cell division and septation](#)).

# Chapter 4

## *D. radiodurans*: cell division and septation

This (unpublished) manuscript brings together conventional and super-resolution fluorescence imaging experiments — performed by F. Lacroix and JP Kleman from the GenOM team — and cryo-ET data from FIB-milled lamellae — acquired by my supervisor I. Gutsche — of *Deinococcus radiodurans*, to characterize the complex composition of this bacterium's cell wall and its unusual mode of septation.

My contribution to this work is tightly coupled to the previous chapter ([Chapter 3: blik: a cryo-ET visualisation and analysis tool](#)): the membrane annotation tool presented therein was developed as a way to systematically analyse the membrane profiles of *D. radiodurans* — as well as uniformly distribute particles for the later work on FtsZ ([Section 4.3: FtsZ is present at the tips of septa](#) and [Section 5.2: FtsZ function and structure](#)). The cryo-ET data processing was also performed by me, through which I established and refined our group's tomography pipeline, consolidated by the batch processing tool waretomo I developed for this work<sup>101</sup> ([Section 5.3: waretomo](#)).

## Contents

Contents .....	66
4.1 Abstract .....	67
4.2 Introduction .....	68
4.3 Results .....	71
Cell wall composition and maturation .....	71
Structure of septal tips .....	76
Septation through a “sliding doors” mechanism .....	79
PG synthesis machineries .....	83
FtsZ is present at the tips of septa .....	86
4.4 Discussion .....	88
4.5 Materials and methods .....	94
Bacterial cultures .....	94
Cell labelling for confocal and SMLM microscopy .....	95
Confocal data acquisition and processing .....	97
SMLM (PAINT/dSTORM) data acquisition and processing .....	97
Sample preparation for Cryo-ET .....	98
Cryo-ET data acquisition .....	99
Cryo-ET data processing .....	100
4.6 Acknowledgements .....	100
4.7 Funding .....	101
4.8 Supplemental figures .....	102

## Combining live cell fluorescence imaging with *in situ* cryo electron tomography sheds light on the septation process in *Deinococcus radiodurans*

Gaifas L.<sup>1†</sup>, Kleman J.P.<sup>1†</sup>, Lacroix F.<sup>1†</sup>, Schexnaydre E.<sup>2</sup>, Trouvé J.<sup>1</sup>,  
Morlot C.<sup>1</sup>, Sandblad L.<sup>2</sup>, Gutsche I.<sup>1,2\*</sup> & Timmins J.<sup>1\*</sup>

<sup>1</sup> Univ. Grenoble Alpes, CEA, CNRS, IBS, F-38000 Grenoble, France.

<sup>2</sup> Department of Chemistry, Umeå University, Umeå, Sweden.

† Joint Authors.

\* Corresponding authors.

### 4.1 Abstract

Cell division is a fundamental biological process that allows a single mother cell to produce two daughter cells. In bacteria, cell division involves two major steps: septation corresponding to the growth of a new dividing cell wall, followed by separation of the two daughter cells. The mode of cell division is largely dictated by the composition of the cell wall and the shape of the bacteria. The radiation-resistant bacterium, *Deinococcus radiodurans*, is protected by a thick and unusual cell envelope and has been reported to divide using a distinctive mode of septation in which the two septa grow across the cell from opposite sides of the cell with a flat leading edge before meeting ad fusing at mid-cell. In the present study, we have combined conventional and super-resolution fluorescence microscopy of live bacteria with *in situ* cryogenic electron tomography of bacterial lamellae to investigate the septation process in *D. radiodurans*. This work provides important insight into (i) the complex cell wall composition of this bacterium, (ii) the “sliding doors” septation process and (iii) the molecular mechanisms underlying coordinated septal growth and closure.

## 4.2 Introduction

Bacterial cell division occurs through binary fission<sup>102</sup> and involves two major steps: (i) inward growth of a new dividing cell wall, known as septum, typically down the middle of the cell and (ii) separation of the two daughter cells through the action of cell wall hydrolases. The new septum can result from either constriction, septation or a combination of both processes<sup>103,104</sup>. In most Gram-negative bacteria, including *Escherichia coli*, cell division is achieved by progressive constriction of the bacterial cell wall at mid-cell until fusion of cell envelope structures allows the separation of daughter cells. In contrast, in Gram-positive bacteria, such as *Staphylococcus aureus* or *Bacillus subtilis*, cell division results from progressive synthesis of a new septal cross-wall at mid-cell that advances centripetally from the outer cell wall like a closing iris until full closure of the septal disk<sup>105,106</sup>. Cryo-electron micrographs of various dividing Gram-positive bacteria have revealed that this septum is actually composed of two adjacent cross-walls separated by a low density region<sup>107–111</sup>. In this mode of division, known as septation, the diameter of the mother cell is unaffected. Some bacteria, such as gonococci and *Escherichia coli*, have also been observed to divide using a combination of constriction and septation<sup>104,112</sup>. In the constriction mode, daughter cell separation occurs at the same time as the division process, while in the case of septation, splitting of the daughter cells only occurs once a complete, new septum has been synthesized. This splitting step can be slow and gradual as in *B. subtilis*<sup>113</sup>, or instead very fast through a “popping” mechanism as in *S. aureus* and actinobacteria<sup>114–116</sup>.

The mode of cell division, constriction versus septation, is to a large extent dictated by the composition of the cell wall. Monoderm (Gram-positive) bacteria that are missing a second OM layer usually possess a thick and multilayered peptidoglycan (PG), while diderm (Gram-negative) bacteria have a thin predominantly single-layered PG<sup>117</sup>. PG is an essential constituent of bacterial cell walls that defines cell shape and protects the cell from turgor pressure<sup>117</sup>. A thick PG layer, as found in many Gram-positive bacteria, is not compatible with cell constriction that requires a

major remodeling and distortion of the cell wall at the site of division<sup>118</sup>. Cell shape also influences the mode of cell division. Indeed, unlike rod-shaped bacteria, a large majority of cocci have been found to divide by septation and not by constriction<sup>119,120</sup>, suggesting that constriction may be facilitated by the elongated shape of bacilli.

These distinct modes of cell division rely on both common and species-specific molecular mechanisms and division factors. In most bacteria, cell division begins with the assembly of the highly conserved FtsZ protein into a Z-ring on the cytoplasmic side of the IM of bacterial cell walls at mid-cell. This Z-ring then acts as a scaffold for the recruitment of several membrane-associated and periplasmic division factors (including the penicillin-binding proteins or PBPs) that together form the divisome<sup>120</sup>. After the divisome has assembled, the ring constricts as the septum progresses, and peptidoglycan is synthesized at the leading edge of the septum, dividing the mother cell into two equally sized cells. In rod-shaped bacteria, two distinct PG synthesis machineries are responsible for peripheral cell wall synthesis and septal cross-wall synthesis<sup>121</sup>. The former is part of the elongasome<sup>121</sup>, a complex responsible for the elongated, rod-shape of these bacteria and is organized by the actin-like MreB protein<sup>122</sup>, while the latter is part of the divisome<sup>123,124</sup>. In cocci and ovococci, which are missing the MreB protein and the elongasome, recent studies making use of single-molecule localization microscopy (SMLM) and 3D structural illumination microscopy (3D-SIM), two super-resolution techniques that provide enhanced spatial resolution, suggest that two distinct machineries involving partially overlapping factors are likely also at play for peripheral and septal cell wall synthesis respectively, both of which would localize at midcell<sup>120,125–128</sup>.

The septation process in the spherical bacterium, *Deinococcus radiodurans*, is unlike that of other cocci. Based on electron micrographs of freeze-cleaved *D. radiodurans* cells, Murray et al.<sup>111</sup> reported that division is not initiated symmetrically from around the whole circumference of the cell at once, but is instead achieved by fusion of two septa growing across the cell from opposite sides of the cell with a flat leading edge to close the slit<sup>111</sup>. This observation was more recently supported by 3D confocal

microscopy imaging of Nile Red labelled *D. radiodurans* cell membranes<sup>129</sup>.

Exposure of *D. radiodurans* to high doses of radiation causes significant damage to the genome and immediate cell cycle arrest<sup>130</sup> suggesting that cell growth and division in this organism are tightly regulated. *D. radiodurans* cells divide in two alternative perpendicular planes<sup>111,131</sup> and their cell cycle can be classified into 6 phases (**Figure 4.1A**). Starting from an elliptical and largely symmetric diad in Phase 1, the cells grow and septal closure progresses until tetrads are formed in Phase 6 which, in exponential phase, are very short lived and rapidly split into two diads to initiate a new cell cycle<sup>129</sup>. As a result, in this organism, the two major steps of cell division, i.e. (i) septal growth and (ii) splitting of the daughter cells, actually occur in separate cell cycles, with septal closure taking place in cycle  $n$  and splitting of the cells in cycle  $n+1$  (**Figure 4.1A**). This temporal separation makes *D. radiodurans* particularly well suited as a model to study septation.

In the present study, we have combined conventional and superresolution fluorescence microscopy of live cells with *in situ* cryogenic electron tomography (cryo-ET) of bacterial lamellae obtained by cryo-focused ion beam (FIB) milling, to image dividing *D. radiodurans* cells. This work unveils the different layers of the cell wall at various stages of the division process. We unambiguously demonstrate that septation of *D. radiodurans* proceeds by a “sliding doors” mechanism in which the cross-wall grows through PG synthesis at the initially flat and progressively curved leading edge of the septa until membrane fusion occurs, first at the extremities of the septa and then all the way across the diameter of the cell in a zip-like mechanism. Using a fluorescent D-Ala probe, we show that PG synthesis in *D. radiodurans* occurs in both septal regions and in the outer cell periphery, and involves two distinct machineries for peripheral and septal cell wall synthesis, with the latter being fully inhibited by ampicillin treatment. To our surprise, membranous protrusions were frequently observed in our tomograms at the tips of the closing septa at early stages of the septation process. We propose that these remarkable structures may constitute a preformed dual membrane layer for the future septum and that PG synthesis in between

these two lipid bilayers progressively fills, thickens and rigidifies the structure of the growing septum. Finally, this rigidification step appears to be guided by the assembly of FtsZ filaments at the tips of the growing septa to coordinate PG synthesis and the septation process.

## 4.3 Results

### Composition, structure and maturation of *D. radiodurans* cell wall

*D. radiodurans* is known to possess an unusual cell wall that stains Gram-positive, but yet is composed of both an inner and an outer plasma membrane interspersed by a thick multilayered region. We have combined super-resolution fluorescence microscopy of live cells with cryo-ET on cryo-FIB-milled *D. radiodurans* lamellae to decipher the structure and composition of this cell wall depending on its location (**Figure 4.1B-C**). Three distinct compositions can be observed in our cryo-ET data (**Figure 4.1B**). The outer, fully matured cell wall is the thickest. The new growing septum is on the contrary the thinnest, and the central septum located between the two cells composing a typical *D. radiodurans* diad, corresponds to an intermediate stage of cell wall maturation before the splitting of the daughter cells. It should be noted that the new septa and the central cell wall both correspond to a double cell wall with a mirror symmetry, as can be seen in both the cryo-ET and super-resolved images (**Figure 4.1B-C**).

The outer cell wall bears two lipid bilayers that can be seen as dark lines in the cryo-ET data (**Figure 4.1B**) and could be distinguished on a few occasions in our super-resolved PAINT images of Nile Red stained *D. radiodurans* (**Figure 4.1C, right panel**). The distance between the inner (IM) and outer (OM) cell membranes was in good agreement between the two techniques and was found to be around 95 nm (**Figure 4.1B-C**). A more in-depth analysis of the cell wall layer composition was facilitated by calculation of straightened cell wall projections of the cryo-ET images using a recently developed tool, blik<sup>72</sup>. Density profiles of the outer cell

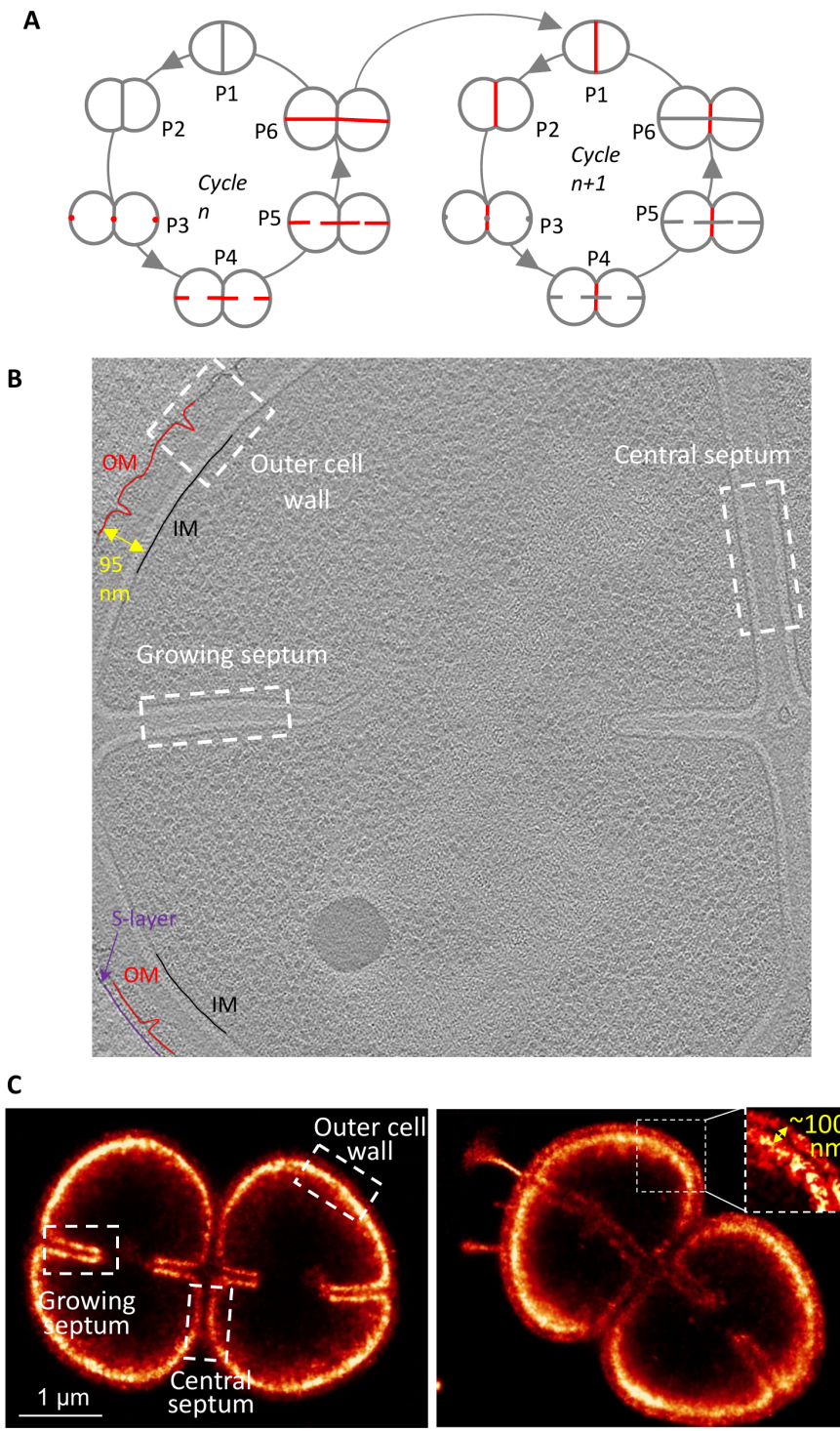


**FIGURE 4.1:** Structures of exponentially growing *D. radiodurans* cell walls during the process of cell division. (caption on the next page)

**FIGURE 4.1:** (A) Schematic diagram of exponentially growing and dividing *D. radiodurans*. Transition from a diad (two-cell unit) to a tetrad (four-cell unit) involves 6 distinct phases (P1-P6). The septation process occurs during phases P3 to P6 of cycle  $n$  (left, red), while the splitting of this newly synthesized cell wall only occurs in the following cell cycle, cycle  $n+1$  (right, red). (B) Central slice of a typical cryo-electron tomogram of an actively dividing wild-type *D. radiodurans* diad. Three different types of cell wall can be seen in this image: (i) the multilayered outer cell wall composed notably of both an inner (IM) and an outer (OM) membrane highlighted respectively in black and red and a discontinuous S.layer (purple), (ii) the central septum dividing the two cells composing the diad unit, and (iii) the new growing septa originating from opposite sides of the cell. The mean distance between the two membranes in the outer cell envelope was determined to be 95 nm. The light grey density in the center of the cell corresponds to the nucleoid, the darker spherical form is a stress granule and the small dark densities distributed throughout the cytoplasm (and excluded from the nucleoid) are ribosomes. Scale bar: 100 nm. (C) Two examples of super-resolved PAINT images of Nile Red stained wild-type *D. radiodurans* diads in the process of dividing. Nile Red specifically stains the plasma membrane. As in (A), three distinct regions of cell wall can be distinguished. On a few occasions, the two lipid bilayers of the outer cell envelope could be resolved (as in the right image). The mean distance between these two layers was determined to be 100 nm in good agreement with the 95 nm measured on the tomograms. Scale bar: 1  $\mu$ m.

wall revealed that this region is composed of 6 distinct layers: (i) the IM, (ii) a low-density periplasmic space, (iii) a high-density PG layer, (iv) an intermediate layer previously described as the SlpA layer<sup>132</sup>, (v) the OM and (vi) a discontinuous S-layer on the outer surface of the bacteria (**Figure 4.2A**). A distinctive white line was observed separating the PG layer from the SlpA layer and V-shaped invaginations of the OM were seen regularly along this outer cell wall. Measurements made on numerous tomograms allowed us to determine the mean thickness of each of these 6 layers. When present, the S-layer was typically located at 18 nm above the OM. The SlpA layer was found to be  $\sim$ 35 nm in thickness in good agreement with the estimated dimensions of the SlpA complex that stretches across this layer<sup>132</sup>. The PG layer was found to be  $\sim$ 44 nm in thickness and located approximately 15 nm above the IM, with a low-density region nestled in between these two essential layers. Interestingly, these measurements revealed that the IM bilayer was significantly thicker than the OM (5.8 nm vs 5.0 nm; **Figure 4.2B**), suggesting distinct lipid compositions.

A similar procedure was used to analyse the composition of the growing septa and the central cell wall region. The outer layers of the external

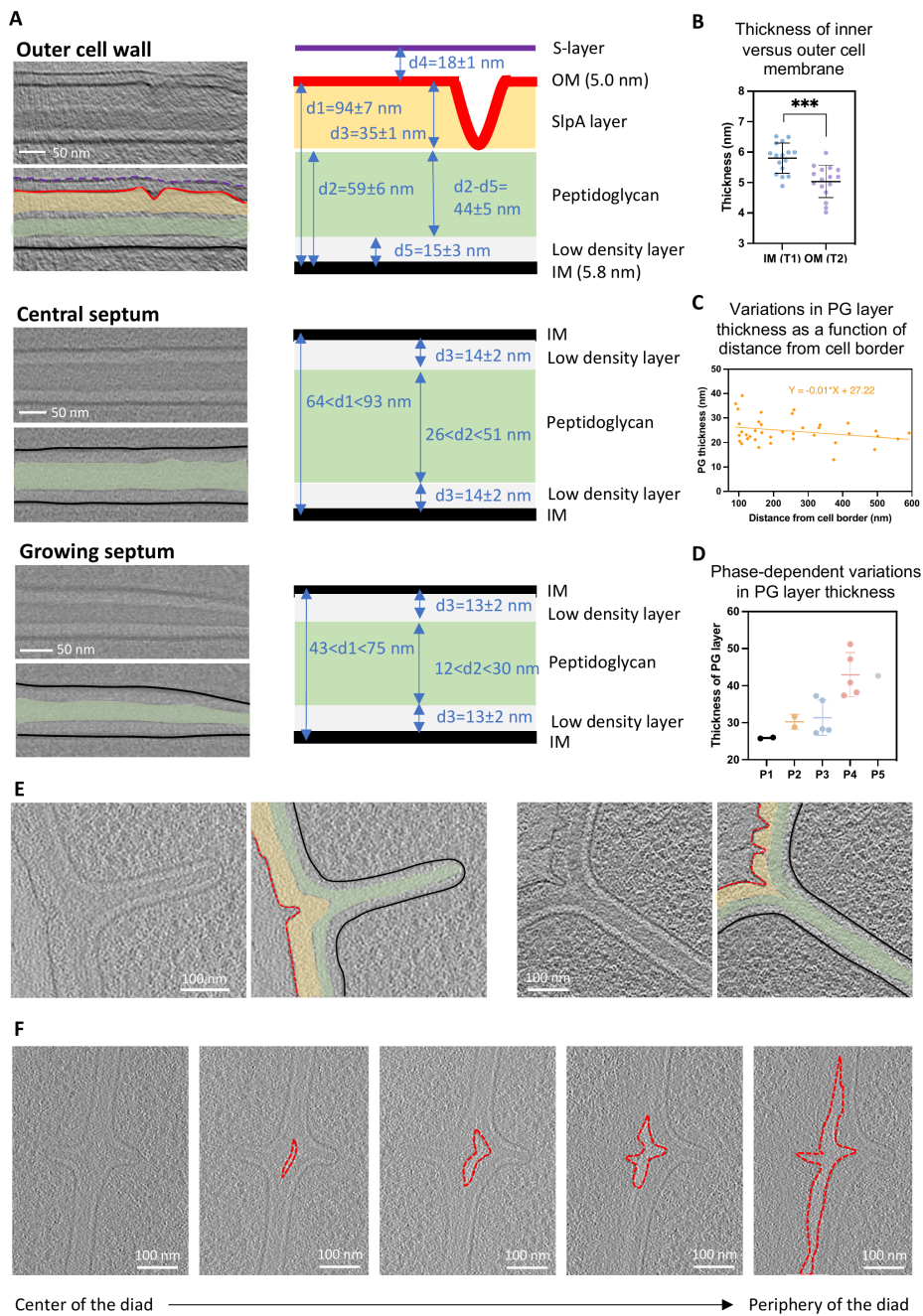


**FIGURE 4.2:** In-depth analysis of the structure and composition of the cell wall of *D. radiodurans*. (caption on the next page)

**FIGURE 4.2:** (A) Straightened regions of the outer (Top), central (middle) and growing septum (bottom) cell walls were used to measure the thickness of the various layers composing these three types of cell wall shown schematically to the right of the images (**Suppl. Figure 4.15**) for more details). Left: Top panels show a straightened region and lower panels show the same region with segmentations of the various layers. The IM is highlighted in black, the OM in red, the S-layer in purple, the SlpA layer in yellow, the peptidoglycan in green and the low-density periplasmic space in light grey. Scale bars: 50 nm. (B) Mean and standard deviation of the thickness of the inner (IM) and outer (OM) membranes within the outer cell envelope. N=16. Statistical test: Welch's t-test. \*\*\* p=0.0002. (C) Plot illustrating the variation in PG thickness as a function of the distance from the root of the growing septa. The PG layer was thinner at the leading edge than at the base of the growing septa. (D) Plot illustrating the phase-dependent thickness of the peptidoglycan (PG) layer in the central septum (d2 in **Suppl. Figure 4.15**). Bars correspond to mean and standard deviation per phase (N<6 for each phase). Individual points correspond to the mean thickness measured on each tomogram. (E) Two illustrations of junctions between the outer cell envelope and the growing septa. Left panels show 2D slices of a tomogram and right panels show the same regions with segmentations of the various layers (colors as in A). Scale bar: 100 nm. (F) 2D slices extracted from a given tomogram at different z values illustrating the progressive splitting of daughter cells that starts at the cell periphery (right) and then progresses inwards towards the center of the diad (left). The progressive synthesis of the outer lipid bilayer is shown in red. Scale bar: 100 nm.

cell wall (S-layer, OM and SlpA layer) were missing in these regions (**Figure 4.2A**), and instead septa were composed of a single central continuous PG layer with the IM and the low-density periplasmic space on either side. These three layers were continuous with those of the outer cell envelope. While the IM bilayer and low-density periplasmic space showed similar thicknesses in these two locations, the PG layer displayed significant variations, ranging from 26 nm to 51 nm in the central cell wall and as low as 12 nm in the growing septa. In both the growing septa and the central cell wall, the PG layer was typically thicker at the cell periphery than at the leading edge of the septum (**Figure 4.2C**) or the centre of the diad. Moreover, in the central cell wall, the mean thickness of the PG layer was also found to vary substantially as a function of the phase of the cell cycle (**Figure 4.2D**), suggesting a progressive thickening of this layer until reaching its final size prior to the splitting of the diad.

At the junction between the outer cell wall and the root of the growing septum (**Figure 4.2E** and **Suppl. Figure 4.9** for more examples), we observed that the PG and low-density periplasmic layers followed the IM,

while the outer layers (SlpA layer and OM) were restricted to the outer cell wall. V-shaped invaginations in the OM were often observed at these junctions and were found to extend inwards during the splitting of the two daughter cells during the subsequent cell cycle. As shown in **Figure 4.2F**, cell splitting is a progressive process, most likely initiated from the cell periphery and moving inwards from both the top and the bottom of the cell towards the center of the diad forming bubble-like membrane structures (**Suppl. Figure 4.8B** for more examples). Splitting occurs concomitantly with the addition of the SlpA layer and finally the OM to the central septum cell wall (**Figure 4.2E-F**).

### Structure of septal tips

A close inspection of the tomograms revealed that the tips of the growing septa exhibited particular structures. A majority of septa (40 of the 64 septa visible in our tomograms) were slightly tapered at their tips and the low-density periplasmic space was significantly thinner in these regions bringing the PG layer very close to (in some cases even touching) the IM (**Figure 4.3A**). Strikingly, in nearly 40% of the observed septa, membrane protrusions, reported in earlier studies as mesosomes<sup>131,133</sup>, were observed at the tips of growing septa (**Figure 4.3B-C** and **Suppl. Figure 4.9** for more examples). These structures, mostly observed in cells in early stages of the septation process bearing short septa, appear to be composed solely of the low-density layer delimited on either side by the IM bilayer, and adopt either outstretched tube-like structures or more circular loop-like arrangements. In all cases, they appear to be very flexible, probably as a result of the absence of a PG layer to rigidify the protrusion. This intrinsic flexibility may explain why the tips of the growing septa were often not observed in the super-resolved images of Nile Red-labelled *D. radiodurans* cells (**Figure 4.3C**, left panel). Instead, in these images, open ends were observed at the leading edge of the growing septa. This suggests that either the Nile Red dye poorly labelled these highly curved membrane bilayers (likely exhibiting reduced membrane fluidity that is known to affect Nile

Red staining<sup>134</sup>) or that the tips were very mobile and not captured in live imaging experiments; both of these phenomena may also be at play. On a few occasions, we did nonetheless observe poorly defined Nile Red labelling at the tips of growing septa that may correspond to such flexible membrane protrusions (**Figure 4.3C**, right panel).

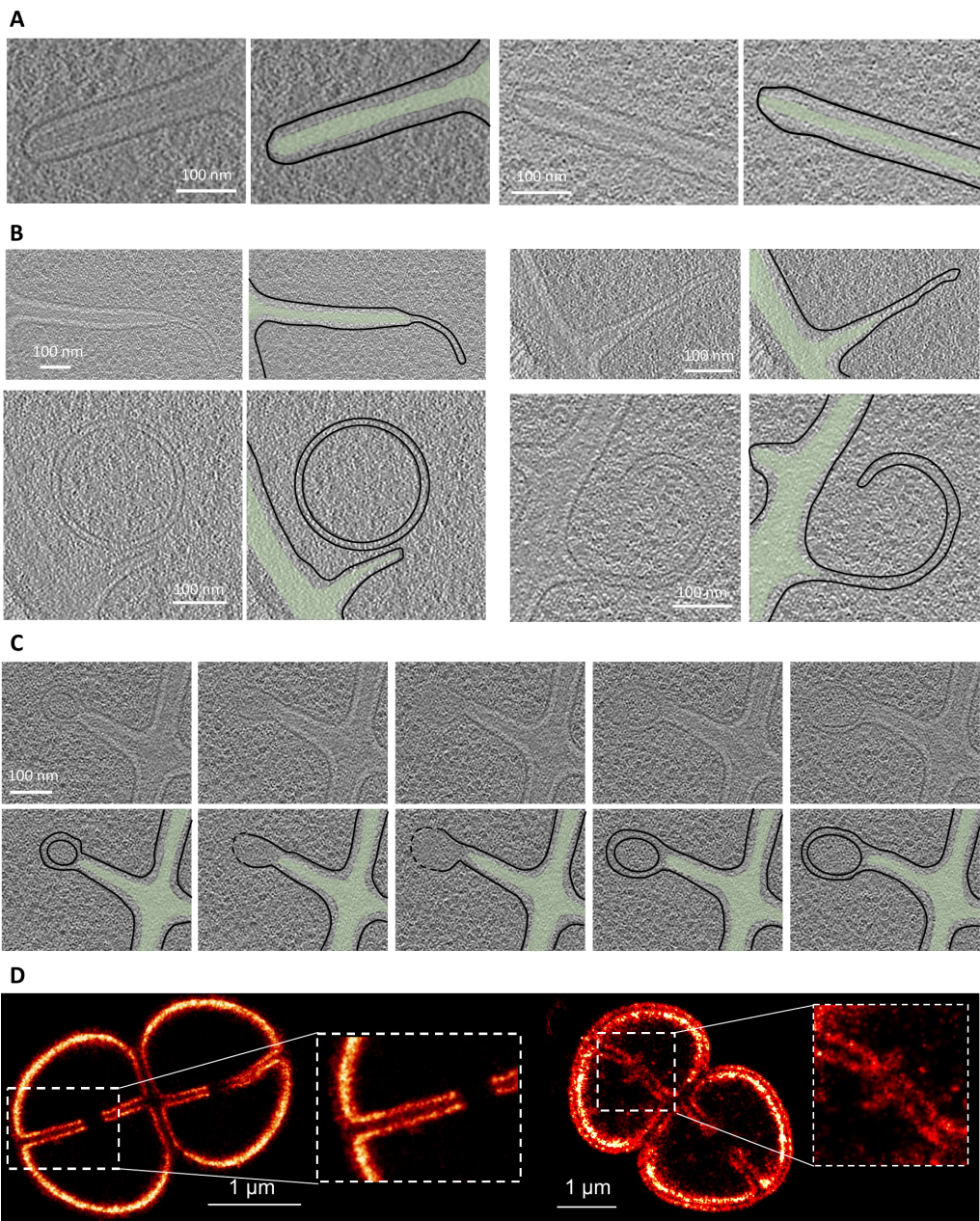


FIGURE 4.3: Close-up view of the septal tips. (caption on the next page)

**FIGURE 4.3:** (A-B) Examples of typical septa tip morphologies: (A) tapered leading edge with a well-defined and rigid PG layer (green) stretching almost to the IM (black) and (B) tubular (top) and curved (bottom) membrane protrusions extending the growing septa. Left panels show 2D slices of a tomogram and right panels show the same regions with segmentations of the various layers (colors as in Fig. 2A). (C) 2D slices extracted from a given tomogram at different z values illustrating the change in size and shape of these membrane protrusions as a function of the position in the tomogram. Top panels show 2D slices and lower panels show the same regions with segmentations of the PG and IM layers (colors as in Fig. 2A). (A-C) Scale bar: 100 nm. (D) Close-up views of the leading edges of growing septa captured by super-resolution PAINT microscopy of Nile Red stained wild-type *D. radiodurans* diads in the process of dividing. Left image: septal tips appear to be open-ended with no fluorescence signal for the highly curved membrane located at the leading edge of these closing septa. Right image: blurry septal tips are visible pointing in opposite directions. These structures may correspond to the membrane protrusions observed in the tomograms (B, C). Scale bar: 1  $\mu$ m.

## Septation through a “sliding doors” mechanism

Using timelapse 3D video confocal microscopy of Nile Red stained *D. radiodurans* bacteria immobilized in various orientations on agarose pads ([Suppl. Figure 4.10B](#)), we followed the division process in live cells. Septation was found to proceed in several steps. First, two septa originating from opposite sides of the cell grow inwards with a flat leading edge creating a central gap stretching from the top to the bottom of the cell ([Figure 4.4](#)). As the septa grow, the leading edge progressively becomes more curved. Finally, when the two septa come close to each other, fusion starts first at the top and bottom of the cell forming a cat’s eye structure and then rapidly proceeds through a zipping mechanism from the cell periphery to the cell center. 3D super-resolved (PAINT) images of Nile Red labelled *D. radiodurans* cells confirmed these observations, allowing to capture snapshots of dividing cells exhibiting septa with flat or slightly curved leading edges embracing a central gap that stretches all across the cell ([Figure 4.4A](#)). Kymographs of individual septation events were extracted from the live cell confocal acquisitions to probe the kinetics of septal closure ([Figure 4.4B](#)). These revealed that septation is a linear process in which the external and internal septa grow respectively at rates of  $7.3 \pm 0.5$  nm. $\text{min}^{-1}$  and  $4.1 \pm 0.7$  nm. $\text{min}^{-1}$  until full closure. Interestingly, the external septum not only grows at a faster rate than the internal septum, it also starts growing ahead

of the internal septum, as can be seen from the asymmetric V-shaped structure of the kymographs (**Figure 4.4B**). This is also visible in several of the tomograms, capturing bacteria at various stages of the division process (**Figure 4.4C-D**). This may be explained by the fact that the external septum needs to grow further than the internal septum to reach the site of fusion located at mid-cell and has to compensate for the expansion of the cells that is occurring simultaneously. The flat or slightly curved leading edge of the growing septa were also observed in the tomograms (**Figure 4.4C**).

In addition to staining the cell membrane, we also labelled the PG layer of *D. radiodurans* cell walls by incorporating modified azido-D-alanine (aDA) into the cell wall that was subsequently labelled by copper free click chemistry with fluorescent probes suitable for either confocal or dSTORM microscopy<sup>125,135</sup> (**Suppl. Figure 4.11**). The PG labelling pattern (**Figure 4.4E** and **Suppl. Figure 4.12**) was very similar to that of Nile Red labelled cells, with an efficient incorporation occurring in all regions of the cell wall (septal, central and outer cell walls) as was observed previously using fluorescently labelled D-alanine<sup>129</sup>. The main difference was that the PG labelling was more prominent at the leading edge of the growing septa than elsewhere, suggesting this likely corresponds to the major site of active PG synthesis in these dividing cells (**Figure 4.4E-F**). This is particularly visible at late stages of the cell cycle, either just before (Phase 5) or just after cytokinesis (Phase 6), where an intense band of labelled PG can be seen at the site of fusion where the two opposing septa meet (**Suppl. Figure 4.12C**). In agreement with these observations, pulse-chase experiments in which bacteria were returned to the incubator for 45 minutes (chase) after incorporation of the modified aDA (pulse) into their cell walls, revealed that septa having incorporated aDA labelling at their tips during the pulse period, were progressively extended further by unlabelled PG, indicating that new PG is added to the existing layer in an inwards direction until the opposing septa are close enough to fuse (**Figure 4.4F** and **Suppl. Figure 4.13**).

Close examination of the tomograms also revealed that the position and shape of the growing septa changed as a function of their length

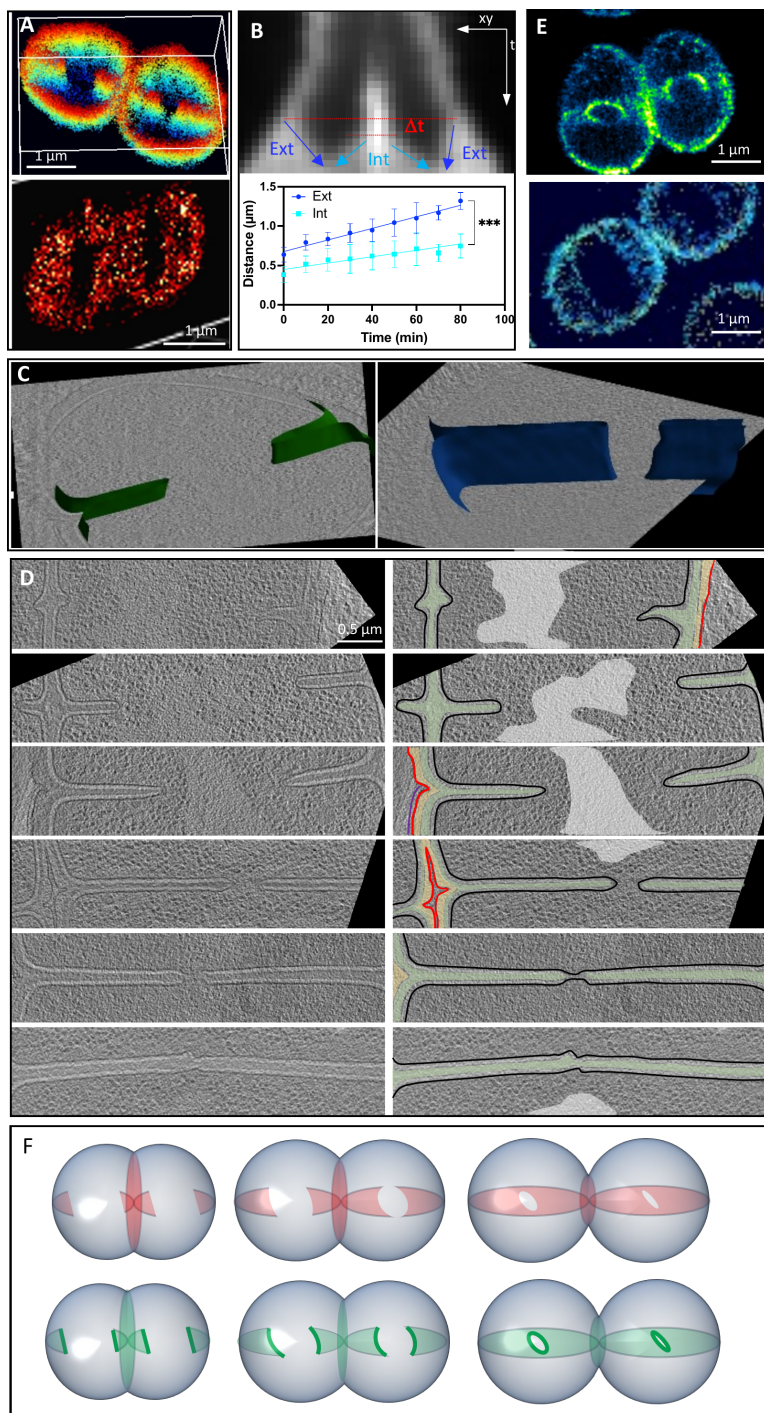


**FIGURE 4.4:** Septation through a “sliding doors” mechanism. (caption on the next page)

**FIGURE 4.4:** (A) 3D super-resolved PAINT image of a Nile Red stained wild-type *D. radiodurans* diads in the process of dividing. Top panel: the 3D volume was obtained by combining 2 stacks of images collected at different focus heights. The flat leading edge is very clear in the left cell while the right cell, which is more advanced in its division process, illustrates the formation of a cat's eye structure stretching across the cell as the opposing septa first meet and fuse at the top and bottom of the cells. This structure is also visible in the lower panel, corresponding to a side view of a labelled cell. Scale bar: 1  $\mu\text{m}$ . (B) Kymograph analysis of the septation process in Nile Red stained *D. radiodurans*. Top panel: example of a typical kymograph obtained for a dividing diad. The coordinates of the borders of the fluorescent signal were used to determine the length of the external (dark blue) and internal (light blue) septa as a function of time. The lag time ( $D_t$ ) between the start of septal growth for the external septa versus the internal septa was also measured. Lower panel: Plot illustrating the linear growth of the external (dark blue) and internal (light blue) septa as a function of time. The external septa were found to grow at a significantly higher rate than the internal septa. \*\*\* (p-value: 0.0004). (C) Examples of segmented septa in two tomograms illustrating the flat edge of the growing septa (left panel, green) that progressively becomes more curved (right panel, blue) as the division process advances. (D) 2D slices extracted from various tomograms illustrating different stages of the septation process in *D. radiodurans*. Left panels show 2D slices of a tomogram and right panels show the same regions with segmentations of the various layers (colors as in Fig. 2A). The light grey annotation in the panels on the right corresponds to the nucleoid. Scale bar: 0.5  $\mu\text{m}$ . (E) 3D super-resolved dSTORM image of PG-labelled (through incorporation of azido-D-Alanine) wild-type *D. radiodurans* diads in the process of dividing. Top panel: PG synthesis occurs both in the septa and in the outer cell wall with a strong PG synthesis activity detected at the leading edge of the growing septa (intense ring and arch). Lower panel: side view of a PG-labelled *D. radiodurans* diad illustrating the incorporation throughout the septal region and the formation of the cat's eye structure similar to that observed in Nile Red stained cells (A). Scale bar: 1  $\mu\text{m}$ . (F) Schematic model of the “sliding doors” mechanism of septation in *D. radiodurans*. The top panels illustrate the Nile Red labelled membrane growth (red), while the lower panels show the closely-related growth of the PG layer and the strong PG synthesis activity at the leading edge of the septa.

(Figure 4.4D). At early stages of the septation process, short septa were not always precisely facing each other and their tips were often bent and bearing membrane protrusions (Figure 4.3B-C and Figure 4.4D), while at later stages, septa were remarkably straight and fully aligned to ensure fusion of the septa originating from opposite sides of the cell (Figure 4.4D). The presence of a PG layer in the growing septa appears to be a pre-requisite for the formation of these straight and well-aligned septa, indicating that the synthesis of the PG layer may provide the necessary rigidity to the growing cell walls for the final closure. This final fusion step was captured in two of the tomograms and was found to proceed first through fusion of

the IM bilayers and subsequently through synthesis of PG to fill the gap and “glue” the two septa together (**Figure 4.4E**). Taken together, these data allow us to propose a model of septation through the “sliding doors” mechanism, which is illustrated schematically in **Figure 4.4F**.

### PG synthesis in the outer cell wall and in the septa are performed by distinct machineries

To better understand the molecular mechanisms underlying this unusual mode of septation, we treated *D. radiodurans* cultures with the  $\beta$ -lactam antibiotic, ampicillin, and compared the growth of untreated and treated Nile Red labelled cells by 3D confocal timelapse microscopy for a three-hour period (**Figure 4.5A**). Ampicillin is known to bind to the active sites of certain PBPs, thereby inhibiting their enzymatic cell wall synthesis function<sup>136</sup>. To our surprise, septation but not cell growth was arrested by ampicillin treatment (**Figure 4.5A-C**). Indeed, the growth of the outer cell perimeter was unaffected by this treatment during this three-hour period, while growth of both the internal and external septa were rapidly arrested (**Figure 4.5B-C**). After 1 hour, the septa even started to shorten, suggesting they may be undergoing disassembly and degradation (**Figure 4.5C**). As a result of this change in the balance between cell growth and septation, cells progressively became distorted (more elongated with a slight bulge at sites of division) as evidenced by the substantially increased diameter (d) to perimeter (p) ratio after three hours of treatment with ampicillin (**Figure 4.5D-E**). The specific inhibition of septal growth by ampicillin suggests that the PBPs responsible for PG synthesis and maturation in the septa are distinct from those involved in outer cell wall growth (**Figure 4.5F**).

Next, we repeated the aDA incorporation experiment on cells pre-grown for either 1 or 2h in the presence of ampicillin before the labelling (**Suppl. Figure 4.14**). In these conditions, aDA was still readily incorporated into the outer cell wall, as expected based on our timelapse experiments. In contrast, no labelling was seen in the septal regions, except at sites of septation initiation at the junction between the outer cell wall and the

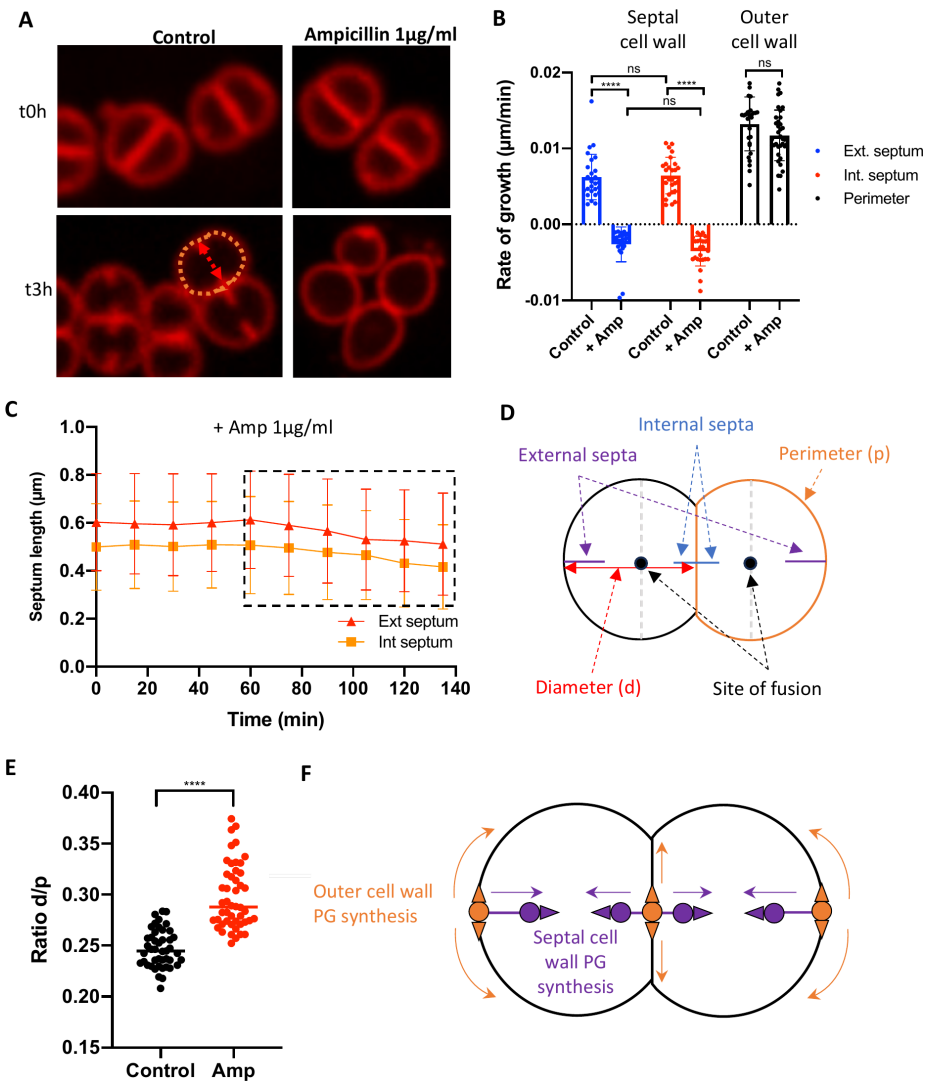


**FIGURE 4.5:** Distinct PG synthesis machineries are involved in septal and outer cell wall growth. (caption on the next page)

**FIGURE 4.5:** (A) Examples of untreated (left) and ampicillin-treated (right) Nile Red stained *D. radiodurans* at the start (t0h) and end (t3h) of the time-lapse experiment. (B) Effects of ampicillin treatment on the growth rate of the external (blue) and internal (red) septa, and of the outer cell wall (black) corresponding to the perimeter of the cells. N>25. Statistical test: One-way ANOVA. Ns: non-significant, \*\*\*\* p-value < 0.0001. (C) Plot illustrating the inhibition of both the external (red) and internal (orange) septal growth by treatment with 1 µg/ml ampicillin. After 1h of treatment, the lengths are the septa shorten suggesting they are being degraded. (D) Schematic diagram of a *D. radiodurans* diad, illustrating the different features and measurements made to probe the effect of ampicillin treatment. (E) Distortion of the cell morphology as a result of ampicillin treatment is particularly visible and is reflected in the marked change in the diameter:perimeter (d/p) ratio that is significantly increased in the presence of ampicillin (red). N>45. Statistical test: unpaired t-test. \*\*\*\* p-value < 0.0001. (F) Schematic model of the two PG synthesis machineries at play in *D. radiodurans*. The outer cell wall PG synthesis machinery (orange) appears to be insensitive to ampicillin and may well be localized to the junction between the outer cell envelope and the growing septa. In contrast, the septal PG synthesis machinery (purple) is very sensitive to ampicillin and is located mainly at the leading edge of the growing septa.

budding of the new septa, where a distinctive bright PG-labelled ring was observed (**Suppl. Figure 4.14**). These rings were occasionally seen in untreated cells, but were much more abundant in ampicillin-treated cells and in particular in samples pre-grown for 2 hours in the presence of the  $\beta$ -lactam antibiotic, where approximately 50% of the cells displayed such ring-shaped PG labelling (**Suppl. Figure 4.14B**). The initial PG synthesis at the start of septation thus appears to be unaffected by ampicillin, while subsequent growth and extension of the septa is fully arrested by this treatment. One PG machinery located at the junction between the outer cell wall and the start of septation may therefore be involved in both outer cell wall synthesis and initiation of septation, but a distinct set of proteins likely located at the leading edge of the growing septa appear to be responsible for PG synthesis across the dividing cells (**Figure 4.5F**). This finding is supported also by the pulse-chase experiments (**Suppl. Figure 4.13**) in which we observed that most of the labelling of the septal regions, but not of the outer cell walls was lost after the chase period, indicating that the PG structure and/or maturation process are quite distinct in these two types of cell wall.

## FtsZ is present at the tips of septa

We investigated the location of FtsZ, one of the key players in bacterial cell division, in dividing *D. radiodurans* cells using both fluorescence microscopy and cryo-ET. Two strategies were used to fluorescently label FtsZ: (i) immunolabelling of an endogenously HA-tagged FtsZ or (ii) endogenous tagging of FtsZ with a photoconvertible fluorescent protein, mEos4B. The latter was compatible with live cell imaging, but this genetically modified strain of *D. radiodurans* showed altered cell morphology (forming many large cells with likely impaired septation) and only a small fraction of cells exhibited fluorescence signal and visible Z-rings (**Figure 4.6A**). In contrast, the strain expressing HA-tagged FtsZ grew very well with no obvious morphological defects and FtsZ could be detected with an anti-HA antibody, after fixing and permeabilizing the cells, by either confocal or dSTORM microscopy (**Figure 4.6A-B**). Both strategies indicated that *D. radiodurans* FtsZ forms ring- or oval-shaped structures of various sizes as reported for other bacteria, some of which appear to be incomplete. Dual labelling of FtsZ and the cell membrane also revealed that FtsZ locates to the leading edge of growing septa at all stages of septation, including very early stages when septa are not yet visible by fluorescence microscopy (**Figure 4.6B**). At these early stages, FtsZ also appeared to form mostly incomplete Z-rings (**Figure 4.6B**).

In several tomograms, of a double-arched structure could be visualized in the cytoplasm at ~15 nm from the IM border of the leading edge of the septum, which likely corresponds to FtsZ (outer arch) and its cellular partner, the membrane-bound FtsA<sup>110</sup> (inner arch; **Figure 4.6C**). These two arches follow the curvature of the septal tip with the outer FtsZ arch typically between 20 nm and 50 nm in length. As in our fluorescence microscopy data, these structures were observed at all stages of the septation process from budding septa all the way to almost fusing septa. In the side projections of the tomograms, FtsZ was observed to form long straight filaments along the flat leading edge of the closing septa with an inter-filament distance of approximately 5 nm in good agreement with previous reports of *in situ* FtsZ

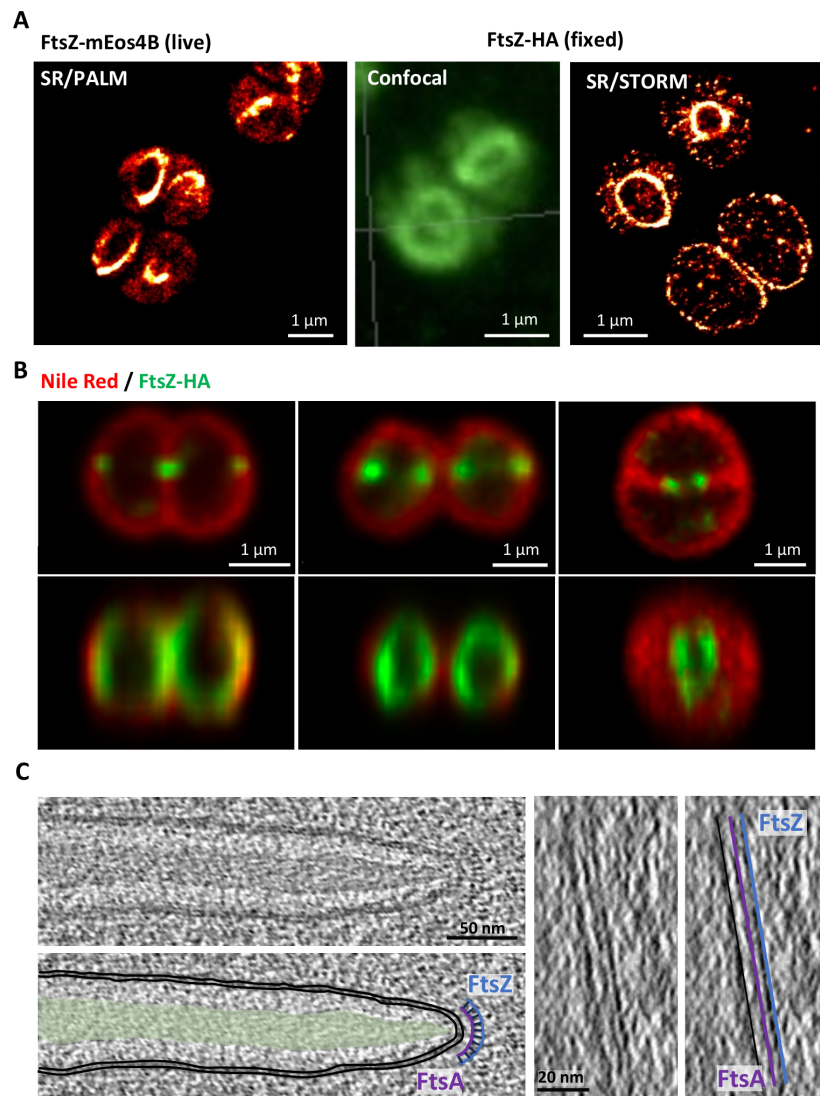


**FIGURE 4.6:** Localisation of the key cell division factor, FtsZ, in *D. radiodurans*.  
(caption on the next page)

**FIGURE 4.6:** (A) 3D fluorescence imaging of FtsZ in *D. radiodurans*. Left: 3D PALM imaging of *D. radiodurans* bacteria expressing FtsZ-mEos4B forming well-defined ring-like structures. Middle and right: 3D confocal images (middle) and super-resolved dSTORM images (right) of immunolabelled *D. radiodurans* bacteria expressing FtsZ-HA. Z-rings of various sizes and shapes were observed. Scale bar: 1 µm. (B) Two-colour labelling of *D. radiodurans* bacteria expressing FtsZ-HA. FtsZ (green) was immunolabelled while the membrane was stained with Nile Red (red). From left to right: illustrations of different stages of the division process. At all stages, FtsZ localizes to the leading edge of the septa. Top panels: top views, lower panels: side views. Scale bar: 1 µm. (C) Left: 2D slice of a typical tomogram of *D. radiodurans* illustrating the double-arched structure of FtsA (purple) and FtsZ (blue) located 15 nm away from the IM bilayer (black) on the cytoplasmic side of the growing septum. Inter-filament distance was estimated to be approximately 5 nm. Scale bar: 20 nm. The top panel shows a 2D slice of a tomogram and the lower panel the same region with segmentations of the various cell wall layers (colors as in Fig. 2A) and the double-arched structure. Scale bar: 50 nm. Right: Side-view of the FtsA and FtsZ filaments highlighted in the right panel in purple and blue respectively.

filaments<sup>137,138</sup> (**Figure 4.6C**). Interestingly, FtsZ was not detected when membrane protrusions were present at septal tips, but was sometimes seen either above or below these structures, which may explain the discontinuous ring structures observed by fluorescence microscopy (**Figure 4.6A-B**).

## 4.4 Discussion

In this study, we have combined live conventional and super-resolution fluorescence microscopy with *in situ* cryo-ET imaging of *D. radiodurans* to follow the process of septation in this relatively large, spherical bacterium. This work provides important insight into (i) the complex cell wall composition of this unusual Gram-positive bacterium and the various stages of its maturation, (ii) its distinct mode of septation involving a “sliding doors” mechanism, and (iii) the molecular mechanisms underlying PG synthesis and the coordinated septal growth that ensures successful fusion of the septa originating from opposite sides of the cell.

*D. radiodurans* is a spherical bacterium that is known to possess a unique cell envelope including an outer S-layer, which has been the object of numerous studies over the past decades<sup>132,139–147</sup>. Like other members of the *Deinococcus-Thermus* phylum, *D. radiodurans* exhibits features of

both Gram-positive and Gram-negative bacteria, and may be considered as a primitive form of Gram-negative bacteria<sup>103</sup>. *D. radiodurans* is indeed lacking lipopolysaccharides commonly found in Gram-negative bacteria, possesses a thick PG layer (35-55 nm) typical of Gram-positive bacteria and yet its cell envelope is composed of two membrane bilayers characteristic of Gram-negative bacteria<sup>148</sup>. The exact composition and structure of this unusual cell wall has been the object of much controversy in the recent years, notably regarding the outer layers linking the PG to the outermost S-layer hexagonal lattice structure. Our cryo-ET analysis of the outer cell wall composition fully supports the model recently proposed by Bharat and colleagues, in which the whole outer cell envelope is ~100 nm in thickness and composed of two membranes in between which can be found a thin periplasmic space and two thicker layers, the PG and SlpA layers<sup>132</sup>. The S-layer forms an additional coat located ~18 nm above the outer membrane<sup>141</sup>. The SlpA layer takes its name from the major protein constituent of this layer, the SlpA protein, a trimeric porin-like protein that is embedded in the outer membrane and stretches across the SlpA layer via a long coiled-coil region to connect to the PG layer<sup>132</sup>. The predicted length of this assembly (~28-29 nm) is in good agreement with our estimated thickness of the SlpA layer (35 nm). Interestingly, in our tomograms, we observe a distinctive white line between the PG and SlpA layers that may correspond to the sites at which the flexible N-terminal SLH domain of SlpA attaches to the PG layer.

In *D. radiodurans*, daughter cell separation driven by the activity of autolysins<sup>149</sup> (four of which have been identified in *D. radiodurans*<sup>150</sup>) is uncoupled from septation, with these two phenomena occurring in successive cell cycles. This is different from previously studied models of bacterial cell division in which both processes occur at the same time to produce two daughter cells. Moreover, dividing *D. radiodurans* cells exhibit three types of cell wall displaying distinct layer compositions and characteristics that reflect different stages of cell wall maturation. Our cryo-ET data revealed that the cell wall in the growing septa is initially composed of a central PG layer surrounded by a lipid bilayer, with a low-density periplasmic space

in between these two layers. The PG layer thickens progressively as the septa grow and this thickening continues after completion of the septation within the central septum. The additional layers observed exclusively in the outer envelope (SlpA layer and OM bilayer) are only added at a late stage of maturation when the splitting of the cells is initiated. This differs from other bacteria and notably *S. aureus* and *E. coli* in which growing septa already exhibit two distinct PG layers (one for each daughter cell) separated by a low-density region<sup>104,108</sup>. This difference may be explained by the temporal separation between septation and cell splitting in *D. radiodurans*, allowing PG hydrolysis and the synthesis of the two additional cell wall layers (and eventually the outer S-layer) to occur in the subsequent cell cycle within the central septum in a tightly coordinated manner. First, the single thick PG layer found in this central septum region is separated through the action of hydrolases into two equal PG layers and the SlpA layer is synthesized in between these two PG layers before rapid synthesis of the OM bilayer to allow the incorporation of the abundant SlpA protein into both the OM and the SlpA layer. These two additional layers efficiently protect *D. radiodurans* from its external environment and must therefore be completed before the splitting of the daughter cells can take place. The splitting process appears to be initiated from the outer boundaries of the cell at sites of outer membrane invagination and then moves inwards towards the center of the diad until full separation of the two daughter cells.

PG synthesis and its subsequent remodelling are key processes in bacterial septation. In *D. radiodurans*, PG synthesis has been shown to occur in both the septal regions and within the outer cell wall<sup>129</sup>. Here, by transiently incorporating aDA into the cell wall to label sites of active PG synthesis and remodelling<sup>125,128</sup>, we show that the leading edge of the septa constitutes the main site of PG synthesis in dividing *D. radiodurans* and that subsequent rounds of synthesis build on the existing PG in an inwards direction until the opposing septa meet and fuse. However, we also observed that the growing septa were very often tapered with a thinner PG layer at the leading edge than at the root of the septum. This has previously been reported also in *S. aureus*<sup>106,108,128</sup> and suggests that PG synthesis may

not be restricted to the leading edge of the septa. In fact, the rapid loss of PG labelling within the growing septa during the chase phase of our aDA pulse-chase experiments suggests that septal PG is rapidly being remodelled and modified in this region. In contrast, aDA incorporation within the outer cell wall was more stable, suggesting also that different machineries may be at a play in these two regions of cell wall. This was further confirmed by our timelapse experiments performed in the presence of ampicillin, a  $\beta$ -lactam antibiotic that is known to specifically inhibit certain classes of PBPs. As has been reported for the ovococci, *Lactococcus lactis*<sup>127</sup> and *Streptococcus pneumoniae*<sup>151,152</sup>, we found that ampicillin treatment specifically impedes septation and not outer cell wall expansion needed for cell growth. In ovococci, this effect has been attributed to the specific inhibition of the class B PBP, PBP2x, that is involved in septation<sup>127,151,153</sup>. The genome of *D. radiodurans* encodes for two class A PBPs and one class B PBP, that is annotated as PBP2 (DR1868). Although little is known so far about the respective roles of these PBPs in *D. radiodurans*, our observations suggest that *D. radiodurans* PBP2 may be the target of ampicillin and thus largely responsible for PG synthesis at the leading edge of the growing septa.

Whereas in most cocci and ovococci studied so far, septation advances centripetally from the outer cell wall like a closing diaphragm, with this study, we provide further evidence that septation in *D. radiodurans* is quite distinct. It proceeds via a “sliding doors” mechanism, also described in an earlier study as a “septal curtain”<sup>111</sup>, in which the two septa originating from opposite sides of the cell grow inwards with a flat leading edge creating a central gap stretching from the top to the bottom of the cell. As septation progresses, the leading edge becomes more curved and eventually when the two septa come close to each other, fusion occurs and the septal disk is filled. Why *D. radiodurans* uses such a remarkable mode of septation remains to date a mystery. Physical constraints associated with the relatively large size (2-3  $\mu\text{m}$  in diameter) of *D. radiodurans*, its cell morphology (diads and tetrads) or its mode of division in two alternating perpendicular planes may have contributed to the development of this unusual division mechanism.

With such a septation process, ensuring the opposing septa are correctly

aligned and meet at mid-cell for septal fusion constitute major challenges for the bacteria. The latter is, in part at least, achieved by differential growth rates of the external and internal septa. Indeed, we observed that the septum originating from the external side of the diad grows at a faster rate and initiates its growth shortly before the septum originating from the central septum to compensate for the longer distance needed for it to reach mid-cell. This study also identifies two other important factors that may facilitate this process: (i) the flexible membrane protrusions observed at the leading edge of septa, and (ii) the presence of FtsZ at septal tips and the formation of Z-rings that may constitute a physical link between the opposing septa.

These two mutually exclusive features were observed at the leading edge of *D. radiodurans* septa. In many instances, particularly at early stages of the septation process, membrane protrusions, adopting a variety of conformations, were observed at the tips of the growing septa. Similar structures were reported in early studies of *D. radiodurans*<sup>131,133</sup> and other bacteria<sup>154,155</sup>, but were later considered as artefacts of chemical fixation procedures used for electron microscopy sample preparation<sup>156–158</sup>. In our case, these structures were observed *in situ* in near native conditions (vitrified cells) strongly suggesting that they are not artefacts. Instead, we propose that these thin mobile membrane extensions, missing a PG layer, may provide the necessary flexibility to allow septa to align with their opposing septa during the initial steps of septation. In contrast, we found that the presence of FtsZ at the septal tips was associated with more rigid and well aligned septa, suggesting that the assembly of the FtsZ ring may constitute a critical step in the proper alignment of opposing septa, possibly through a direct bridging of the two “sliding doors”. Importantly, FtsZ was only observed at the leading edge of septa containing a well-defined central PG layer that extended almost to the lipid bilayer significantly reducing the low-density periplasmic space in these tips. In addition to possibly bridging the opposing septa via its ring formation, FtsZ is likely also acting as an anchor for the recruitment of the PG synthesis machinery needed for septation, as has been reported for many other bacteria (recently

reviewed in Barrows and Goley<sup>159</sup>, McQuillen and Xiao<sup>160</sup>, Cameron and Margolin<sup>161</sup>).

Although FtsZ was never seen on the membrane protrusions themselves, in several tomograms FtsZ was observed either above or below the protrusions. The leading edge of a given “sliding door” may thus be dynamic and heterogeneous, composed of both flexible regions bearing membrane protrusions and more rigid areas in which FtsZ can assemble to drive PG synthesis. We thus propose a model for *D. radiodurans* septation (**Figure 4.7**) in which membrane synthesis may precede PG synthesis during the early stages of septation, leading to the formation of membrane protrusions. The subsequent assembly of FtsZ filaments at the leading edge of the septa followed by the formation of the Z-ring would then act as a cue for the recruitment and activation of PG synthesis in order to progressively fill and rigidify the growing septa. Further studies will certainly be needed to decipher the precise roles of FtsZ and to identify the other key players in this complex and intriguing septation process.

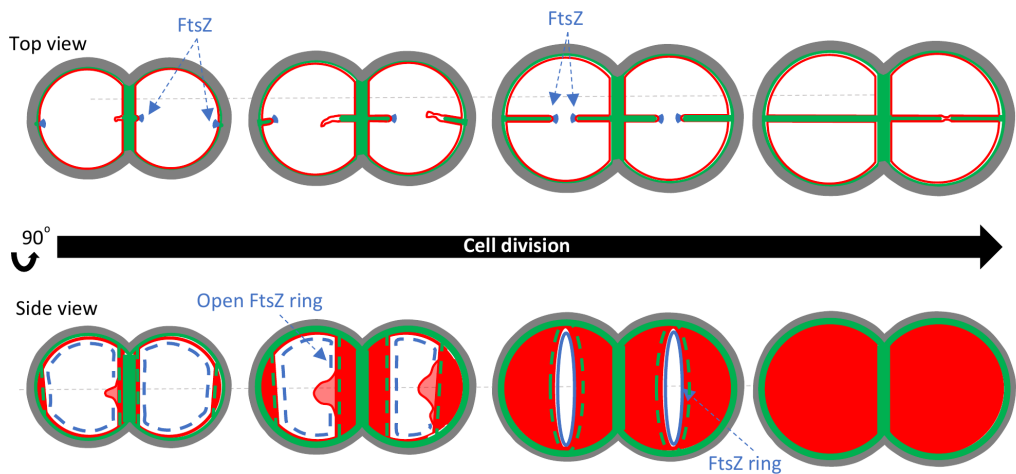


**FIGURE 4.7: Schematic model of the septation process in *D. radiodurans*.** Top and side views are illustrated at various stages of the division process. For simplicity, only the IM (red) and the PG layer (green) are highlighted. FtsZ is shown in blue with incomplete Z-rings as dashed lines and complete Z-rings as a full line. Flexible membrane protrusions are visible at early stages of the septation process, which progressively become filled with PG providing the necessary rigidity to achieve a solid and well-aligned cross-wall. FtsZ plays a key role in targeting the PG synthesis machinery to the leading edge of the growing septa and may also facilitate the proper alignment of opposing septa by bridging the two independent elements via Z-ring formation.

## 4.5 Materials and methods

### Bacterial cultures

*D. radiodurans* (DR) strains used in this study are listed in Table S1. All strains were derivatives of the wild-type strain R1 ATCC 13939 (DR<sup>WT</sup>). The genetically engineered strain of *D. radiodurans* expressing FtsZ fused to mEos4B (DR-FtsZ-mEos4B) was obtained by the tripartite ligation method as described recently<sup>162</sup>. A synthetic gene encoding mEos4B was amplified together with the kanamycin resistance cassette by PCR as were the regions (~500bp) flanking the insertion site (3' end of *ftsZ* gene and region immediately downstream of the *ftsZ* gene) using oligonucleotides listed in Table S2. After restriction digestion the three fragments were ligated together and transformed into *D. radiodurans*. Transformants were selected on TGY agar plates containing 6 µg/ml kanamycin, leading to allelic replacement on one

genome copy. Because *D. radiodurans* is multigenomic, the transformant colonies were streaked three times successively on selective medium to ensure that all copies of the genome had incorporated the foreign DNA. This was then confirmed by PCR analysis and DNA sequencing. *D. radiodurans* cells were grown aerobically at 30°C in a shaking incubator (160 rpm) in Tryptone-Glucose-Yeast extract 2x (TGY2X) medium supplemented with the appropriate antibiotics. Typically for microscopy experiments, *D. radiodurans* cells were pre-grown the day before and then diluted for an overnight growth until reaching exponential ( $OD_{650} \sim 0.3\text{-}0.5$ ) the next morning. Optical density measurements were made on a Clariostar (BMG Labtech) plate reader.

### Cell labelling for confocal and single-molecule localization (SMLM) microscopy

Membranes of exponential phase DR bacteria were stained by addition of Nile Red (30  $\mu\text{M}$  for confocal microscopy and 30-100 nM for SMLM) to the growth medium of cells (1 ml) for 10 min at room temperature. The cells were then harvested by centrifugation and resuspended in 200  $\mu\text{l}$  TGY2X for confocal microscopy or instead washed 3 times in DPBS (3x 1 ml) and resuspended in 200  $\mu\text{l}$  DPBS for SMLM. 3-5  $\mu\text{l}$  of cell suspension was then deposited on a 1.5% (w/v) low melting agarose (LMA; Bio-Rad) pad prepared using a gene frame positioned on a glass slide. Two stripes of LMA were cut out on either side of the deposited sample for good aeration of the bacteria before a 1.5H coverslip was added to cover the frame. For PALM imaging of FtsZ-mEos4B, DR-*FtsZ-mEos4B* cells were grown to exponential phase, washed twice with DPBS and deposited directly on a 1.5% LMA pad prepared in DPBS using a gene frame positioned on a glass slide. To visualize dividing bacteria in different orientations, an alternative set-up was also used (**Suppl. Figure 4.8B**) in which 10  $\mu\text{l}$  of the cell suspension was placed on the bottom of a glass dish and cells were allowed to sediment for 2 min. Excess liquid was then gently removed using a pipette and after 2 minutes of air-drying, 10  $\mu\text{l}$  1.5% LMA equilibrated at 37°C was poured

over the cells. The LMA was prepared in TGY2X medium for timelapse confocal imaging and in DPBS for PAINT imaging of Nile Red labelled bacteria. For PG labelling, 1.5 ml of exponential phase DR cultures were centrifuged at 3000xg and resuspended in 200  $\mu$ l TGY2X medium to which 50  $\mu$ l 10 mM azido-D-Alanine (aDA) was added<sup>125,135</sup>. Pulse labelling was typically performed for 10 min at 30°C, before washing the cells two times with cold DPBS to stop cell growth. Cells were then resuspended in 48  $\mu$ l 30  $\mu$ M DBCO-AF488 or DBCO-AF647 (dSTORM) diluted in DPBS and incubated on ice for 45 min to allow the DBCO-AF488/AF647 to enter the bacteria and react by click chemistry with the incorporated aDA. When ready to be imaged, labelled cells were washed two times with DPBS and resuspended in 100  $\mu$ l DPBS. For immunolabelling of HA-tagged FtsZ, DR-*FtsZ-HA* (strain GY15705) bacteria were grown to exponential phase. 0.5 ml culture was flash-frozen using liquid nitrogen in DPBS-glycerol buffer (19% glycerol) supplemented with 2.58% formaldehyde. Cells were then fixed through slow thawing of these samples on ice overnight, washed twice in DPBS and resuspended in 100  $\mu$ l DPBS. Cells were permeabilized by treatment with 4 mg/ml lysozyme at 37°C for 30 min followed by the addition of 0.1% Triton X-100 for 5 min at 25°C. Cells were then washed twice with DPBS and incubated with a mouse anti-HA antibody (1:400 dilution in PBS-Tween0.05% supplemented with 2% BSA) for 1h at 37°C. After several washes with PBS-Tween0.05%, cells were incubated with anti-mouse secondary antibody coupled to either Alexa fluor 488 (for confocal) or Alexa Fluor 647 (for dSTORM) for 1h at 37°C. After a final washing step, the bacteria were deposited on a 1.5% LMA pad prepared in DPBS as described above. For dSTORM experiments, the LMA was prepared in glucose buffer (62.5 mM Tris-HCl pH 8.0, 12.5% glucose, 12.5 mM NaCl) and contained 0.1 M MEA and 1x GLOX (prepared from the 10x GLOX solution composed of 10 mM Tris-HCl pH 8.0, 50 mM NaCl, 56 mg/ml Glucose oxidase and 13.6 mg/ml Catalase). For confocal microscopy, the LMA was prepared as above in TGY2X.

## Confocal data acquisition and processing

Spinning-disk confocal microscopy was performed using an Olympus IX81 inverted microscope equipped with a Yokogawa CSU-X1 confocal head. The excitation laser beam (Ilas2 laser bench, GATACA systems) was focused to the back focal plane of a 100X 1.49-numerical-aperture (NA) oil immersion apochromatic objective. Series of Z-planes were acquired every 132 nm using a PRIOR N400 piezo stage to achieve cubic voxels. Fluorescence excitation was performed at 488 nm for DBCO-AF488 and 561 nm for Nile Red. Fluorescence emission was collected with an Andor iXon Ultra EMCCD camera through a quad-band Semrock™ Di01-T405/488/568/647 dichroic mirror and single-band emission filters adapted to each fluorophore used: 520 nm for DBCO-AF488 (FF02-520/28 Semrock™), and 600 nm for Nile Red (ET600/50m Chroma™). Data acquisition was performed using Metamorph 7.10 (Molecular devices). Acquired images were processed using Imaris (Oxford Instrument™) to correct for the possible translational (in x, y, and z directions) and rotational (z axis) drifts, followed by correction of the timepoints intensities using the embedded “Normalized timepoint” routine (Imaris XT package). When needed, Kymograph builder plugin in Fiji was applied to datasets. Coordinates of kymograph boundaries were then extracted in Fiji and used to calculate the septal closure rate in growing cells.

## SMLM (PAINT/dSTORM) data acquisition and processing

PAINT and dSTORM data were acquired on an Olympus IX83 inverted motorized microscope equipped with a SAFE 360 (Abbelight) SMLM set up, and using a UPLXAPO 100x oil immersion objective (NA 1.5, Olympus™). Data collection was performed using simultaneous dual camera acquisitions (50/50 splitter; Orca Fusion sCMOS – Hamamatsu™) with an astigmatism lens intercalated in the emission path of the direct camera to reconstruct 3D volumes in parallel with 2D single-molecule localization determination. Data was acquired at 27°C under continuous HiLo illumination with 400 W/cm<sup>2</sup> 561 nm light or 642 nm light and a typical frame time of 10 ms

for PAINT and 50 ms for dSTORM. Typically, 40,000 – 60,000 frames were acquired per dataset under constant activation of the Zero Drift Control system (ZDC2 at 830 nm) to limit Z-drift during acquisitions, and at constant temperature (Digital Pixel™ blind cage incubator and water jacket around the objective set at 27°C). Typical 3D reconstructions are limited by the astigmatic point spread function to a few hundreds of nm. When specified in the corresponding figure legends, we collected stacked localizations at 400 nm distance and reconstructed the cumulated localizations to obtain larger reconstructed volumes. SMLM data was processed using NeoAnalysis software (Abbelight™) using default values for maximum likelihood estimations (MLE) of the gaussian localizations fittings. Further filtering of the dataset was performed using Thunderstorm plugin<sup>163</sup> in Fiji<sup>164</sup> to correct for possible drift in x and y directions (using cross-correlation), and restrict the localizations to limit the spreading of values for sigma, intensity, and uncertainty values.

## Sample preparation, vitrification and cryo-FIB milling for cellular cryo-ET

A 20 ml pre-culture of *D. radiodurans* cells was grown overnight to stationary phase ( $OD_{650} \sim 1.8$ ) in TGY2X medium in a shaking incubator at 30°C and 170 rpm and then diluted to  $OD_{650} \sim 0.1$  in 20 ml fresh medium the next day and grown further until reaching exponential phase ( $OD_{650} \sim 0.4$ ). The culture was then centrifuged for 5 min at 4000 rpm, the pellet collected in a 1 ml Eppendorf tube and washed three times in 1 ml PBS. Shortly before plunge-freezing, the pellet was resuspended in PBS to reach a final volume of  $\sim 60 \mu\text{l}$ . Plunge-freezing was performed in liquid ethane/propane mixture using Vitrobot Mark IV (Thermo Fisher Scientific) at 23°C, 90% humidity, with blot force -5 to 10, blot time 8 to 10 sec and wait time 30 sec. 4  $\mu\text{l}$  of cell suspension were deposited per Quantifoil Cu 1.2/1.3, 200 mesh grid (Micro Tools GmbH, Großlobichau, Germany), glow-discharged immediately prior to use. Frozen grids were clipped into standard AutoGrid specimen cartridges (Thermo Fisher Scientific) marked to keep track of

the milling direction for the subsequent orientation in the Titan Krios (ThermoFisher Scientific) microscope, and stored in liquid nitrogen until usage. For cryo-FIB milling, the clipped grids were mounted into a 45° pre-tilt shuttle and transferred into a Scios cryo-FIB/scanning electron microscope dual-beam microscope (Thermo Fisher Scientific). To reduce curtaining and enhance sample conductivity, the grids were sputter-coated with organometallic platinum using the gas injection system. The Gallium milling was performed at a 17° to 23° stage tilt angle, dependent on the milling location on the grid. Lamellae were prepared in a stepwise manner, progressively reducing the FIB current from 0.5 nA to remove the bulk material to 30 pA for the final polishing step, ending up with lamellae of 200-300 nm thickness. Progress of the milling process was monitored using the SEM operated at 10 kV and 50 pA. Grids were stored in liquid nitrogen until transfer into the Titan Krios microscope.

### Cryo-ET data acquisition

Data was collected using a Titan Krios operated at 300 keV and equipped with a BioQuantum post-column energy filter (Gatan, Pleasanton, CA) and a K2 Summit direct detector (Gatan, Pleasanton, CA). The energy filter was operated with a 20 eV slit width. Image acquisition was performed using SerialEM software. To identify regions of interest (ROI) and account for the lamella pre-tilt, lamella montages were acquired at an intermediate magnification of 17 Å/pixel, and at +13° tilt. Tilt series were then recorded with the detector operated in super-resolution mode, at a nominal magnification of 33,000x corresponding to 2.173 Å/pixel at the specimen level. Data were collected at ~3 µm defocus following a grouped dose-symmetric tilt scheme in 3° increments, with a tilt range depending on the ROI position and thickness, typically ±50° to ±60°. The dose was kept constant for all tilts in each given tilt series and adjusted such as to reach the total per tilt series dose of ~140 e/Å<sup>103</sup>. In total, 45 tilt series were collected for the presented analysis.

## Cryo-ET image processing, visualization, segmentation and analysis

Data preprocessing was carried out in Warp<sup>23</sup>: gain reference and motion correction, and CTF estimation were performed following the standard Warp<sup>23</sup> procedure for tomography data with the following non-default parameters: binning 1x, CTF grid dimensions 5x5x1, and motion grid dimensions 5x5x15. The dataset was then manually curated to remove low quality tilt images and extracted into stacks for tilt series alignment. Alignment was performed in batch with AreTomo<sup>61</sup>, using our in-house script Waretomo ([source code](#)) to integrate it seamlessly with Warp<sup>23</sup>. Alignment parameters were reimported in Warp<sup>23</sup> and used to reconstruct full tomograms at a resolution of 17.41 Å/pixel. Tomograms were denoised using Topaz<sup>26</sup> to help with picking and inspection. All images of tomogram slices presented in this manuscript come from non-denoised tomograms, averaging over 5 slices. Cell walls were annotated using the surface annotation tool in blik<sup>72</sup> ([source code](#)). These annotations were then used to generate the 3D surface visualizations of the septa and cell wall profiles using the surface tool in blik<sup>72</sup>, resampling the tomogram perpendicularly to the surfaces to obtain “straightened” wall volumes. 2D projections were obtained by averaging over the Z dimension of the resampled volumes. 1D density profiles were calculated in Fiji<sup>164</sup> on 76-pixel sections of the 2D projections and used to measure cell wall dimensions using the point to point measuring tool in Fiji<sup>164</sup> as detailed in [Suppl. Figure 4.15](#).

## 4.6 Acknowledgements

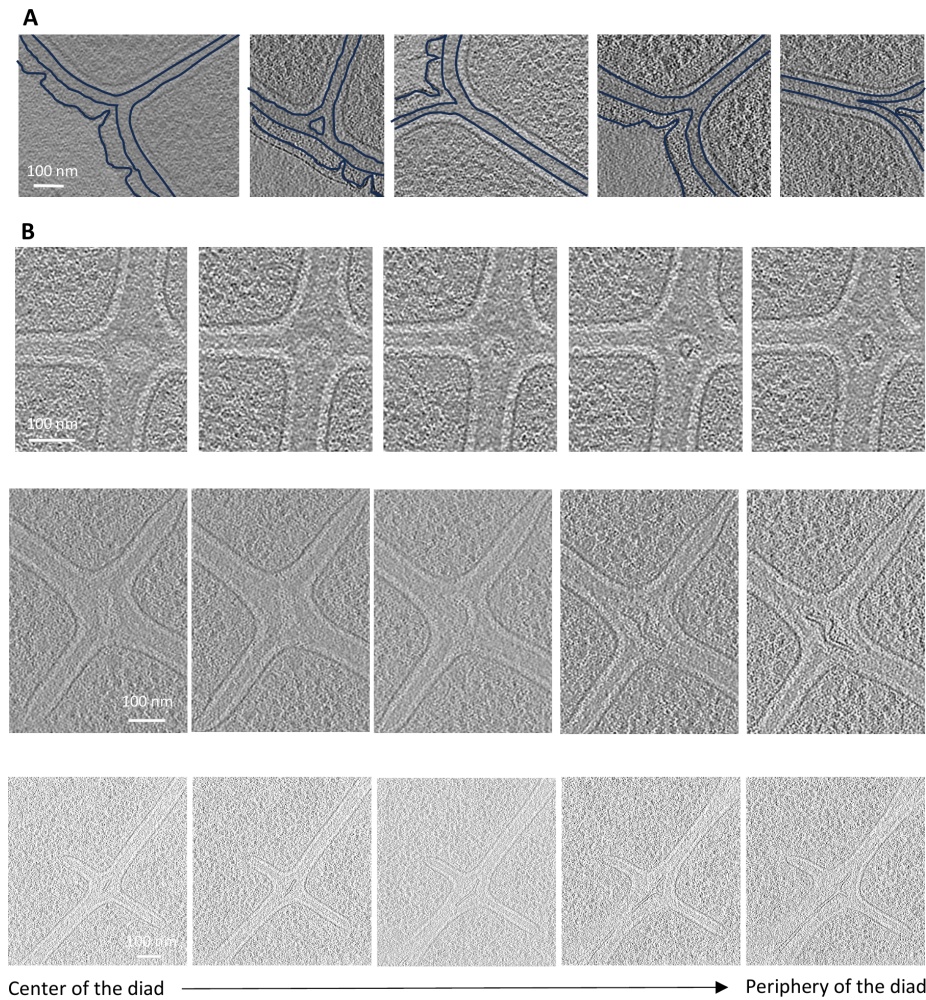
IBS acknowledges integration into the Interdisciplinary Research Institute of Grenoble (IRIG, CEA). The optical imaging was carried out on the M4D imaging platform of the Grenoble Instruct-ERIC center (ISBG; UAR 3518 CNRS-CEA-UGA-EMBL) within the Grenoble Partnership for Structural Biology (PSB), supported by FRISBI (ANR-10-INBS-0005-02) and GRAL, financed within the University Grenoble Alpes graduate school (Ecole Uni-

versitaires de Recherche) CBH-EUR-GS (ANR-17-EURE-0003). We thank staff on the M4D platform at IBS for their help for data acquisition and processing. Electron microscopy sample preparation, cryo-FIB milling and cryo-ET data collection were performed at the Umeå Centre for Electron Microscopy (UCEM). IG thanks the UCEM staff for training and support.

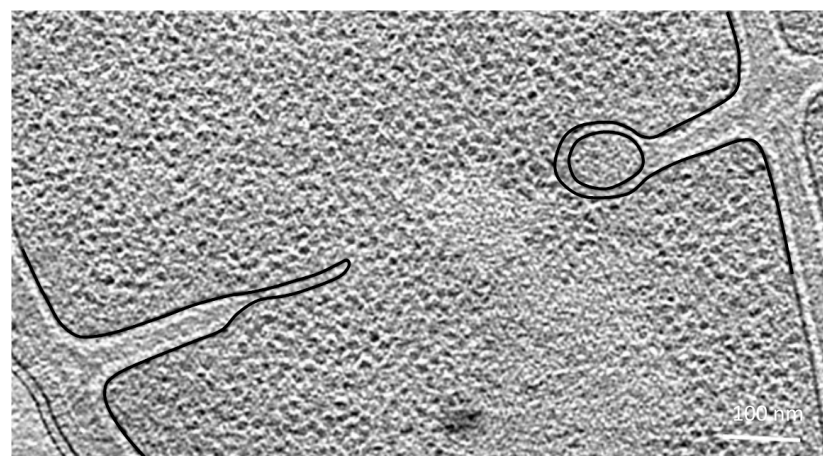
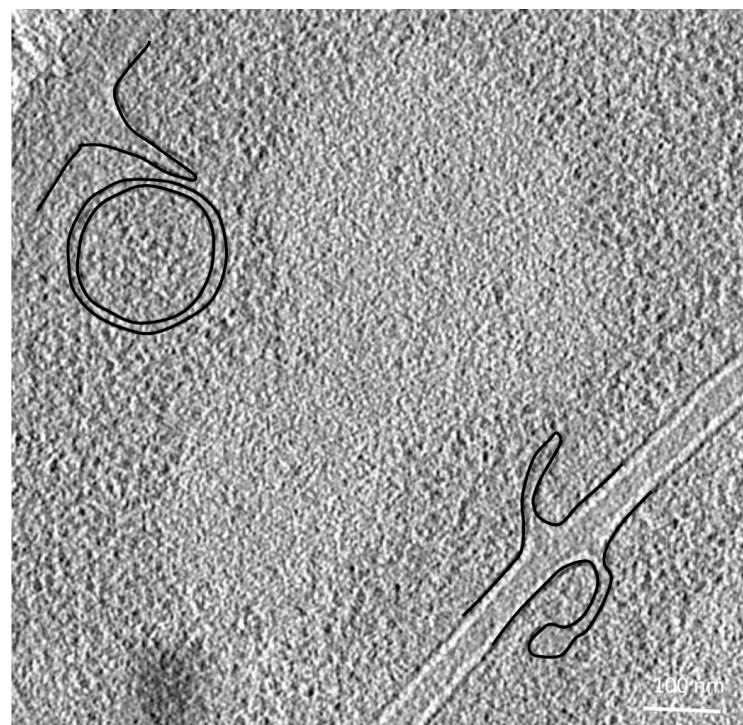
## 4.7 Funding

The fluorescence microscopy work benefitted from funding from the CEA Radiobiology program and the Agence Nationale de la Recherche (grant N ° ANR-22-CE11-0029-01). The electron microscopy work was supported by visiting professorship fundings from the Molecular Infection Medicine Sweden (MIMS), the Wenner Gren foundation and the the Swedish Research Council (VR) Tage Erlander to IG. LG's PhD position was funded by GRAL, a project of the University Grenoble Alpes graduate school (Ecole Universitaires de Recherche) CBH-EUR-GS (ANR-17-EURE-0003).

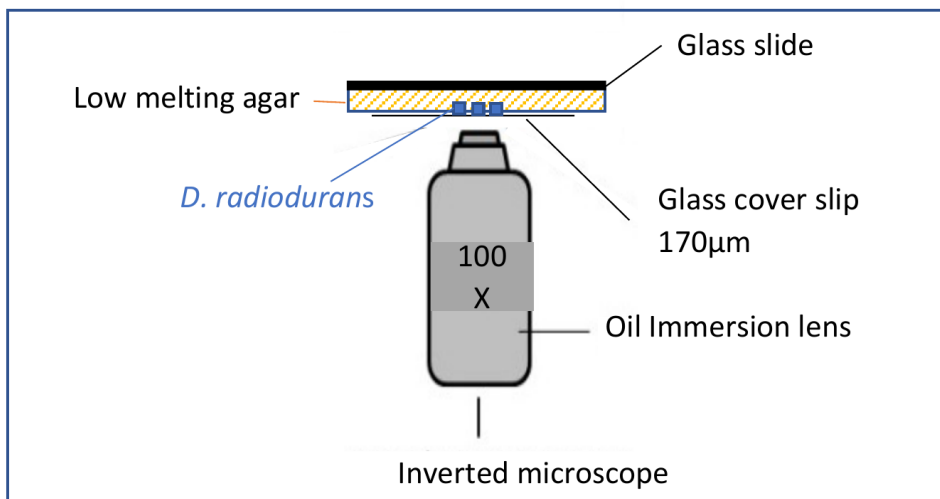
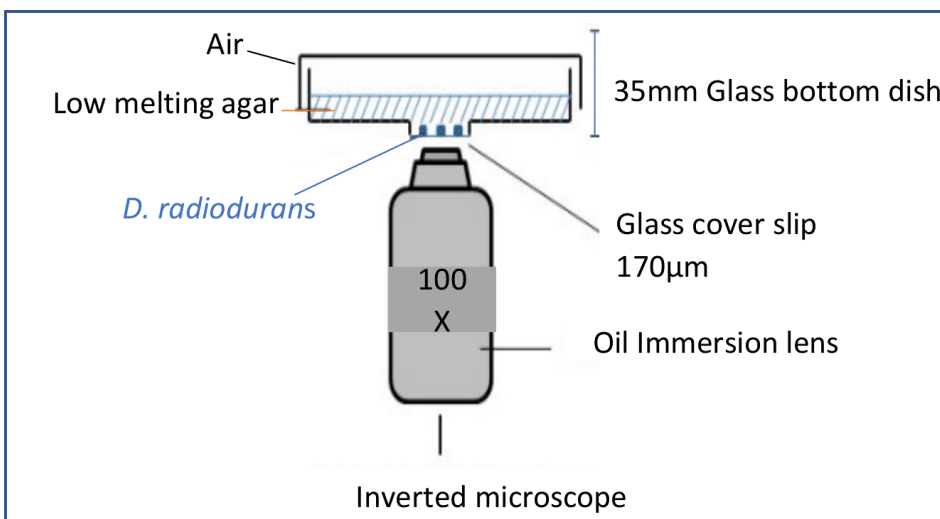
## 4.8 Supplemental figures



**FIGURE 4.8: Cell wall junction examples.** (A) Examples of junctions between the outer cell wall and the growing septa observed in various tomograms of *D. radiodurans*. The borders of the different layers composing the cell wall are highlighted in dark blue. (B) Examples of regions in which splitting of the daughter cells were observed. From left to right: slices through the tomograms with the earlier stages of cell splitting illustrated on the left (located towards the center of the diads) and the later stages on the right (located closer to the outer periphery of the bacteria).



**FIGURE 4.9: Membrane protrusion examples.** Examples of membrane protrusions observed in various tomograms of *D. radiodurans* at the leading edge of growing septa. The IM is highlighted in black.

**A****Classical set-up****B****New set-up**

**FIGURE 4.10: Microscopy set-ups for timelapse 3D confocal video-microscopy.** (A) Classical set-up in which cells are seeded on a low melting agarose pad and then overlaid with a glass coverslip. In this set-up, cells are mostly positioned in the same orientation orthogonal to the two successive division planes. (B) New set-up in which cells are deposited on the glass of a glass-bottomed dish and then coated with low melting agarose. The pouring of the melted agarose over the cells results in a wider distribution of cell orientations allowing to view the septation in tilted cells.

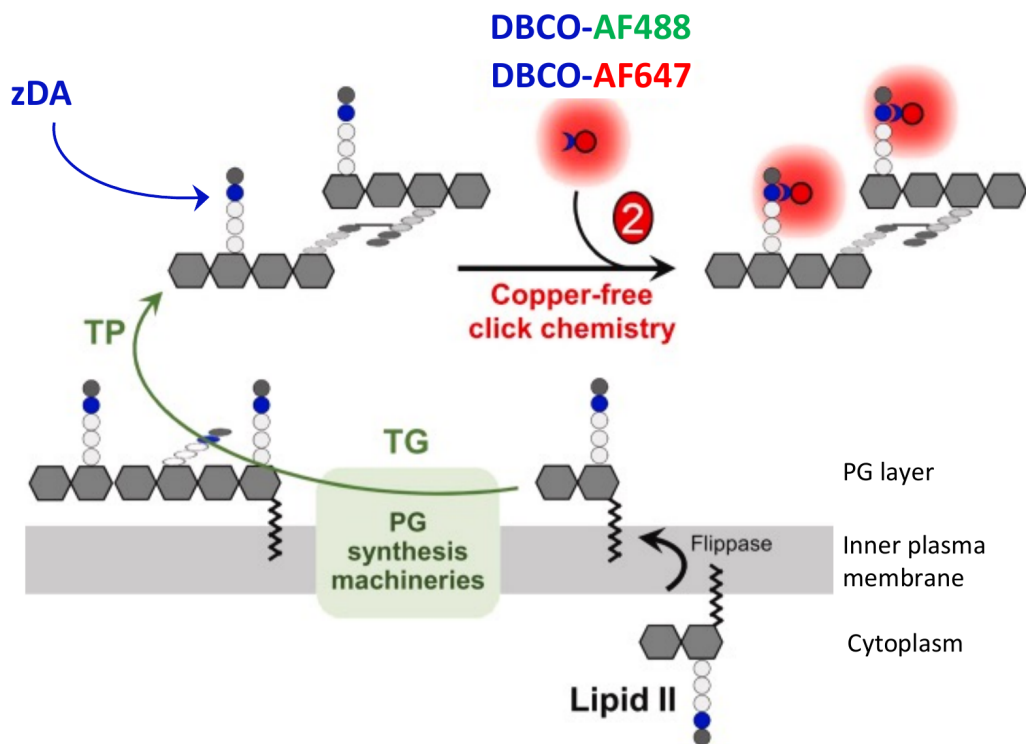


**FIGURE 4.11: PG labelling schematic.** Schematic diagram of the mode of zDA incorporation and labelling of PG in growing *D. radiodurans*.

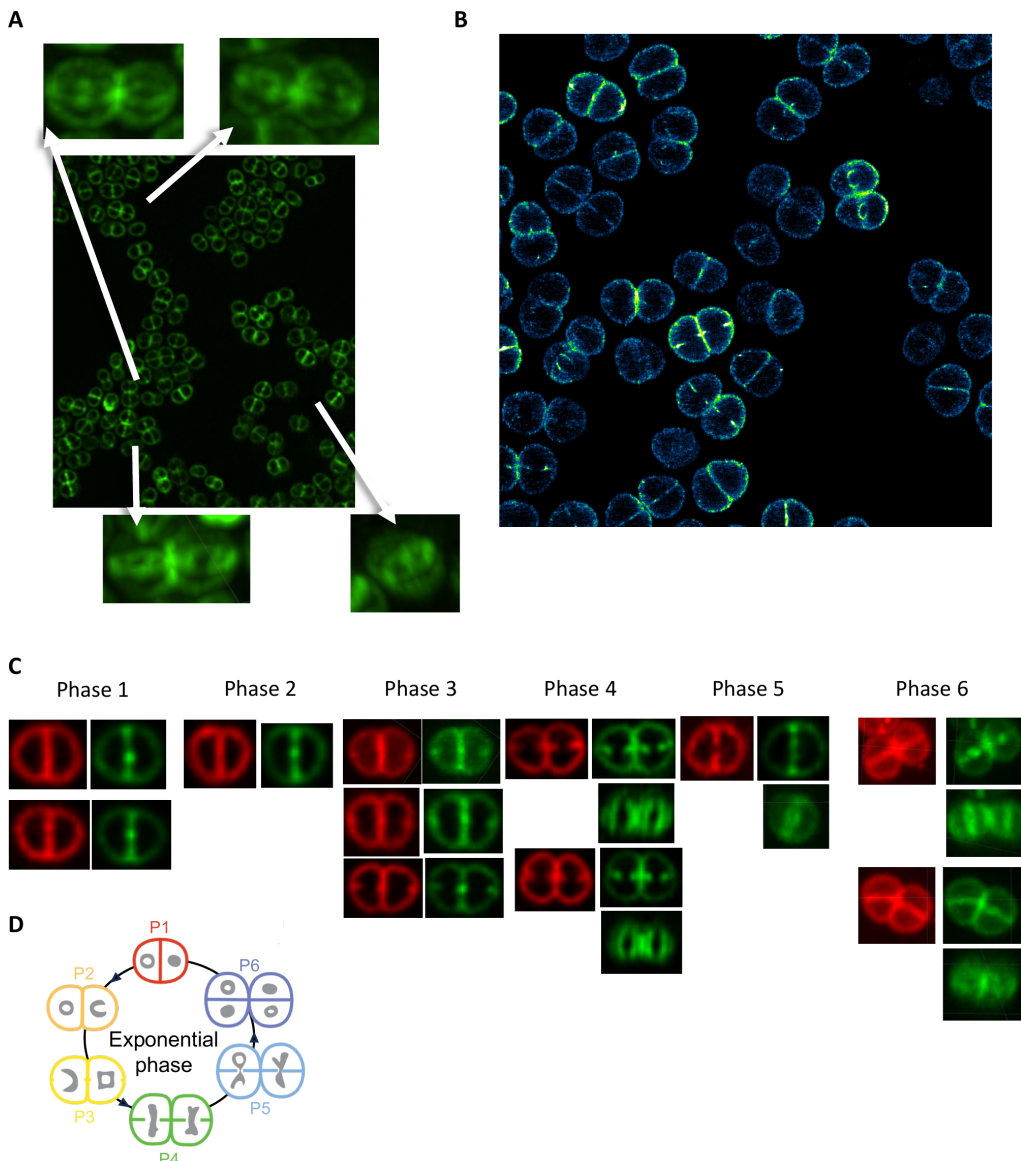


**FIGURE 4.12: PG-labelled *D. radiodurans*.** Examples of images of PG-labelled growing *D. radiodurans* viewed by confocal (A) and dSTORM (B) microscopy. (C) Dual labelling of PG (green) and membrane (Nile Red) layers as a function of the phases of the cell cycle. (D) Schematic diagram of the different phases of the *D. radiodurans* cell cycle starting in phase 1 (P1) as a diad and ending in phase 6 (P6) in the form of a tetrad. The septation process takes place from phases 3 to 6.

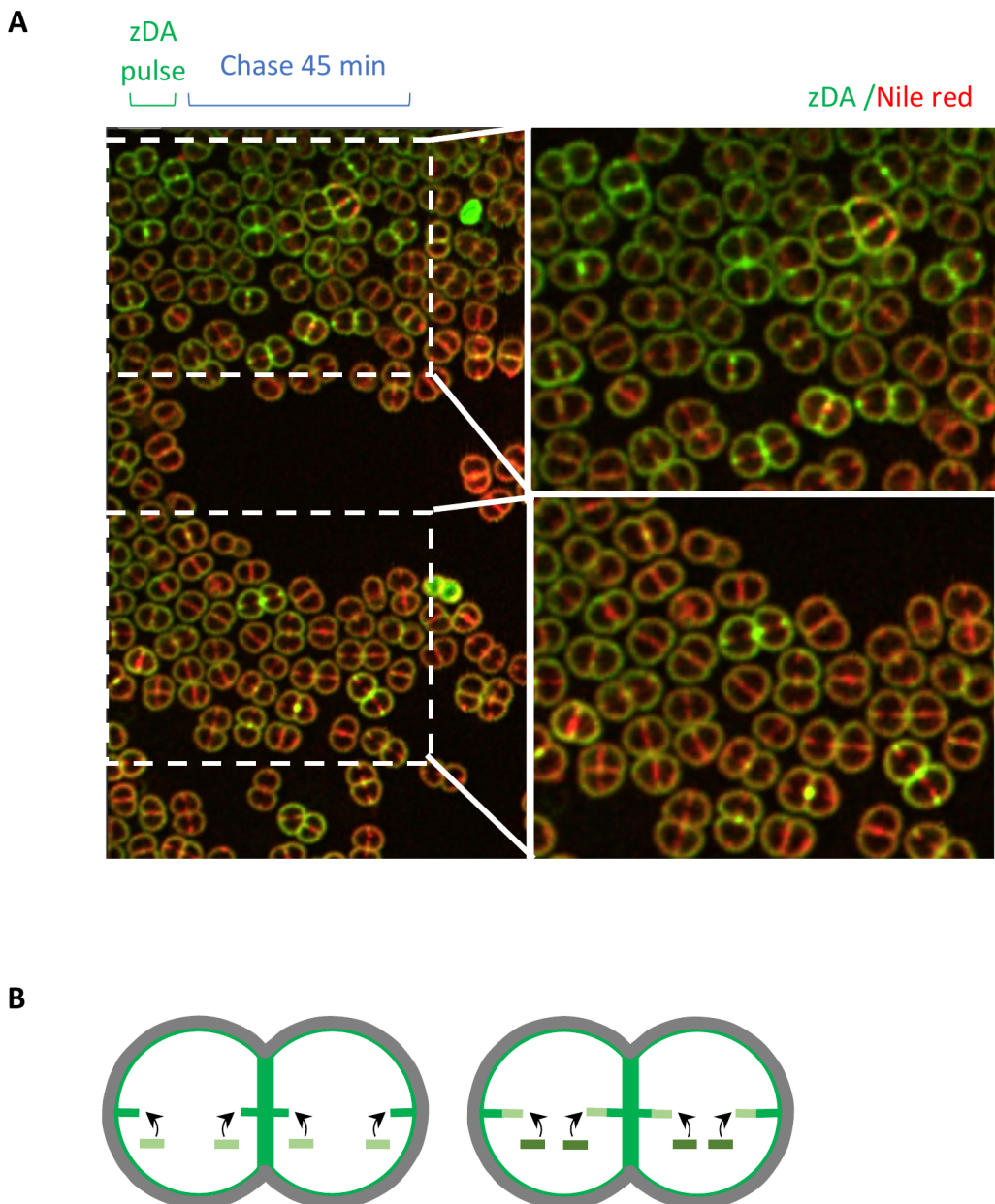


**FIGURE 4.13:** Two-color labelled chase experiment. (A) Examples of two-color confocal microscopy images of PG- and Nile Red-labelled *D. radiodurans* after a 45 min chase experiment. PG labelling in green and membrane labelling in red. (B) Diagram illustrating the stepwise synthesis of PG at the tip of the growing septa to progressively extend the septa until they are sufficiently close to fuse.

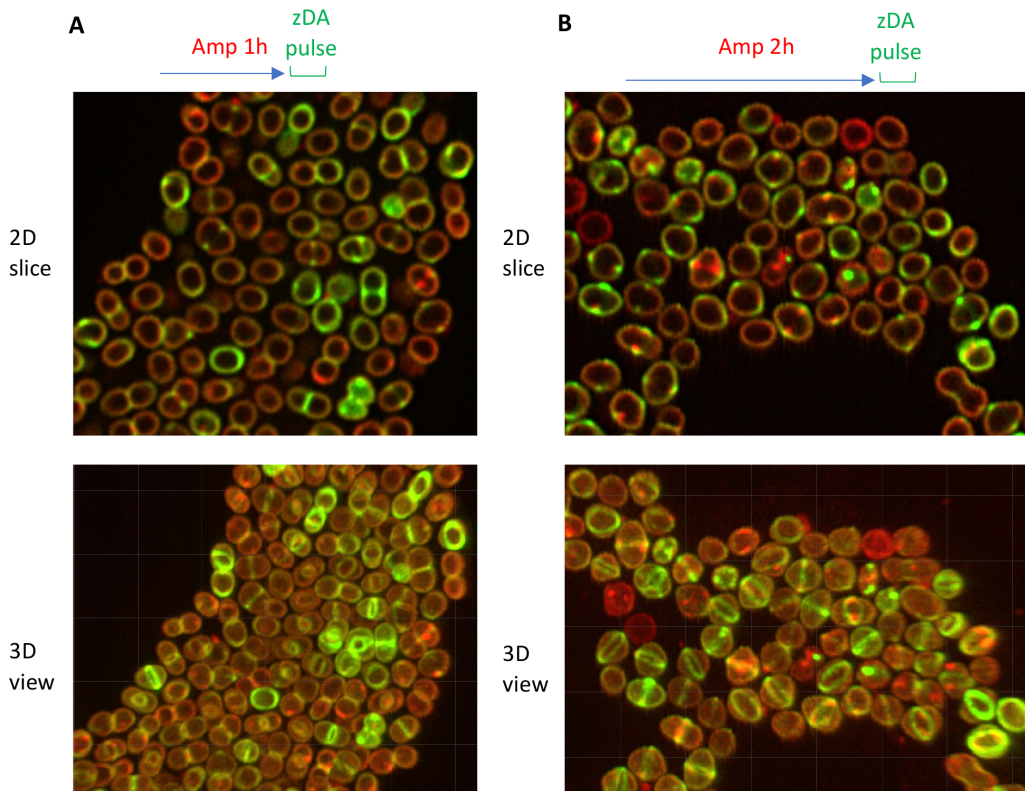


**FIGURE 4.14:** Two-color labelled chase experiment with Ampicillin. Examples of two-color confocal microscopy images of PG- and Nile Red-labelled *D. radiodurans* after growth in the presence of 1 µg/ml Ampicillin for 1h (A) or 2h (B). PG labelling in green and membrane labelling in red. Top panels: 2D slices through the confocal images. Lower panels: 3D views of the same regions.

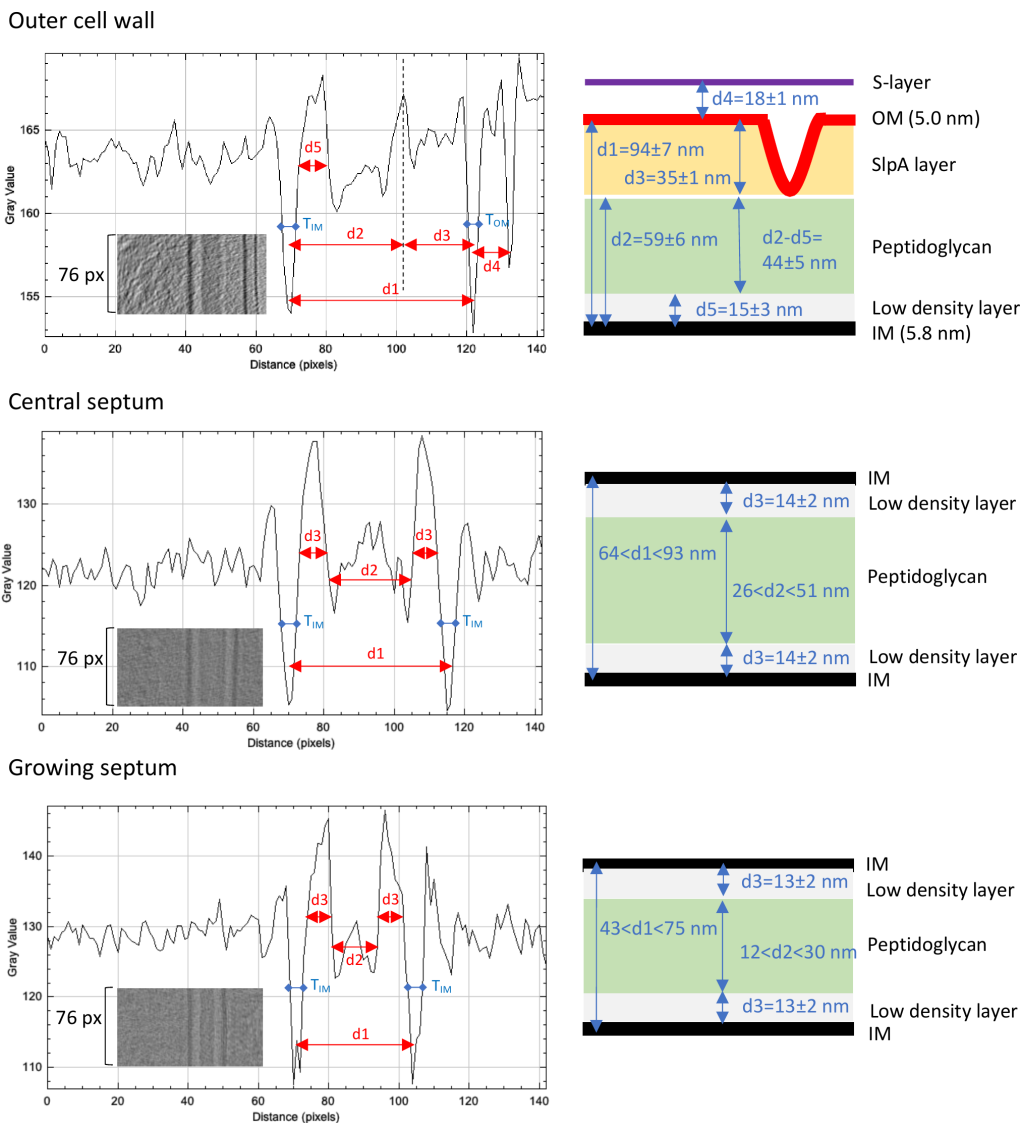


**FIGURE 4.15: 1D density profiles of walls and septa.** Typical 1D density profiles obtained for 76-pixel sections of 2D projections of straightened cell walls (illustrated as insets) from the outer cell envelope (top), central septum (middle) and the growing septum (bottom). Various measurements were made to determine the average thicknesses of the different layers composing these distinct cell walls. Distances between the middle of the IM, OM, central white line and the S-layer were measured as shown by the red arrows. Additionally, the thickness of the inner (TIM) and outer (TOM) were measured at mid-peak height as shown with the blue lines. The thickness of the periplasmic space (d<sub>5</sub> in top panel and d<sub>3</sub>/d<sub>3'</sub> in lower panels) was measured at the base of this positive peak.

# Chapter 5

## Bacterial chromatin, FtsZ, and other projects

My PhD project was originally focused on unraveling the mechanism of action of the nucleoid-associated protein HU, and its role in chromatin compaction and nucleoid dynamics in *D. radiodurans*. The structural study of FtsZ — both in STA and SPA — emerged from our exploration of the nucleoid and cell division processes of *D. radiodurans* in cryo-ET as part of the septation paper ([Chapter 4: \*D. radiodurans\*: cell division and septation](#)) Along the way, I contributed to a few other projects and developed several tools. This chapter presents these projects and the tools and scripts worthy of mention in this manuscript.

### Contents

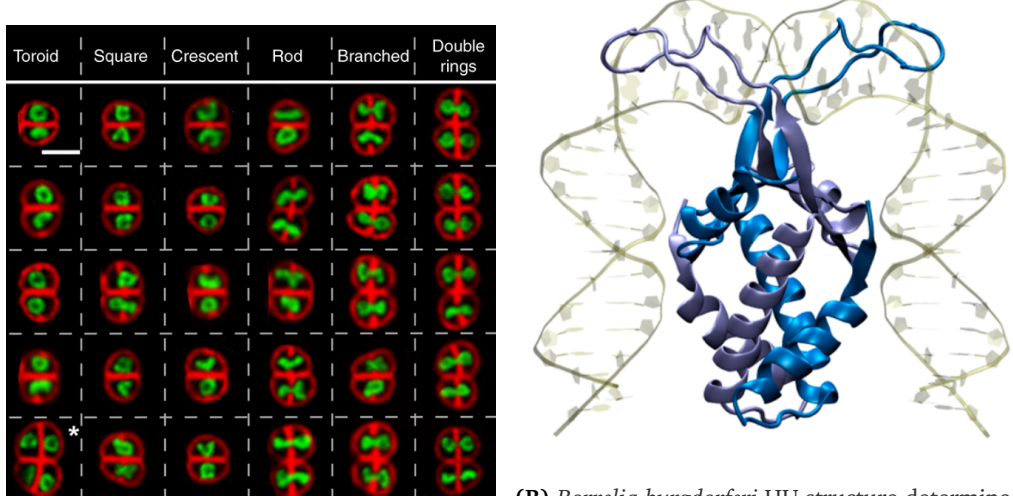
Contents .....	110
5.1 Bacterial chromatin and HU .....	111
5.2 FtsZ function and structure .....	116
State of the art .....	116
Structural study by SPA .....	118
Graphene and streptavidin-coated grids .....	120
Tilted data collection .....	121

Addition of detergent.....	123
Tomography and STA .....	123
Subtomogram averaging .....	126
5.3 Tools and scripts .....	128
waretomo.....	128
emscan .....	128
Design and workflow .....	129
Potential improvements .....	130
Other napari tools .....	130
cs2star .....	131
stemia .....	131
cspplot.....	131
create_mask .....	131
project_profiles .....	131
warp .....	132
generate_tilt_angles .....	132

## 5.1 Bacterial chromatin and HU

Initially the main project of my PhD, the study of bacterial chromatin compaction by cryo-EM and cryo-ET is an ongoing collaborative project between the MICA group and the GenOM team. It builds upon previous fluorescence imaging on *D. radiodurans* nucleoids done by the GenOM team and more recent cryo-EM and cryo-ET data collected and analyzed by the MICA group.

The main protein of interest is HU, a nucleoid-associated protein (NAP) present in most bacteria (including *E. coli* and *D. radiodurans*) which is known to be a key player in chromatin compaction and nucleoid morphology throughout the cell cycle. The structure of dimeric HU from various bacterial species has been solved in either its apo- or DNA-bound forms ([Figure 5.1](#)). HU is thought to have a histone-like bending function — with molecular dynamics simulations supporting the evidence to this binding mode<sup>[165](#)</sup> — but it was also observed forming stacks of dimers that lay parallel to the



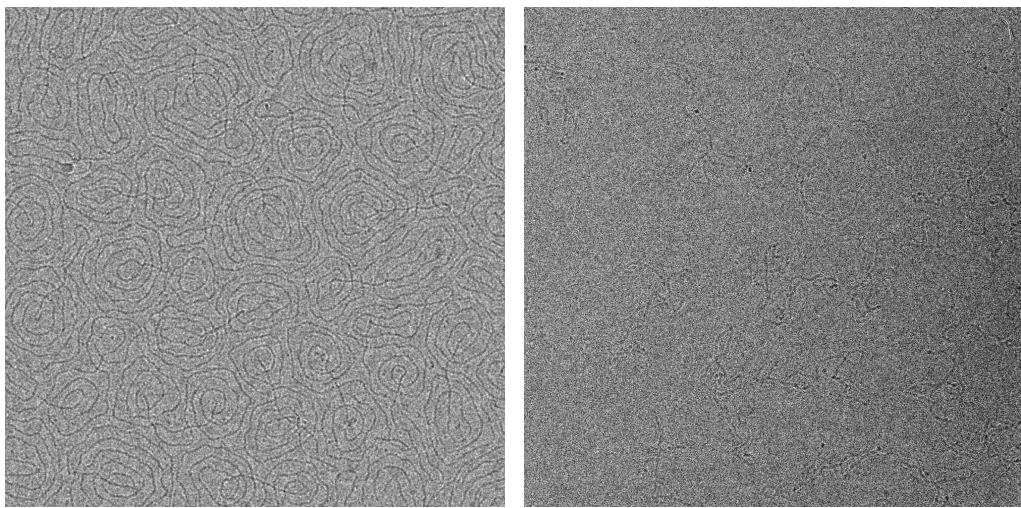
(A) *D. radiodurans* heterogeneous and dynamic nucleoid morphology shows variations throughout the cell cycle. Figure taken from Floc'h et al.<sup>129</sup>.

(B) *Borrelia burgdorferi* HU structure determined by X-ray crystallography. Its DNA-kinking histone-like behavior was replicated by molecular dynamics simulations. Figure taken from Hognon et al.<sup>165</sup>.

**FIGURE 5.1: *D. radiodurans* nucleoids and HU structure.** (a) Nucleoid compaction and morphology in *D. radiodurans* is complex and dynamic, with HU being one of the major drivers of chromatin compaction. (b) HU is thought to have a histone-like behaviour, bending the DNA to form a tight kink.

DNA duplex, suggesting the possibility of multiple modes of interaction between HU dimers and the DNA<sup>166</sup>. Such drastically different modes may explain the heterogeneous highly dynamic nature of the *D. radiodurans* nucleoids despite the relatively low number of players involved — mostly driven by HU and a DNA-gyrase.

To begin investigating DrHU in complex with the DNA, my supervisors collected single particle cryo-EM data of an *in vitro* preparation of plasmid DNA and HU, in order to observe the interaction in a free aqueous environment. The bacterial genomic DNA is large, circular and supercoiled; where previous structural studies used short DNA segments, we opted for a circular dsDNA plasmid as it would be a more appropriate stand-in that would allow us to evaluate how circularity, supercoiling and DNA topology affect HU binding and assembly on DNA. HU and pUC19 plasmid DNA were mixed at different ratios, and within a small range of relative concentration (~100 HU/2686 bp plasmid) intriguing spirals (**Figure 5.2**) were formed by the



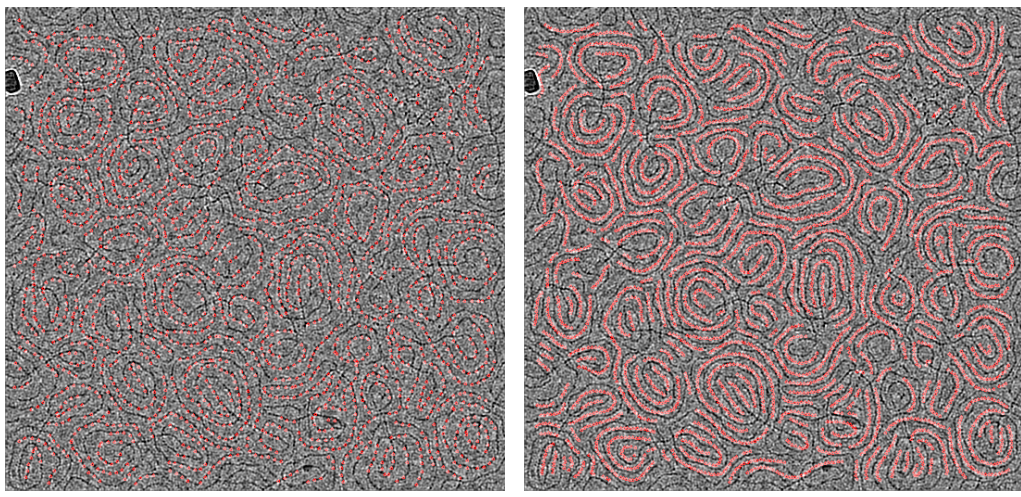
(A) DNA spirals formed in presence of HU.      (B) In absence of HU no spirals are formed.

**FIGURE 5.2: HU-induced DNA spirals.** Spiral formations of supercoiled plasmid DNA are formed in presence of HU only at specific concentration ranges.

DNA. Notably, these spirals were formed by supercoiled DNA only, but not by relaxed or linearized plasmid, and were never observed in the absence of HU. Our original idea based on these images was that HU would form tetramers and bind between two neighbouring turns of the DNA spirals to hold them together.

The very small molecular weight of HU (~25 kDa in its dimeric form) meant that picking and processing these particles (even in the expected dimeric or tetrameric forms) would be practically impossible in cryo-EM (see [Figure 2.4](#) for the theoretical limits). However, due to the relatively high concentration of HU — ~100 HU/plasmid corresponds to approximately 1 HU for every 26bp — the DNA should be densely decorated by HU, unless the protein distribution on the grid is not uniform or big aggregates are forming. It should therefore be possible to work around the particle size limitation by using the supporting geometry of the DNA filament to do the picking and guide refinement.

With this in mind, we devised two picking strategies: a DNA-aligned one ([Figure 5.3A](#)), from which we might be able to isolate picks where HU is decorating the DNA on the side, and one positioned between two DNA filaments ([Figure 5.3B](#)), where we might be able to see tetramer of HU,



(A) Particle picks aligned on the DNA.

(B) Particle picks between DNA filaments.

**FIGURE 5.3: Filament picking strategies for HU.** Filament picking is controlled via several parameters, among which an optional template. We generated two different templates (by doing some manual picking and simple classification): one that is aligned with the DNA filament, and one centered between two DNA filaments. Particles picked using the CryoSPARC<sup>22</sup> filament picker.

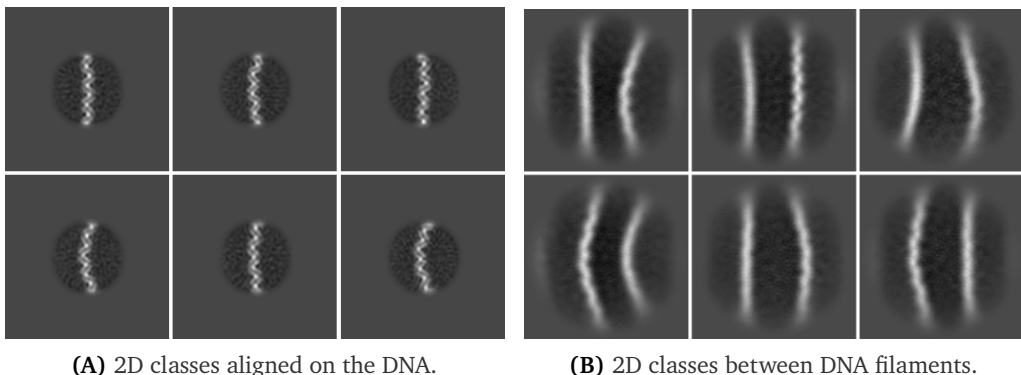
hypothesized to form a bridge between DNA filaments based on previous biochemical studies by the GenOM team.

With these picks and a few rounds of 2D classification and cleaning, we were able to obtain 2D classes in which DNA features were clearly visible; unfortunately, no decoration on the DNA was visible ([Figure 5.4](#)).

We attempted also to pick particles manually or using topaz, focusing on each occurrence of a small “blob” of HU-compatible dimensions appearing next to the DNA ([Figure 5.5](#)).

In all these cases, when doing 3D reconstruction, we attempted to apply tight masking around the filament or next to it, or to restrict the refinement shifts to allow the DNA to help with initial alignment without hindering the pose refinement. Unfortunately, in none of these cases we were able to successfully identify HU in our dataset, likely due to the small size of HU, but also the heterogeneous and dynamic nature of the HU-DNA complex.

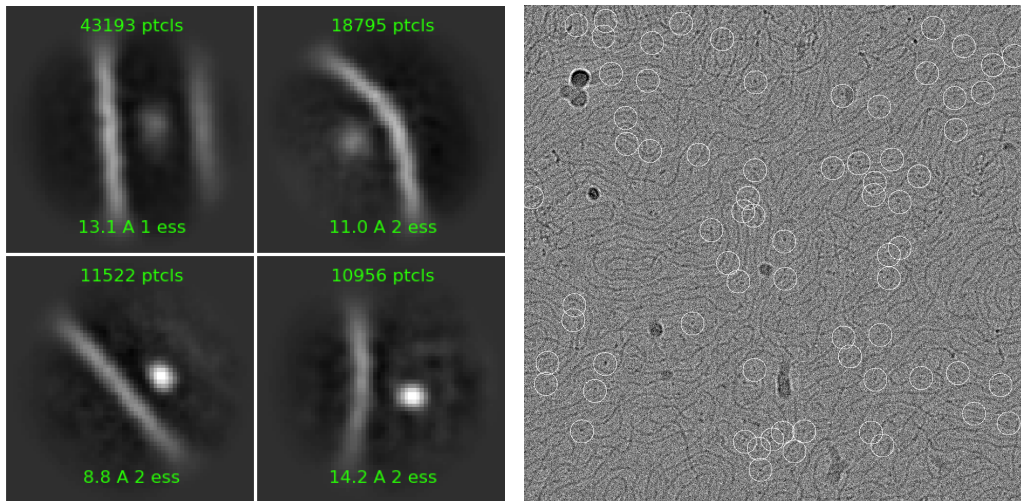
Given the difficulty of picking HU and refining further, we concluded that we needed to devise a new sample preparation and/or data collection that was designed to help with picking and refinement. In the interest of



(A) 2D classes aligned on the DNA.

(B) 2D classes between DNA filaments.

**FIGURE 5.4: 2D classes from filament picking.** Particle picks aligned on the DNA show high resolution detail in the 2D classes, where the DNA double strand is clearly visible. Picks centered between two filaments did not reach as high resolutions, likely due to how impactful the relative spacing and curvature of the two DNA filaments is on driving the classification procedure.



(A) 2D classes from Topaz picking.

(B) Particle picks from Topaz.

**FIGURE 5.5: 2D classification from Topaz picking.** Representative classification results (left) from Topaz picks (right) centered on “blobs” next to the DNA.

time — and to focus on my primary goal of software development — the project was temporarily shelved to be later picked up by others in the group ([Section 7.4: Chromatin and HU](#)).

## 5.2 FtsZ function and structure

To better understand the role of FtsZ in the septation of *D. radiodurans*, we investigated its structure and superstructure using both single particle cryo-EM and *in situ* cryo-ET. This work is ongoing and not yet consolidated into a manuscript for publication. Sample preparation and screening was performed by my supervisors Irina Gutsche and Joanna Timmins, while data collections were done partly by Irina, and partly commissioned to external facilities. Data processing on the single particle and tomography data, and software tool development were performed by me.

### State of the art

FtsZ is an extremely well conserved prokaryotic tubulin homologue, known to form ring-like structures (the Z-ring) at the septation site in most bacteria. It polymerizes in a GTP-dependent fashion to form filaments and bundles, anchoring to the membrane via its partner FtsA, and interacting with several other partners in the cytokinesis and peptidoglycan (PG) synthesis machinery<sup>159,160</sup>.

Based on crystal structures, filaments have been shown to form through head-to-tail stacking of monomers<sup>159,160,167</sup>. However, there is no structural information regarding the flexible C-terminal region, which is responsible for regulating the FtsZ activity and interaction with its cellular partners, including FtsA. It's also unclear how multiple filaments may assemble to form bundles at the structural level and even less so *in vivo*. Thus — while its key role in cell division is undisputed — the exact mechanism and function of FtsZ are still unclear. There is currently no consensus model that fully explains the function and mode of action of FtsZ in the division process in bacteria, as the current evidence is inconclusive, sometimes presenting significant variations between species — likely ascribable to different shapes or membrane compositions between bacteria<sup>159,160</sup>.

Some studies have shown that FtsZ presents mechanical functions that may drive the septation process. *T. maritima* FtsZ+FtsA expressed in

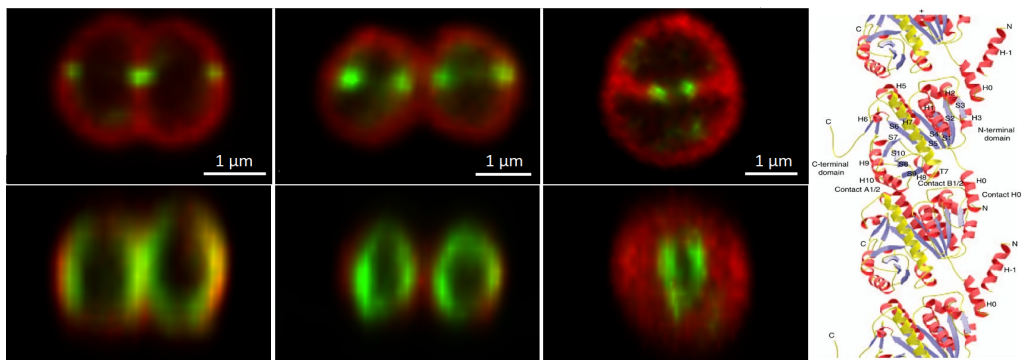


**FIGURE 5.6:** FtsZ forms a ring *in vivo* and filaments *in vitro*. During cell division, FtsZ is known to localize on a ring located at the tips of the septa, as can be seen in these images of *D. radiodurans* (left, figure adapted from [Figure 4.6](#)). Many structural studies were done on FtsZ, identifying the formation of protofilament via head-to-tail stacking (right, figure adapted from Oliva et al. <sup>167</sup>).

liposomes was shown to form coil-like structures, which can constrict the membrane via a “filament sliding” mechanism, creating a partial septum <sup>138</sup>. In *C. crescentus*, FtsZ may form short, loosely bundled filaments, which may drive constriction via an “iterative pinching” mechanism where repeated rounds of phosphorylation lightly bend the filament, thus slowly pinching the membrane <sup>137</sup>.

Other publications investigated the recruitment and signalling role of FtsZ for downstream machinery such as PG synthesis. FtsZ was shown to undergo plus-end polymerization and minus-end depolymerization, in a GTP-regulated process typical of cytoskeletal proteins called treadmilling <sup>168</sup>. In *B. subtilis*, this treadmilling is required to drive the movement along the septum of the PG synthesis centers <sup>169</sup>. A “diffusion-and-capture” model was proposed, where the FtsZ ring performs a recruitment role by engaging in weak transient interactions with downstream machinery for PG synthesis <sup>170</sup>. However, in *S. aureus*, cytokinesis may actually occur in two separate steps: a slow, FtsZ-driven, treadmilling-dependent step which causes initial invagination, followed by a faster step where PG synthesis is the driving force for septation <sup>171</sup>.

While FtsZ ring formation and PG synthesis are clearly linked, their precise interaction may differ between bacteria. In *E. coli*, GTP regulates

FtsZ treadmilling, which in turn controls the movement of the synthesis machinery<sup>172</sup>. However, it does not appear to affect the rate of PG synthesis, as opposed to what happens in *B. subtilis*, which suggest that the presence or absence of an outer membrane may change PG synthesis machinery regulation<sup>172</sup>. Indeed, in *E. coli*, some additional proteins may help with a timely invagination of the outer membrane, although they are not needed for septation to occur<sup>173</sup>. This is intriguing for *D. radiodurans* which, despite staining gram-positive, presents an outer membrane.

The disordered C-terminal domain of FtsZ was found to be necessary both for the anchorage to the membrane via FtsA, and to regulate oligomerization as well as bundling with neighboring filaments<sup>159</sup>.

Collectively, the literature hints that FtsZ treadmilling is likely not the only factor that controls the dynamics of FtsZ and the Z-ring, and that variations across species may be explained by different divergent mechanisms, or some other underlying behavior not yet discovered<sup>159</sup>.

## Structural study by SPA

We began our investigation of the structure of DrFtsZ filaments by doing SPA on *in vitro* samples prepared from purified monomeric FtsZ from *D. radiodurans*. Since successful polymerization is highly sensitive to FtsZ concentration, temperature, concentration of GTP (or other nucleotide), and elongation time, my supervisors screened a variety of conditions. The selected cryo-EM preparation resulted in FtsZ filaments long enough to allow filament picking and helical reconstruction, while avoiding an excess of filament bundles which make picking and refinement more difficult (**Figure 5.7**).

We used CryoSPARC<sup>22</sup> for filament picking, which gave us a large amount of particles (>4M) to classify and clean up from spurious picks. After cleaning, we ended up with about 2M particles, and very uniform classes with little variation (**Figure 5.8**). This is a typical symptom of strong preferential orientation due to the air-water interface (**Section 1.2: Preferential orientation**), leading to a very limited range of views in the

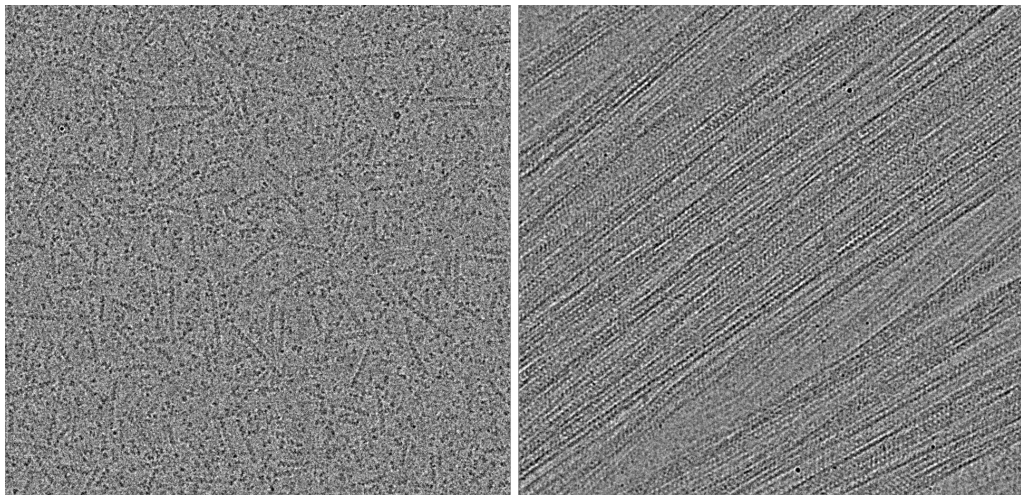


**FIGURE 5.7: Micrographs of FtsZ filaments.** Micrographs containing FtsZ filaments. When filaments are individual and well separated (left) they are ideal for picking and refinement. In some cases, FtsZ filaments form bundles (right) which are harder to pick, refine and classify due to the overlapping particles.

particle projections. Although we saw hints of different views in the bundled filaments, they proved impossible to disentangle enough to obtain well-resolved classes.

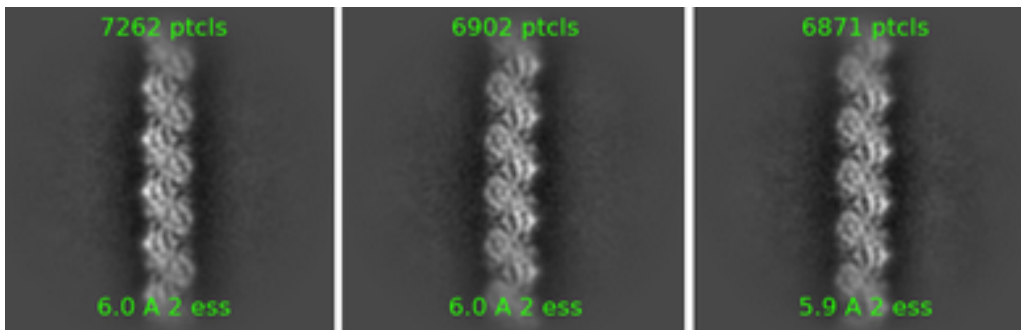


**FIGURE 5.8: FtsZ filament: 2D classes.** Classification results from particles with strong preferential orientation. All classes show very similar views of the FtsZ filaments, with minor variation in the out-of-plane angle.

Given the strong preferential orientation, it's unsurprising that 3D reconstructions from these particles showed very strong resolution anisotropy (while reporting  $\sim 4 \text{ \AA}$  global resolution), so much so that we couldn't

convincingly fit the monomeric model in the map ([Figure 5.9](#)).

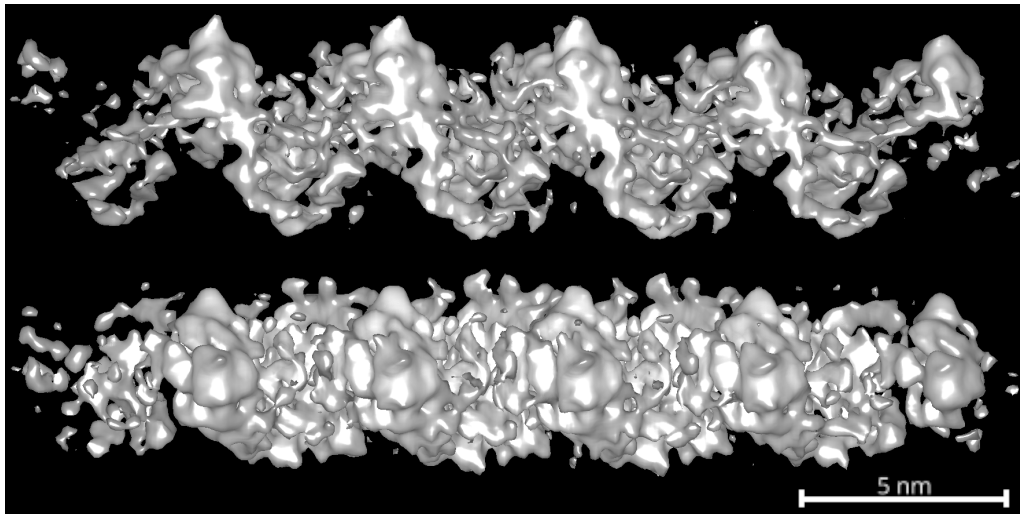


**FIGURE 5.9:** FtsZ filament: anisotropic map. FtsZ filament map affected by preferential orientation, viewed from the same direction as most 2D classes (top) and rotated by 90° (bottom) to highlight the streaking artifacts due to anisotropic orientation sampling.

The best map currently available of FtsZ filaments (from *Klebsiella pneumoniae*) also suffered from similar issues, despite the high reported resolution (~3 Å)<sup>174</sup>.

We attempted to address the issue of preferential orientation in two different ways: collecting a tilted dataset of the same samples, and preparing a new sample with methods that combat air-water interface effects.

### Graphene and streptavidin-coated grids

We attempted to address the preferential orientation problem by using functionalized graphene grids<sup>12</sup>, and streptavidin-coated affinity support grids<sup>13,14</sup>. While these approaches have been shown to work, we struggled to obtain usable grids; at the very end of my thesis, the sample prepared with the addition of detergent showed promising results, so we moved forward with it instead.

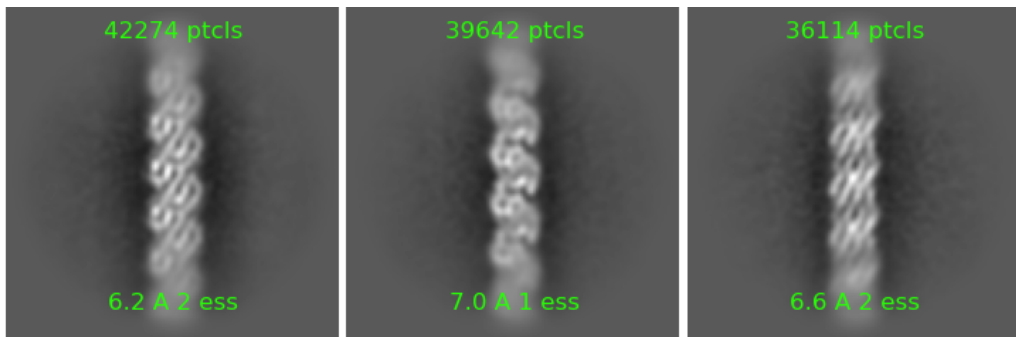


**FIGURE 5.10:** FtsZ tilted dataset: 2D classes. Classification results from the tilted dataset. Differently from the untilted classes, particles successfully classified into distinct views of the filament.

### Tilted data collection

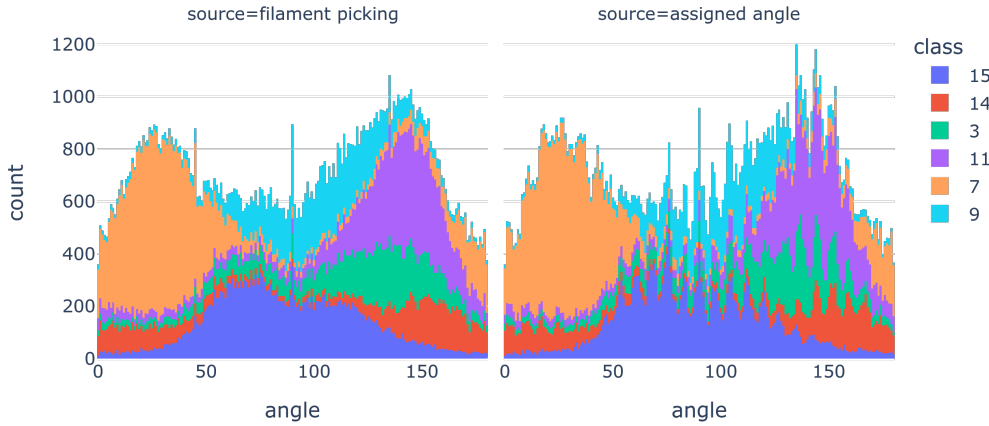
We prepared the sample in the same way as originally, but this time the data collection was done with the grid at a  $35^\circ$  tilt. Following the same workflow as with the untilted dataset, we then picked, classified and selected particles, obtaining a new set of class averages (Figure 5.10). These classes looked immediately more promising than the ones from the untilted datasets, showing multiple views from the first round of classification, even in isolated filaments.

Despite the better view distribution of 2D classes, our 3D reconstructions had similar anisotropy issues as the untilted data, and we seemed to hit a resolution plateau. Assuming a uniform distribution of in-plane angles of the filaments (which we observed in the original dataset), a single, relatively high-tilt dataset should cover a higher portion of 3D Fourier space during backprojection and thus significantly improve map isotropy<sup>175</sup>.

With preferentially oriented filaments collected at a fixed tilt angle, there should be a strong correlation between in-plane angle (easily identifiable from the micrograph) and the projection view (which is identified by classification). Indeed, this is what we see when plotting the in-plane angle distribution per class from the filament picking; however, in the angle distribution after 3D helical reconstruction, we no longer saw any correlation, suggesting that the refinement procedure was unable to properly assign in-



(A) Original in-plane angle versus 2D class plot. On the left, a correlation is clear between the filament picking in-plane angle and class; on the right, correlation appears to be lost.



(B) Updated angle vs class plot. The correlation is now evidently retained after 3D helical refinement.

**FIGURE 5.11: Correlation between in-plane angle and 2D class.** In-plane angle distribution for a cleaned subset of the FtsZ particles, colored by class. The original (wrong) plot (top right), showed no correlation between angles and class; the updated plot (bottom right) shows similar correlation to that found in the filament picking poses.

and out-of-plane angles to each particle ([Figure 5.11A](#)).

Unfortunately, we recently discovered we made a mistake in our calculations — likely due to the (undocumented) angle conversions from CryoSPARC data to Relion Euler angles ([Section 6.1: Metadata wrangling](#)) — which, once fixed, revealed that correlation was still present and angular assignment was probably not the source of our resolution plateau ([Figure 5.11B](#)).

Based on the (wrong) assumption that angles were not properly assigned,

we concluded that in this specific case the 3D reconstruction routines of both Relion<sup>28</sup> and CryoSPARC<sup>22</sup> were struggling with assigning Euler angles, resulting in practically random orientations.

Therefore, to impose more constraints on the refinement based on the expected angle correlations, we calculated the theoretical orientation of each particle based on the in-plane angle (and assuming perfect preferential orientation), which we used to initialize the particle poses ([Section 5.3: generate\\_tilt\\_angles](#)).

Unfortunately — though in hindsight unsurprisingly — this approach did not improve our reconstruction, and we learned that CryoSPARC does not provide fine control over angle priors and search patterns, and Relion’s parameters for angle refinement are tricky to control and may easily lead to orientations being stuck in local minima.

### Addition of detergent

Detergent has long been used as a way to address preferential orientation and aggregation of proteins in the sample. In our case, while it did not affect the orientation problem, it allowed FtsZ to polymerize into longer filaments without creating large bundles ([Figure 5.12](#)).

The longer filaments and the very small helical twist (estimated at  $<1^\circ$  with the previous samples), should result in different side views of the monomers being visible in the dataset.

Preliminary results indeed showed a higher diversity in class averages, including classes with different views of single filaments ([Figure 5.13A](#)) and classes with two or three filaments potentially interacting side-by-side ([Figure 5.13B](#)).

### Tomography and STA

In parallel to the study of *in vitro* FtsZ filament by SPA, we also investigated the FtsZ *in situ* in the tomograms of *D. radiodurans* lamellae. Some of our findings and speculations about the 3D morphology of FtsZ are included in

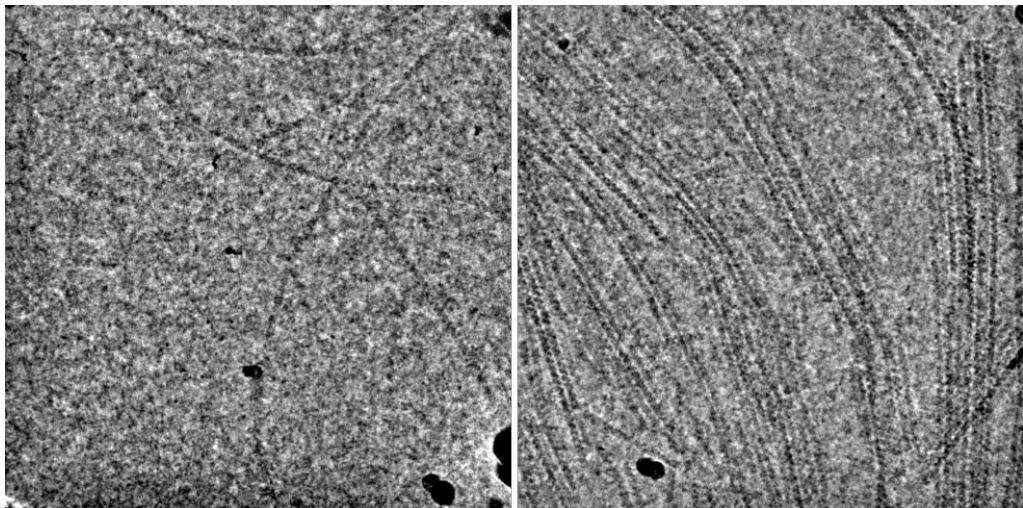
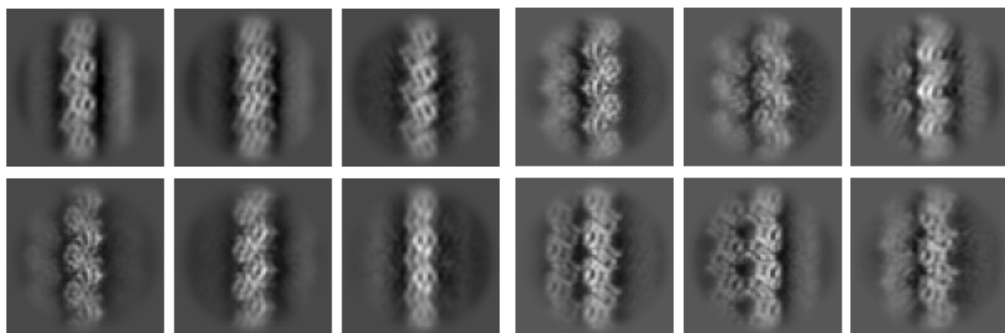


**FIGURE 5.12:** Micrographs of FtsZ with detergent. The addition of detergent allowed the FtsZ filaments to elongate further, without resulting in dense bundles (left). When bundles formed (right), they were often less densely packed than without detergent, opening up the possibility to pick bundled filaments in order to investigate side interactions.



(A) Classes with different views on single FtsZ(B) Classes with multiple interacting FtsZ filaments.

**FIGURE 5.13:** 2D classes of FtsZ with detergent. Classification results from the FtsZ+DDM dataset show a wider range of views than the original dataset. Classes containing bundled filaments also show multiple views, with intriguing hints at side interactions between neighboring filaments.

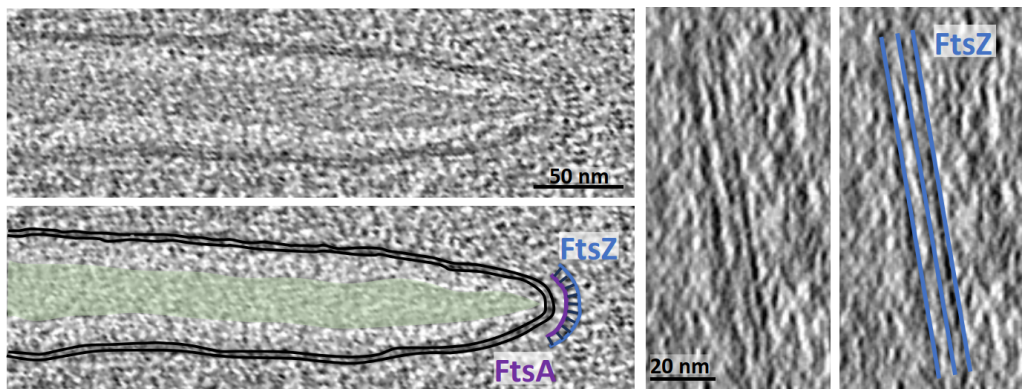
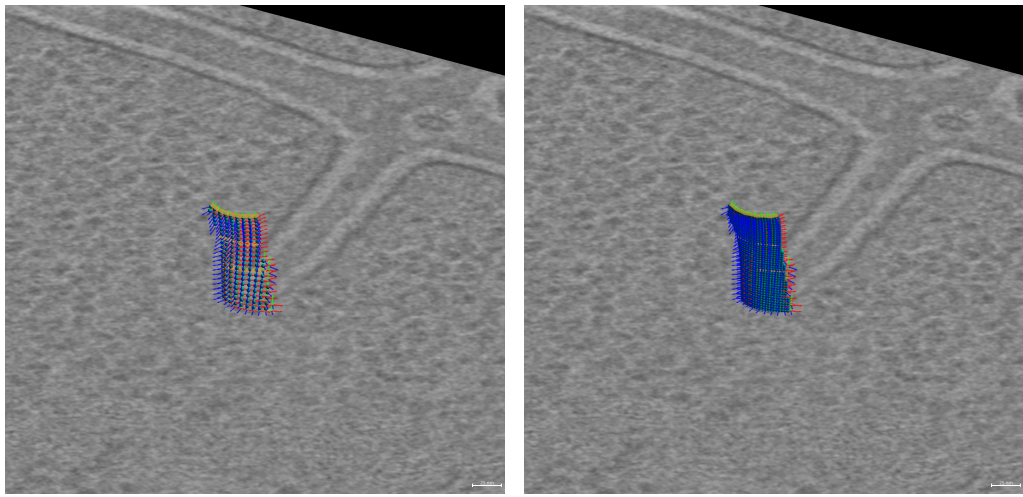


**FIGURE 5.14:** FtsZ: tomogram slices from top and side view. When viewing a cross-section of a tomogram of *D. radiodurans* (left), a double arch separated by a gridded pattern can be seen near the tip of the septa. This is likely a layer of FtsA bridging between the membrane and a layer of FtsZ filaments. The distance of the second arch (FtsZ) from the membrane is  $\sim$ 14 nm, in concordance with the literature. The distance between each line in the gridded pattern (expected to match the filaments) is  $\sim$ 55 Å, similar to the inter-filament distance from other studies. A side view of the septal tip (right) shows that the double-arch is an elongated structure, matching the expectation of a bundle of filaments forming a septation ring. Figure adapted from [Figure 4.4](#).

the *D. radiodurans* manuscript ([Section 4.3: FtsZ is present at the tips of septa](#) and [Section 4.4: Discussion](#)).

Our observations on the reconstructed tomograms matched those by Sexton et al.<sup>110</sup>, who also used tomography to look into *D. radiodurans* and identified FtsZ and FtsA forming filaments just inside the inner membrane of the septal tips ([Figure 5.14](#)).

The spacing between supposed FtsZ filaments ( $\sim$ 55 Å) is generally consistent with crystal structures and SPA studies on FtsZ filaments<sup>160</sup>. The distance between the membrane and the FtsZ filaments in the outer arch ( $\sim$ 14 nm) is consistent with the expected  $\sim$ 13-16 nm found in literature<sup>160</sup>. However, the width of the bundle appears to be smaller than the previously reported 80-100 nm<sup>160</sup>, typically no wider than around 50-60 nm; this might be caused by differences in the thickness of the septa or modes of septation between different bacteria.



(A) Particle picks at 50 Å spacing.

(B) Particle picks at 25 Å spacing.

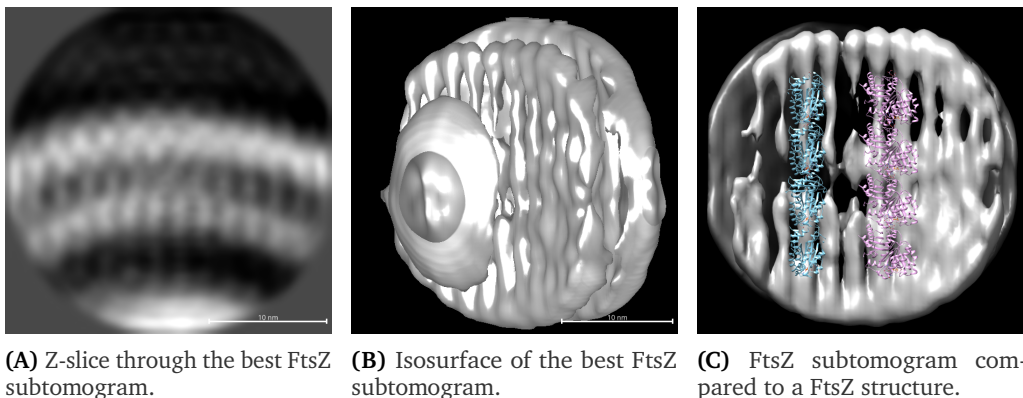
**FIGURE 5.15:** Surface-based FtsZ particle picks for STA. Particle picks on FtsZ at the tip of the septa in *D. radiodurans* tomograms, generated with surface-based picking in blik<sup>176,177</sup> at two different inter-particle spacings.

### Subtomogram averaging

While it is clear that FtsZ and FtsA are forming filaments and bundles *in vitro*, and that they localize to the Z-ring in a bundle-like fashion, the details of this superstructural assembly are unknown. To get a higher resolution view of this complex *in situ*, we performed STA on particles picked from the FtsZ arches at the tips of the septa ([Figure 5.14](#)).

Given the apparent regularity of the bundles (whose morphology appears unchanged across their length), we used blik’s surface picking tool<sup>72,176</sup>, which allows us to distribute regularly spaced particles on the sheet-like FtsZ bundles. The inter-particle distance was chosen to be based on the spacing in the regular comb-like pattern along the FtsZ arches. Several different sets of particles were thus generated, with two showing more promising results: with inter-particle distance matching the visible pattern ( $\sim 50 \text{ \AA}$ ), and twice oversampled ( $\sim 25 \text{ \AA}$ ) ([Figure 5.15](#)).

Subtomograms were reconstructed in Warp<sup>23</sup> using these particle picks, at different resolutions and with varying box sizes. Using Relion<sup>28,62,74</sup>, we performed subtomogram averaging and 3D classification to refine the positions and obtain a 3D map of the particles. Due to the low magnification



(A) Z-slice through the best FtsZ subtomogram. (B) Isosurface of the best FtsZ subtomogram. (C) FtsZ subtomogram compared to a FtsZ structure.

**FIGURE 5.16:** FtsZ STA preliminary results. Subtomogram averaging results of the particle picks on FtsZ at the tip of the septa in *D. radiodurans*. The grid-like pattern visible in the tomogram slices is captured by the subtomograms, but it's likely to be partly artifactual, as the spacing between filaments is too low. On the right, FtsZ filament crystal structures fitted to the map in two different orientations show the mismatch in sizes.

of the dataset (Nyquist  $\approx 8.8 \text{ \AA}$ ), Relion was in most cases struggling to assign orientations. The only refinement that resulted in consistent orientations and a reasonable map was with particles picked at 50  $\text{\AA}$  spacing, and subtomograms reconstructed at the highest resolution (4.346  $\text{\AA}/\text{px}$ ) and with a large box size of 64 pixels, corresponding to  $\sim 28 \text{ nm}$  (**Figure 5.16**). Even still, this map is likely to contain artifacts due to misalignment of the repeating filament patterns, as evidenced by the too-small inter-filament distance ( $\sim 21.1 \text{ \AA}$ ) (**Figure 5.16C**).

It's worth noting that, due to the nature of the division cycle of *D. radiodurans*, the bacterium is generally found as a tetrad laying flat on the grid, which leads to a preferential orientation of the septa (and therefore the FtsZ filaments) along the Z axis on the tomograms. Due to the missing wedge (**Section 2.4: Tomogram Reconstruction**), along which the filaments are aligned, the information is blurred along the FtsZ filament axis, limiting for example the ability to distinguish individual FtsZ monomers.

This project has now been picked up by other members of the group, and by using existing and new datasets it's already showing promising improvements over this work, on both the single particle (**Section 7.4: FtsZ SPA**) and the subtomogram averaging sides (**Section 7.4: FtsZ STA**).

## 5.3 Tools and scripts

### waretomo

As most cryo-ET users, over time I kept tweaking and improving my processing pipeline. At present, it consists of three main elements: Warp<sup>23</sup> for preprocessing and tomogram and subtomogram reconstruction, AreTomo<sup>61</sup> for tilt series alignment, and Relion<sup>28,62,74</sup> for STA.

To facilitate batch processing and remove most needs for manual intervention (and potential points of failure), I developed an automated tool which connects Warp to AreTomo: `waretomo`<sup>101</sup>.

Specifically, `waretomo`:

1. automates parsing `.mdoc` files to provide appropriate inputs to AreTomo
2. ensures that tilts skipped in Warp are properly handled
3. adjusts tilt angles in Warp based the output of AreTomo to untilt tilted samples (such as lamellae)
4. optionally reconstructs preliminary tomograms with AreTomo and denoises them with Topaz<sup>26</sup>

When possible, each step is performed in parallel (and on GPUs) to maximize resource usage and minimize idle time. While this tool is available and open-source, it's not yet publication-ready and still in alpha, so bugs are expected.

### emscan

In cell-extract cryo-EM<sup>32,33</sup>, a dataset may contain a large variety of proteins and complexes, many of which unknown. In these non-purified datasets, automating parts of the selection and protein identification processes is essential for practical applications such as structural proteomics of a novel organism.

As a contribution to the PhD project of Eymeline Pageot — another PhD student in the MICA group under the co-supervision of Ambroise Desfosses

and Irina Gutche — I developed `emscan`, a napari<sup>78</sup>-based tool that searches the EMDB database<sup>178</sup> for maps whose projections have a high similarity with the input 2D classes.

This allows for example to discard classes from already-solved structures, or to identify 2D classes that potentially belong to different views of a protein whose homologues are present on the EMDB.

### Design and workflow

The challenging part of such a tool is performance: the EMDB is a big database, and performing exhaustive cross-correlation search on all the maps could be prohibitive if not done cleverly. To save on networking, storage, and computation, `emscan` keeps an up-to-date local version of the EMDB database but, instead of storing maps, it stores the FT of map projections at different angles (by default, 150 views per map).

When input 2D classes are provided, their FT is calculated and used to compute the CC value between them and each projection of each map (and their mirror image), including a rotational search (by default with a 2° angular step). This step is the bulk of the work, and thus heavily optimized: FTs and intermediate calculations are cached and reused as much as possible, and computations are performed on the GPU when available. With this setup, `emscan` can currently process each 2D class in about 2 hours.

The user is then presented with the best scoring matches, displayed in napari side-by-side for visual comparison with the input classes; a few shortcuts allow to quickly navigate to the relative EMDB page, to open a 3D map in a new napari window, or to generate projections for use in template matching. It's also possible to group together the results of multiple classes by averaging their best scores for each projection comparison; this is useful to determine whether different 2D classes are from unrelated proteins or just different views of the same object.

## Potential improvements

While the tool already proved useful for the cell-extract project, there are several potential avenues for improvement, especially for performance — which will be crucial for the future automation plans.

The current CC calculation is a bit limited and not strictly correct (compromises were made for performance), and its speed could be improved with some clever caching tricks<sup>179</sup>. Alternatively, changing the method altogether, for example by using Fourier-Bessel functions<sup>180</sup> or other methods<sup>181</sup>, might improve the performance even more.

No optimization is currently in place to account for symmetrical objects, which are very common and would require much fewer computations if properly treated.

## Other napari tools

During my thesis, napari proved time and time again a powerful library for creating custom interactive visualisation tools. Some smaller napari-based tools and plugins I contributed to that are worthy of mention are:

1. [surforama](#)<sup>100</sup>, a tool to explore cryo-ET membrane annotations inspired by membranorama<sup>93</sup>, fruit of a collaboration with other napari developers and members of the teamtomo community
2. [napari-molecule-viewer](#), a plugin to open PDB and mmCIF files in napari
3. a [Fourier transform playground](#) to interactively explore the relationship between images and their FTs
4. a [Euler angle playground](#) to build an intuition on the various Euler angle conventions and their effects on particle orientations

## cs2star

A small tool, but used widely by our group and others, and later added to SBGrid<sup>182</sup>, cs2star<sup>183</sup> is a small wrapper around the widespread cryosparc2star.py which automates a few tedious manual steps normally needed when converting CryoSPARC<sup>22</sup> projects to Relion<sup>28</sup> ones.

## stemia

Stemia is a collection of command-line tools that I developed for various purposes, but that were either too small or too niche to make sense as standalone packages. Some of the more relevant tools are noted here for reference.

### csplot

An interactive tool to plot any combination of CryoSPARC<sup>22</sup> particle data columns in a few different styles. Since this was developed, CryoSPARC's own live plotting tools reached similar functionality for particles and micrographs.

### create\_mask

A simple tool to create geometric masks, which often solved problems with similar tools available in other software suites. A better and more full-featured version of this is now being developed by others in Teamtomo at ttmask ([Section 7.3: Teamtomo](#)).

### project\_profiles

A very ad hoc tool, but which was instrumental in streamlining and speeding up significantly the calculation of membrane profiles for the septation paper ([Chapter 4: \*D. radiodurans\*: cell division and septation](#)).

**warp**

A collection of tools to work with Warp, such as for spoofing or fixing mdocs, offsetting tilt angles, or preparing data for processing.

**generate\_tilt\_angles**

A tool developed to work on the FtsZ tilted dataset ([Section 5.2: Tilted data collection](#)) which can be used to initialize angle priors for particles in a tilted dataset.

# **Part III**

## **Discussion**

# Chapter 6

## Software in cryo-ET

Due to the rapid growth of cryo-ET, the software ecosystem as a whole is fragmented; conventions are either not established, or appear on a first-come-first-served basis, with little consensus or community discussion. Meanwhile, the most established pipelines use big monolithic applications, developed with streamlined workflows in mind and little attention to code reusability.

### Contents

Contents .....	134
6.1 Monolithic vs modular: an academia paradox .....	134
Metadata wrangling .....	135
6.2 Good software practices and human-in-the-loop .....	136
Interactive visualization .....	137

### 6.1 Monolithic vs modular: an academia paradox

In academia, large publications with splashy headlines can make or break career paths, rewarding speed, competition, and secrecy; unfortunately, this is not conducive to the development of good software practices.

Researchers regularly develop ad hoc solutions, lacking the time and resources to release a maintainable tool, leading to software that can hardly be adapted even to similar problems. These researchers are also typically PhD students that will soon move to a different group, work on different projects, and won't have any more time to dedicate to their old software. It's rarely in their best interest to keep working on software that won't give them any further publications, so there's little incentive to begin development with modularity and maintainability in mind. All this leads to regular wheel-reinventing, and abandonware full of great ideas but hard to reuse in any capacity for future work.

In the rare success stories where software becomes adopted widely enough to achieve long term maintenance, it's usually in the form of inscrutable monolithic applications developed by a single group or person with little community collaboration on the development. There are of course exceptions, but for young researchers it's generally a safer bet to go the "develop and publish" route than the "design and maintain" one; of course, most research developers struggle with this tension, wishing for their work to be reused and improved, but unable to allocate the time and resources required to do so.

## Metadata wrangling

A common symptom of such an ecosystem is that significant time and effort is lost in dealing with metadata when setting up a cryo-ET data processing workflow.

Due to its history, cryo-ET has also inherited many tools and conventions from cryo-EM, even in cases where they had to be stretched thin in order to fit the needs of the new technique. The existing de facto standard is arguably set by Relion, which in recent years has added explicit support for cryo-ET preprocessing and STA, encoding reconstruction and particles metadata in its STAR file format, which was previously only used for single particle analysis<sup>62,74</sup>. Several other formats exist for particle, alignment, and various other parameters and tilt-series metadata (Dynamo tables<sup>60</sup>,

AreTomo alignments<sup>61</sup>, Warp spline grids<sup>23</sup>, etc.), and while some of them can be interchangeable, others are virtually impossible to convert between.

Currently, there are several attempts at intercommunication between software through converters and pipeline managers. Scipion<sup>85</sup> is likely the most effective and prolific, but it fights an uphill battle, integrating wildly different software, languages and approaches that were never built to be collaborate.

## 6.2 Good software practices and human-in-the-loop

These software ecosystem issues are especially problematic for cryo-ET, where custom workflows and unique solutions are routinely required, due the diverse nature of the samples and project goals. Developing custom tools is often unfeasible for researchers new to the technique or who lack the necessary programming skills to delve deep in the code of the existing software. Monolithic software suites offer user-friendly interfaces and automation — some of their stronger selling points — which can often get in the way of custom tool injections and human intervention. On the flip side, tools that are standalone and single-purpose provide the flexibility to be used within any workflow, but may be difficult to integrate, especially without well-established conventions.

To move away from this limiting dichotomy, the cryo-ET community needs to push for an ecosystem where automation and user-friendliness don't get in the way of customizability and control. Such an ecosystem, however, is founded upon good software practices, which often go against the academia-machine:

1. build small-scoped, generalized and modular **libraries** to allow re-use by many, with a low barrier of entry
2. develop on top of well-established generalized libraries (numpy, pandas, etc.), to minimize wheel-reinventing and lower the learning curve for new users

3. write readable code, and document it extensively, to make adoption and contribution easier
4. develop tools that others would want to use, not tools that only you need
5. release code quickly and openly, without waiting for the lethargic publication industry, to encourage sharing and expedite exchange of ideas
6. engage the community to share maintenance responsibilities and institutional knowledge, in order to prevent abandonware and ensure continued development

These things require expertise in software development and time to dedicate to non-glamorous tasks, both of which are often missing in academia. I was lucky enough to join the napari community — from which I learned a lot on the former — and to have supervisors who valued my independence and self-determination in my PhD career.

## Interactive visualization

Other than generally good software practices, cryo-ET software would benefit from moving towards a human-in-the-loop model, where automation and human supervision are equally important.

This is exactly the goal of a workflow-agnostic and interactive visualization tool such as blik ([Chapter 3: blik: a cryo-ET visualisation and analysis tool](#)), which allows users and developers to view, explore and manipulate the data in a seamless way at any point during the processing.

In cryo-ET, it's crucial to have powerful 3D interactivity, as 2D-only views on 3D data can be extremely limiting in understanding the system. One visualization tool that lacked particularly when we started working on blik was a quick and interactive way to look at and modify particle poses (positions and orientations) within their context in the tomogram (though nowadays other tools with similar capabilities are available<sup>92</sup>).

Similarly, annotation, picking and segmentation tools were (and in large part still are) limited to interactivity only in 2D; this is a limitation shared

across imaging fields, which is why several napari developers are making a concerted effort to make ergonomic 3D interactivity possible.

# Chapter 7

## Future perspectives

This manuscript does not mark the end of the projects herein; the development of blik — and of the ecosystem it lives in — is ongoing, and much more is in the plans to further our understanding of *D. radiodurans* and its key players, such as FtsZ and HU.

### Contents

Contents .....	139
7.1 blik .....	140
STA visualisation <i>in situ</i> .....	140
3D interactivity .....	140
Multicanvas .....	141
7.2 napari .....	141
7.3 Teamtomo .....	142
7.4 <i>D. radiodurans</i> : FtsZ, HU, and more .....	143
Chromatin and HU .....	143
FtsZ SPA .....	143
FtsZ STA .....	144
Effects of stress and radiation .....	145
Structural proteomics .....	145
7.5 Cryo-ET .....	146

Hardware .....	146
Software .....	146
Applications .....	147

## 7.1 blik

The development of blik has already proven useful for daily use in our group and others. However, there are several features that were part of blik's original plan, but which are not yet implemented, or only partially. Other planned enhancements are not specific to blik, but more general napari features which will benefit blik and hopefully many other plugins and applications depending on napari.

### STA visualisation *in situ*

One of the main ones is the ability to visualise subtomogram averages *in situ*, positioned and oriented based on the particle picks they originated from. While some tools that can do this exist<sup>92</sup>, they are either not fully interactive (particles cannot be selected, moved around, or isosurface levels changed), limited in performance, or both. In order to develop this feature, some changes need to be done to napari to allow instance-based mesh and volume rendering. Some of these changes are already partially implemented, and there are plans to continue on this development in the coming months. Developing a generalized framework for such rendering in napari will also benefit several other fields where rendering of high numbers of instances at high performance is needed (molecular dynamics, highly-multiplexed labeling, astrophysics).

### 3D interactivity

3D interactivity in blik can still be significantly improved; some features planned for this purpose are:

1. particle picking on 3D slicing planes, without need to switch to 2D for accurate depth selection
2. more ergonomic controls for orientation selection of picked particles
3. improved two-way interaction between feature plots and 3D view (coloring, classifying, selecting particles)

## Multicanvas

Another crucial improvement for napari (and therefore blik) which is underway and has been on my — and on other napari developers' — to-do list is **full support for multicanvas**. Especially for segmentation and annotation, having access two linked views of 2D and 3D visualisations can make a big difference in the ergonomics of a tool.

## 7.2 napari

This thesis was heavily influenced and shaped by my extended collaboration with the **napari** project<sup>78</sup> and its core developers and community<sup>184</sup>, whose values and goals for the development of scientific software strongly align with mine.

The napari community aims to provide a fast, user-friendly, hackable and reusable library and application for the visualization and annotation of n-dimensional scientific imaging data. It's built on top of the well-established and widespread libraries at the core of the scientific python ecosystem (such as numpy and pandas), in order to allow seamless interactive visualization both programmatically and via graphical user interface. Our committed effort to bridge many different imaging fields in order to share knowledge and resources has resulted in a steady influx of new contributors and users from various backgrounds, who ensured napari remains user-friendly, hackable, and powerful.

Due to the distributed and collaborative nature of community-driven open-source development — especially of as large a project as napari — it's a difficult (and futile) exercise to determine who “authored” a specific

feature, and yet the steady contributions from newcomers shows that this approach to development is what many research developers seek.

Other developers do not directly contribute to napari, but develop plugins for it instead. There are already [many cryo-ET-focused plugins](#) that appeared independently, which build upon some of the groundwork contributed to napari by me as part of this thesis and by many other contributors.

The current [napari roadmap](#) is filled with exciting new features, and I expect that in the next few years the project will continue growing and expanding to new fields.

### 7.3 Teamtomo

As another effort to go against the academia-machine, early on in my PhD, Alister Burt and I started the [teamtomo](#) project, with the goal of creating a shared, open-source resource for cryo-ET developers, and to encourage the community to collaborate on the development of cryo-ET software within the python ecosystem.

While at first we were the only two people involved, at the time of writing almost 30 researchers and developers from several different groups around the world have contributed to libraries and tools in the [teamtomo repositories](#), and more are joining our montly meetings where we plan future concerted efforts.

With time, we aim to collect well-scoped and well-documented libraries that cover all the needs of a cryo-ET data processing pipeline, from simple ones like I/O utilities or cross-correlation, to more complex routines such as tilt-series alignment. Some of these tools — contributed by various developers — are already available, such as [ttmask](#) for mask creation, [cryohub](#) for I/O, or [fidder](#) for fiducial masking.

## 7.4 *D. radiodurans*: FtsZ, HU, and more

The ongoing efforts on HU and FtsZ encountered technical challenges that so far prevented us from reaching high resolution and unraveling the structure and function of these proteins. We already started to work around these challenges, and Harald Bernhard — a joint GenOM/MICA postdoc — has picked up the work on these projects and already started improving on it. There are also new directions in which we'd like to extend our work on *D. radiodurans*, using cryo-EM, cryo-ET and other imaging techniques; particularly, we're interested in understanding the effects of radiation damage on all these processes, and how *D. radiodurans* protects itself from it.

### Chromatin and HU

To increase our chances to identify and pick HU, a new dataset was collected with a phase plate, which allows to collect data closer to focus while improving the contrast of low spatial frequency information (**Section 1.3: Contrast Transfer Function**). Preliminary results on this data showed more classes containing what could be HU in a similar conformation to what was seen in **Figure 5.1B**, but more work is needed.

### FtsZ SPA

Since Harald picked up this project, he has already managed to improve the results from the FtsZ+DDM dataset in a few ways. With careful use of 2D and 3D classifications, it's possible to better isolate single filaments, which improves the initial model generation. Balancing the different views by number of particles also improves the orientation distribution, reducing map artifacts at the cost of some global resolution. Additionally, the use of a bigger box size in particle extraction has improved slightly the quality of the alignments and 2D class averages. While the anisotropy issue remains, the new maps are much more interpretable, and match quite well those by Fujita et al.<sup>174</sup> from *K. pneumoniae* FtsZ (**Figure 7.1**).

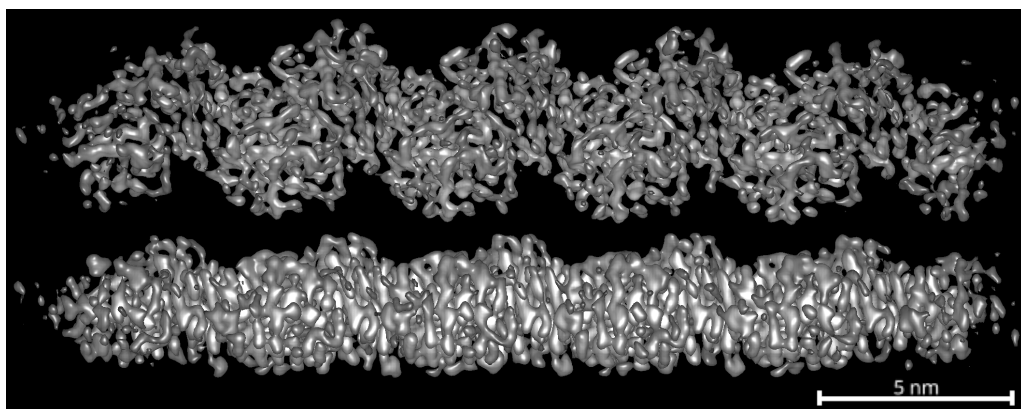


**FIGURE 7.1: 3D map of FtsZ with detergent.** Using the FtsZ+DDM dataset, and more careful 2D and 3D classifications to clean the dataset and better balance different views, Harald significantly improved on the FtsZ filament map. Preferential orientation is unfortunately still not fully solved, as evidenced by the streaking artifacts along one direction (bottom view), which are not present in the other (top view).

Depending on the outcome of the detergent dataset, we might need to go back to the tilted dataset. We think that the process of assigning angles and restricting the search should be theoretically sound, so it may be worth spending more time tweaking parameters in Relion to find a working setup. A recent study by Aiyer et al.<sup>15</sup> showed that negative effects of thickening the sample (due to tilting) should be negligible with proper preprocessing, so the achievable resolution should be unrestricted by the tilt.

## FtsZ STA

The cryo-ET dataset used in the septation paper ([Chapter 4: \*D. radiodurans\*: cell division and septation](#)) was collected with the goal of capturing a wide field of view including a full *D. radiodurans* cell. For this reason, it contains a relatively low amount of FtsZ bundles (which are often not visible and/or not present in the lamellae), and has a relatively high pixel size (4.346 Å/px), which significantly limits our ability to reach high resolutions.

A new dataset has recently been collected by Harald with higher magnification and focused on the septa tips, which will hopefully provide a higher resolution view on the tips.

However, another problem with STA of FtsZ was the preferential orientation of the filaments, a consequence of how *D. radiodurans* lies on the grid. A way to tackle this problem is to force the bacteria into different orientations, for example by creating a dense paste of bacteria to freeze using the waffle method<sup>185</sup>. Preliminary attempts to prepare such sample were promising, but due to technical problems with the cryo-FIB microscope we were not yet able to continue with this sample. Similarly, freezing the sample with a Leica™ plunge freezer showed a more diverse orientation distribution of the bacteria.

## Effects of stress and radiation

*D. radiodurans* is especially intriguing due its incredibly effective radiation and stress resistance machinery. While the FtsZ and HU projects are interesting by themselves, they all fit in a wider question: **How does *D. radiodurans* protect itself from radiation?** To answer this, we plan to compare how the known machineries are affected by radiation exposure. Some preliminary cryo-ET data, collected at the same time as the septation dataset ([Chapter 4: \*D. radiodurans\*: cell division and septation](#)), appeared to show some morphological differences in the nucleoid and membranes after irradiation. New, higher magnification data will probably be collected to move this investigation further.

## Structural proteomics

The study of the effects of radiation damage on *D. radiodurans* may come in the form of another cross-over with the cell-extract project in the MICA group ([Section 5.3: emscan](#)). Cell-extract SPA cryo-EM could be used to perform **structural proteomics**, identifying not only the changes in the proteome caused by irradiation, but the effects that these have on protein structures and complexes.

## 7.5 Cryo-ET

During the course of this thesis, the cryo-ET world has changed a lot, starting from improved sample preparation techniques, all the way to high resolution STA processing and post-processing.

### Hardware

Cryo-FIB milling<sup>53</sup> has become an essential procedure in every group working on cellular tomography, leading to the automation of lamellae production being a major focus of hardware and software development around the world. The combination of FIB milling and Correlative light-electron microscopy (CLEM) is especially powerful, pushing the field towards being able to reliably and accurately locate a structure of interest in a large cell or tissue, cut out a lamella, and image it at high resolution<sup>51,186,187</sup>.

Exciting progress is being made towards cheaper, smaller, lower-energy microscopes that are still powerful and capable of high resolution work<sup>77,188</sup> — though for thicker samples it might be more complicated (**Figure 2.4**). Development of such instruments will hopefully help spread and democratize electron-microscopy, which currently requires extremely expensive equipment (due also in part to the quasi-monopolistic industry) and is therefore in constant lack of supply and out of reach for many researchers around the world.

### Software

During the course of this thesis, many new software suites and standalone tools have appeared, improving the field both in ergonomics and algorithmically.

Software pipelines are steadily moving away from the naive “reconstruct full tomogram -> extract subvolumes” approach in favour of different flavours of per-particle tilt-series, as the field pushes for sub-nanometer resolution.

Interactive visualization tools like blik<sup>72</sup> and ArtiaX<sup>92</sup> appeared to answer the need for a HITL workflow, together with integrative workflow managers like Scipion<sup>85</sup> now providing extensive support for cryo-ET.

Community initiatives — such as Teamtomo — aiming to establish common frameworks and conventions will be paramount to the development of the cryo-ET software ecosystem.

The field giant Relion has implemented an almost full pipeline for cryo-ET and STA<sup>62,74</sup>, and many other complete software suites are being published, often together with novel and unique tools<sup>63,73,75,189,190</sup>.

Of note is also the recently (beta) release of [Warp tools](#), a linux port of Warp<sup>23</sup> allowing to finally integrate parts of the Warp pipeline into others, without the need of using a graphical interface and a Windows machine.

The tide of Machine-learning tools of the last few years has flooded — among many others — the cryo-ET field, giving rise to powerful automated tools for denoising<sup>26</sup>, segmentation<sup>97,191</sup>, picking<sup>31,70</sup>, modeling<sup>46</sup>, structure prediction<sup>1-3</sup>, and much more. While these tools may work like magic, it's important to keep an eye out for hallucinations<sup>192</sup>, especially as the field moves towards heavier and more normalized use of the technology; ML validation and introspection are already a high priority in other fields, and cryo-ET will be no exception.

## Applications

As cryo-ET becomes more widespread, it's being used in a variety of different and novel applications; with this wider spectrum of literature, the community is realizing where cryo-ET really shines, and where other techniques might be preferable. Especially thanks to the evolution of FIB milling and the ever faster data collection, high-resolution structure determination *in situ* can also be achieved by using SPA on the same samples (with all the SNR benefit that comes with it). On the other hand, cryo-ET is establishing as the go-to technique for superstructural studies, where the mesoscale view allows to investigate emergent structures and behaviours which are simply too heterogeneous to be visible via SPA.

A particularly exciting prospect for me is the marriage of cryo-ET and (coarse-grained) molecular dynamics to investigate large systems such as whole cells, which was only dreamed of at the beginning of my thesis<sup>193</sup>. The cryo-ET/MD combination is already bearing fruits in exploring conformational variability<sup>194</sup>, in multi-scale modeling<sup>195</sup>, and much more; it's only a matter of time before we'll be able to take a snapshot of a cell *in situ*, and just simulate to see what happens next.

# List of Figures

1.1	Cryo-EM workflow .....	5
1.2	Vitrification via plunge freezing .....	6
1.3	Image formation .....	9
1.4	CTF: effect of defocus .....	10
1.5	CTF: effect of phase shift .....	11
1.6	CTF: effect of the envelope function .....	12
1.7	Cross-correlation of 1D signals.....	14
1.8	Fourier filtering .....	15
1.9	Central slice theorem .....	19
1.10	Projection matching .....	20
1.11	Fourier shell correlation .....	21
2.1	Cryo-ET workflow .....	25
2.2	FIB milling .....	27
2.3	Missing wedge .....	31
2.4	Particle size limit versus sample thickness .....	35
3.1	Volume visualisations.....	45
3.2	3D particle visualisation and feature plotting.....	47
3.3	Interpolated segmentations .....	49
3.4	Filament-based particle picking.....	51
3.5	Surface generation procedure.....	53
3.6	Surface-based volume resampling .....	54
3.7	Surface mesh and particle picks .....	55

4.1	Structures of exponentially growing <i>D. radiodurans</i> cell walls during the process of cell division .....	72
4.2	In-depth analysis of the structure and composition of the cell wall of <i>D. radiodurans</i> .....	74
4.3	Close-up view of the septal tips .....	78
4.4	Septation through a “sliding doors” mechanism .....	81
4.5	Distinct PG synthesis machineries are involved in septal and outer cell wall growth .....	84
4.6	Localisation of the key cell division factor, FtsZ, in <i>D. radiodurans</i> .....	87
4.7	Schematic model of the septation process in <i>D. radiodurans</i> ..	94
4.8	Cell wall junction examples .....	102
4.9	Membrane protrusion examples .....	103
4.10	Microscopy set-ups for timelapse 3D confocal video-microscopy	104
4.11	PG labelling schematic .....	105
4.12	PG-labelled <i>D. radiodurans</i> .....	106
4.13	Two-color labelled chase experiment .....	107
4.14	Two-color labelled chase experiment with Ampicillin .....	108
4.15	1D density profiles of walls and septa .....	109
5.1	<i>D. radiodurans</i> nucleoids and HU structure .....	112
5.2	HU-induced DNA spirals .....	113
5.3	Filament picking strategies for HU .....	114
5.4	2D classes from filament picking .....	115
5.5	2D classification from Topaz picking .....	115
5.6	FtsZ forms a ring <i>in vivo</i> and filaments <i>in vitro</i> .....	117
5.7	Micrographs of FtsZ filaments .....	119
5.8	FtsZ filament: 2D classes .....	119
5.9	FtsZ filament: anisotropic map .....	120
5.10	FtsZ tilted dataset: 2D classes .....	121
5.11	Correlation between in-plane angle and 2D class .....	122
5.12	Micrographs of FtsZ with detergent .....	124
5.13	2D classes of FtsZ with detergent .....	124

*LIST OF FIGURES*

151

5.14 FtsZ: tomogram slices from top and side view .....	125
5.15 Surface-based FtsZ particle picks for STA .....	126
5.16 FtsZ STA preliminary results .....	127
7.1 3D map of FtsZ with detergent .....	144

# Glossary

<b>CC</b>	Cross-correlation
<b>CLEM</b>	Correlative light-electron microscopy
<b>CTF</b>	Contrast Transfer Function
<b>Cryo-EM</b>	Cryo-electron microscopy
<b>Cryo-ET</b>	Cryo-electron tomography
<b>FIB</b>	Focused Ion Beam
<b>FT</b>	Fourier transform
<b>HITL</b>	Human-in-the-loop
<b>I/O</b>	Input/Output
<b>ND</b>	N-dimensional
<b>NMR</b>	Nuclear Magnetic Resonance
<b>PS</b>	Power Spectrum
<b>PSF</b>	Point spread function
<b>SEM</b>	Scanning Electron Microscope
<b>SPA</b>	Single particle analysis
<b>STA</b>	Subtomogram averaging

# Bibliography

- [1] John Jumper, Richard Evans, Alexander Pritzel, Tim Green, Michael Figurnov, Olaf Ronneberger, Kathryn Tunyasuvunakool, Russ Bates, Augustin Žídek, Anna Potapenko, Alex Bridgland, Clemens Meyer, Simon A. A. Kohl, Andrew J. Ballard, Andrew Cowie, Bernardino Romera-Paredes, Stanislav Nikolov, Rishub Jain, Jonas Adler, Trevor Back, Stig Petersen, David Reiman, Ellen Clancy, Michal Zielinski, Martin Steinegger, Michalina Pacholska, Tamas Berghammer, Sebastian Bodenstein, David Silver, Oriol Vinyals, Andrew W. Senior, Koray Kavukcuoglu, Pushmeet Kohli, and Demis Hassabis. Highly accurate protein structure prediction with AlphaFold. *Nature*, 596(7873):583–589, August 2021. ISSN 1476-4687.  
[DOI: 10.1038/s41586-021-03819-2](https://doi.org/10.1038/s41586-021-03819-2). (pg. 2, 147)
- [2] Josh Abramson, Jonas Adler, Jack Dunger, Richard Evans, Tim Green, Alexander Pritzel, Olaf Ronneberger, Lindsay Willmore, Andrew J. Ballard, Joshua Bambrick, Sebastian W. Bodenstein, David A. Evans, Chia-Chun Hung, Michael O'Neill, David Reiman, Kathryn Tunyasuvunakool, Zachary Wu, Akvilė Žemgulytė, Eirini Arvaniti, Charles Beattie, Ottavia Bertolli, Alex Bridgland, Alexey Cherepanov, Miles Congreve, Alexander I. Cowen-Rivers, Andrew Cowie, Michael Figurnov, Fabian B. Fuchs, Hannah Gladman, Rishub Jain, Yousuf A. Khan, Caroline M. R. Low, Kuba Perlin, Anna Potapenko, Pascal Savy, Sukhdeep Singh, Adrian Stecula, Ashok Thillaisundaram, Catherine Tong, Sergei Yakneen, Ellen D. Zhong, Michal Zielinski, Augustin Žídek, Victor Bapst, Pushmeet Kohli, Max Jaderberg, Demis Hassabis, and John M. Jumper. Accurate structure prediction of biomolecular interactions with AlphaFold 3. *Nature*, 630(8016):493–500, June 2024. ISSN 1476-4687.  
[DOI: 10.1038/s41586-024-07487-w](https://doi.org/10.1038/s41586-024-07487-w). (pg. 2, 24, 147)
- [3] Minkyung Baek, Frank DiMaio, Ivan Anishchenko, Justas Dauparas, Sergey Ovchinnikov, Gyu Rie Lee, Jue Wang, Qian Cong, Lisa N. Kinch, R. Dustin Schaeffer, Claudia Millán, Hahnbeom Park, Carson Adams, Caleb R. Glassman, Andy DeGiovanni, Jose H. Pereira, Andria V. Rodrigues, Alberdina A. van Dijk, Ana C. Ebrecht, Diederik J. Opperman, Theo Sagmeister, Christoph Buhlheller, Tea Pavkov-Keller, Manoj K. Rathinaswamy, Udit Dalwadi, Calvin K. Yip, John E. Burke, K. Christopher

- Garcia, Nick V. Grishin, Paul D. Adams, Randy J. Read, and David Baker. Accurate prediction of protein structures and interactions using a three-track neural network. *Science*, 373(6557):871–876, August 2021. DOI: [10.1126/science.abj8754](https://doi.org/10.1126/science.abj8754). (pg. 2, 147)
- [4] Helen M. Berman, John Westbrook, Zukang Feng, Gary Gilliland, T. N. Bhat, Helge Weissig, Ilya N. Shindyalov, and Philip E. Bourne. The Protein Data Bank. *Nucleic Acids Research*, 28(1):235–242, January 2000. ISSN 0305-1048. DOI: [10.1093/nar/28.1.235](https://doi.org/10.1093/nar/28.1.235). (pg. 3)
- [5] Helen Berman, Kim Henrick, and Haruki Nakamura. Announcing the worldwide Protein Data Bank. *Nat Struct Mol Biol*, 10(12):980–980, December 2003. ISSN 1545-9985. DOI: [10.1038/nsb1203-980](https://doi.org/10.1038/nsb1203-980). (pg. 3)
- [6] A. Ravikumar, M. N. Gopnarayan, S. Subramaniam, and N. Srinivasan. Comparison of side-chain dispersion in protein structures determined by cryo-EM and X-ray crystallography. *IUCrJ*, 9(1):98–103, January 2022. ISSN 2052-2525. DOI: [10.1107/S2052252521011945](https://doi.org/10.1107/S2052252521011945). (pg. 3)
- [7] A. R. Faruqi and Sriram Subramaniam. CCD detectors in high-resolution biological electron microscopy. *Quart. Rev. Biophys.*, 33(1):1–27, February 2000. ISSN 0033-5835, 1469-8994. DOI: [10.1017/S0033583500003577](https://doi.org/10.1017/S0033583500003577). (pg. 4)
- [8] Jacques Dubochet, Marc Adrian, Jiin-Ju Chang, Jean-Claude Homo, Jean Lepault, Alasdair W. McDowall, and Patrick Schultz. Cryo-electron microscopy of vitrified specimens. *Quarterly Reviews of Biophysics*, 21(2):129–228, May 1988. ISSN 1469-8994, 0033-5835. DOI: [10.1017/S0033583500004297](https://doi.org/10.1017/S0033583500004297). (pg. 5)
- [9] Jae-Hee Chung and Ho Min Kim. The Nobel Prize in Chemistry 2017: High-Resolution Cryo-Electron Microscopy. *Applied Microscopy*, 47(4):218–222, December 2017. ISSN 2287-5123. DOI: [10.9729/AM.2017.47.4.218](https://doi.org/10.9729/AM.2017.47.4.218). (pg. 6)
- [10] Olivier Gemin, Victor Armijo, Michael Hons, Caroline Bissardon, Romain Linares, Matthew W. Bowler, Georg Wolff, Kirill Kovalev, Anastasiia Babenko, Veijo T. Salo, Sarah Schneider, Christopher Rossi, Léa Lecomte, Thibault Deckers, Kévin Lauzier, Robert Janocha, Franck Felisaz, Jérémie Sinoir, Wojciech Galej, Julia Mahamid, Christoph W. Müller, Sebastian Estermann, Simone Mattei, Florent Cipriani, and Gergely Papp. EasyGrid: A versatile platform for automated cryo-EM sample preparation and quality control. Preprint, Molecular Biology, January 2024. (pg. 5)
- [11] Alex J Noble, Venkata P Dandey, Hui Wei, Julia Brasch, Jillian Chase, Priyamvada Acharya, Yong Zi Tan, Zhenning Zhang, Laura Y Kim, Giovanna Scapin, Micah Rapp,

- Edward T Eng, William J Rice, Anchi Cheng, Carl J Negro, Lawrence Shapiro, Peter D Kwong, David Jeruzalmi, Amedee des Georges, Clinton S Potter, and Bridget Carragher. Routine single particle CryoEM sample and grid characterization by tomography. *eLife*, 7:e34257, May 2018. ISSN 2050-084X. DOI: [10.7554/eLife.34257](https://doi.org/10.7554/eLife.34257). (pg. 5)
- [12] Ye Lu, Nan Liu, Yongbo Liu, Liming Zheng, Junhao Yang, Jia Wang, Xia Jia, Qinru Zi, Hailin Peng, Yu Rao, and Hong-Wei Wang. Functionalized graphene grids with various charges for single-particle cryo-EM. *Nat Commun*, 13(1):6718, November 2022. ISSN 2041-1723. DOI: [10.1038/s41467-022-34579-w](https://doi.org/10.1038/s41467-022-34579-w). (pg. 6, 120)
- [13] Corinne Crucifix, Muriel Uhring, and Patrick Schultz. Immobilization of biotinylated DNA on 2-D streptavidin crystals. *Journal of Structural Biology*, 146(3):441–451, June 2004. ISSN 1047-8477. DOI: [10.1016/j.jsb.2004.02.001](https://doi.org/10.1016/j.jsb.2004.02.001). (pg. 6, 120)
- [14] Bong-Gyo Han, Zoe Watson, Hannah Kang, Arto Pulk, Kenneth H. Downing, Jamie Cate, and Robert M. Glaeser. Long shelf-life streptavidin support-films suitable for electron microscopy of biological macromolecules. *Journal of Structural Biology*, 195(2):238–244, August 2016. ISSN 1047-8477. DOI: [10.1016/j.jsb.2016.06.009](https://doi.org/10.1016/j.jsb.2016.06.009). (pg. 6, 120)
- [15] Sriram Aiyer, Philip R. Baldwin, Shi Min Tan, Zelin Shan, Juntaek Oh, Atousa Mehrani, Marianne E. Bowman, Gordon Louie, Dario Oliveira Passos, Selena Đorđević-Marquardt, Mario Mietzsch, Joshua A. Hull, Shuichi Hoshika, Benjamin A. Barad, Danielle A. Grotjahn, Robert McKenna, Mavis Agbandje-McKenna, Steven A. Benner, Joseph A. P. Noel, Dong Wang, Yong Zi Tan, and Dmitry Lyumkis. Overcoming resolution attenuation during tilted cryo-EM data collection. *Nat Commun*, 15(1):389, January 2024. ISSN 2041-1723. DOI: [10.1038/s41467-023-44555-7](https://doi.org/10.1038/s41467-023-44555-7). (pg. 6, 144)
- [16] Martin Schorb, Isabella Haberbosch, Wim J. H. Hagen, Yannick Schwab, and David N. Mastronarde. Software tools for automated transmission electron microscopy. *Nat Methods*, 16(6):471–477, June 2019. ISSN 1548-7105. DOI: [10.1038/s41592-019-0396-9](https://doi.org/10.1038/s41592-019-0396-9). (pg. 7)
- [17] Wen Jiang and Wah Chiu. Web-based Simulation for Contrast Transfer Function and Envelope Functions. *Microscopy and Microanalysis*, 7(4):329–334, July 2001. ISSN 1431-9276. DOI: [10.1007/S10005-001-0004-4](https://doi.org/10.1007/S10005-001-0004-4). (pg. 10, 11, 12)
- [18] Radostin Danev and Wolfgang Baumeister. Expanding the boundaries of cryo-EM with phase plates. *Current Opinion in Structural Biology*, 46:87–94, October 2017. ISSN 0959-440X. DOI: [10.1016/j.sbi.2017.06.006](https://doi.org/10.1016/j.sbi.2017.06.006). (pg. 11)

- [19] Osip Schwartz, Jeremy J. Axelrod, Sara L. Campbell, Carter Turnbaugh, Robert M. Glaeser, and Holger Müller. Laser phase plate for transmission electron microscopy. *Nat Methods*, 16(10):1016–1020, October 2019. ISSN 1548-7105. DOI: [10.1038/s41592-019-0552-2](https://doi.org/10.1038/s41592-019-0552-2). (pg. 11)
- [20] Wikipedia. Convolution theorem. *Wikipedia*, June 2024. (pg. 12)
- [21] Shawn Q. Zheng, Eugene Palovcak, Jean-Paul Armache, Kliment A. Verba, Yifan Cheng, and David A. Agard. MotionCor2: Anisotropic correction of beam-induced motion for improved cryo-electron microscopy. *Nat Methods*, 14(4):331–332, April 2017. ISSN 1548-7105. DOI: [10.1038/nmeth.4193](https://doi.org/10.1038/nmeth.4193). (pg. 13)
- [22] Ali Punjani, John L. Rubinstein, David J. Fleet, and Marcus A. Brubaker. cryoSPARC: Algorithms for rapid unsupervised cryo-EM structure determination. *Nature Methods*, 14(3):290–296, March 2017. ISSN 1548-7105. DOI: [10.1038/nmeth.4169](https://doi.org/10.1038/nmeth.4169). (pg. 13, 16, 22, 114, 118, 123, 131)
- [23] Dmitry Tegunov and Patrick Cramer. Real-time cryo-electron microscopy data preprocessing with Warp. *Nat Methods*, 16(11):1146–1152, November 2019. ISSN 1548-7091, 1548-7105. DOI: [10.1038/s41592-019-0580-y](https://doi.org/10.1038/s41592-019-0580-y). (pg. 13, 14, 30, 33, 40, 100, 126, 128, 136, 147)
- [24] Jaakko Lehtinen, Jacob Munkberg, Jon Hasselgren, Samuli Laine, Tero Karras, Miika Aittala, and Timo Aila. Noise2Noise: Learning Image Restoration without Clean Data. *arXiv:1803.04189 [cs, stat]*, October 2018. Comment: Added link to official implementation and updated MRI results to match it. (pg. 14)
- [25] Alexander Krull, Tim-Oliver Buchholz, and Florian Jug. Noise2Void - Learning Denoising From Single Noisy Images. In *Proceedings of the IEEE/CVF Conference on Computer Vision and Pattern Recognition*, pages 2129–2137, 2019. (pg. 14)
- [26] Tristan Bepler, Kotaro Kelley, Alex J. Noble, and Bonnie Berger. Topaz-Denoise: General deep denoising models for cryoEM and cryoET, May 2020. (pg. 14, 40, 41, 100, 128, 147)
- [27] Tim-Oliver Buchholz, Mareike Jordan, Gaia Pigino, and Florian Jug. Cryo-CARE: Content-Aware Image Restoration for Cryo-Transmission Electron Microscopy Data. *arXiv:1810.05420 [cs]*, October 2018. Comment: This work has been submitted to the IEEE for possible publication. Copyright may be transferred without notice, after which this version may no longer be accessible. This version fixed flipped graph labels in Figure 5. (pg. 14, 40)

- [28] Sjors H. W. Scheres. RELION: Implementation of a Bayesian approach to cryo-EM structure determination. *Journal of Structural Biology*, 180(3):519–530, December 2012. ISSN 1047-8477. DOI: [10.1016/j.jsb.2012.09.006](https://doi.org/10.1016/j.jsb.2012.09.006). (pg. 16, 17, 22, 40, 55, 123, 126, 128, 131)
- [29] Shaoda He and Sjors H. W. Scheres. Helical reconstruction in RELION. *Journal of Structural Biology*, 198(3):163–176, June 2017. ISSN 1047-8477. DOI: [10.1016/j.jsb.2017.02.003](https://doi.org/10.1016/j.jsb.2017.02.003). (pg. 16)
- [30] Thorsten Wagner, Felipe Merino, Markus Stabrin, Toshio Moriya, Claudia Antoni, Amir Apelbaum, Philine Hagel, Oleg Sitsel, Tobias Raisch, Daniel Prumbaum, Dennis Quentin, Daniel Roderer, Sebastian Tacke, Birte Siebolds, Evelyn Schubert, Tanvir R. Shaikh, Pascal Lill, Christos Gatsogiannis, and Stefan Raunser. SPHIRE-crYOLO is a fast and accurate fully automated particle picker for cryo-EM. *Commun Biol*, 2(1):218, December 2019. ISSN 2399-3642. DOI: [10.1038/s42003-019-0437-z](https://doi.org/10.1038/s42003-019-0437-z). (pg. 16, 32, 40, 41, 57)
- [31] Thorsten Wagner and Stefan Raunser. The evolution of SPHIRE-crYOLO particle picking and its application in automated cryo-EM processing workflows. *Commun Biol*, 3(1):61, December 2020. ISSN 2399-3642. DOI: [10.1038/s42003-020-0790-y](https://doi.org/10.1038/s42003-020-0790-y). (pg. 16, 32, 147)
- [32] Chih-Chia Su, Meinan Lyu, Christopher E. Morgan, Jani Reddy Bolla, Carol V. Robinson, and Edward W. Yu. A ‘Build and Retrieve’ methodology to simultaneously solve cryo-EM structures of membrane proteins. *Nat Methods*, 18(1):69–75, January 2021. ISSN 1548-7105. DOI: [10.1038/s41592-020-01021-2](https://doi.org/10.1038/s41592-020-01021-2). (pg. 17, 128)
- [33] Fotis L. Kyritis, Annette Meister, and Panagiotis L. Kastritis. Integrative biology of native cell extracts: A new era for structural characterization of life processes. *Biological Chemistry*, 400(7):831–846, July 2019. ISSN 1437-4315. DOI: [10.1515/hsz-2018-0445](https://doi.org/10.1515/hsz-2018-0445). (pg. 17, 128)
- [34] Wikipedia. Projection-slice theorem. *Wikipedia*, July 2023. (pg. 18)
- [35] A. H. Andersen and A. C. Kak. Simultaneous Algebraic Reconstruction Technique (SART): A Superior Implementation of the Art Algorithm. *Ultrason Imaging*, 6(1): 81–94, January 1984. ISSN 0161-7346. DOI: [10.1177/016173468400600107](https://doi.org/10.1177/016173468400600107). (pg. 18)
- [36] J. I. Agulleiro and J. J. Fernandez. Fast tomographic reconstruction on multicore computers. *Bioinformatics*, 27(4):582–583, February 2011. ISSN 1367-4803. DOI: [10.1093/bioinformatics/btq692](https://doi.org/10.1093/bioinformatics/btq692). (pg. 18)

- [37] Wikipedia. Tomographic reconstruction. [https://en.wikipedia.org/w/index.php?title=Tomographic\\_reconstruction&oldid=1230834962#Back\\_projection\\_algorithm](https://en.wikipedia.org/w/index.php?title=Tomographic_reconstruction&oldid=1230834962#Back_projection_algorithm), June 2024. (pg. 18)
- [38] Eva Nogales and Sjors H. W. Scheres. Cryo-EM: A Unique Tool for the Visualization of Macromolecular Complexity. *Molecular Cell*, 58(4):677–689, May 2015. ISSN 1097-2765. DOI: [10.1016/j.molcel.2015.02.019](https://doi.org/10.1016/j.molcel.2015.02.019). (pg. 19, 20)
- [39] Richard Anthony Crowther, D. J. DeRosier, and Aaron Klug. The reconstruction of a three-dimensional structure from projections and its application to electron microscopy. *Proceedings of the Royal Society of London. A. Mathematical and Physical Sciences*, 317(1530):319–340, January 1997. DOI: [10.1098/rspa.1970.0119](https://doi.org/10.1098/rspa.1970.0119). (pg. 18)
- [40] Daniel Castaño-Díez, Mikhail Kudryashev, Marcel Arheit, and Henning Stahlberg. Dynamo: A flexible, user-friendly development tool for subtomogram averaging of cryo-EM data in high-performance computing environments. *Journal of Structural Biology*, 178(2):139–151, May 2012. ISSN 1047-8477. DOI: [10.1016/j.jsb.2011.12.017](https://doi.org/10.1016/j.jsb.2011.12.017). (pg. 20, 40, 50, 56)
- [41] Ali Punjani and David J. Fleet. 3D variability analysis: Resolving continuous flexibility and discrete heterogeneity from single particle cryo-EM. *Journal of Structural Biology*, 213(2):107702, June 2021. ISSN 1047-8477. DOI: [10.1016/j.jsb.2021.107702](https://doi.org/10.1016/j.jsb.2021.107702). (pg. 20)
- [42] Takanori Nakane and Sjors H. W. Scheres. Multi-body Refinement of Cryo-EM Images in RELION. *Methods Mol Biol*, 2215:145–160, 2021. ISSN 1940-6029. DOI: [10.1007/978-1-0716-0966-8\\_7](https://doi.org/10.1007/978-1-0716-0966-8_7). (pg. 20)
- [43] Ali Punjani and David Fleet. 3D Flexible Refinement: Structure and Motion of Flexible Proteins from Cryo-EM. *Microscopy and Microanalysis*, 28(S1):1218, August 2022. ISSN 1431-9276. DOI: [10.1017/S1431927622005074](https://doi.org/10.1017/S1431927622005074). (pg. 20)
- [44] Peter B. Rosenthal and Richard Henderson. Optimal Determination of Particle Orientation, Absolute Hand, and Contrast Loss in Single-particle Electron Cryomicroscopy. *Journal of Molecular Biology*, 333(4):721–745, October 2003. ISSN 0022-2836. DOI: [10.1016/j.jmb.2003.07.013](https://doi.org/10.1016/j.jmb.2003.07.013). (pg. 21)
- [45] Dmitry Tegunov, Liang Xue, Christian Dienemann, Patrick Cramer, and Julia Mahamid. Multi-particle cryo-EM refinement with M visualizes ribosome-antibiotic complex at 3.5 Å in cells. *Nat Methods*, 18(2):186–193, February 2021. ISSN 1548-7105. DOI: [10.1038/s41592-020-01054-7](https://doi.org/10.1038/s41592-020-01054-7). (pg. 22, 29, 33, 40, 55)

- [46] Kiarash Jamali, Lukas Käll, Rui Zhang, Alan Brown, Dari Kimanis, and Sjors H. W. Scheres. Automated model building and protein identification in cryo-EM maps. *Nature*, 628(8007):450–457, April 2024. ISSN 1476-4687. DOI: [10.1038/s41586-024-07215-4](https://doi.org/10.1038/s41586-024-07215-4). (pg. 22, 147)
- [47] Radon J. On the determination of functions from their integrals along certain manifolds. *Mathematisch-Physische Klasse*, 69:262–277, 1917. (pg. 25)
- [48] Vladan Lučić, Alexander Rigort, and Wolfgang Baumeister. Cryo-electron tomography: The challenge of doing structural biology in situ. *J Cell Biol*, 202(3):407–419, August 2013. ISSN 0021-9525. DOI: [10.1083/jcb.201304193](https://doi.org/10.1083/jcb.201304193). (pg. 25)
- [49] Martin Turk and Wolfgang Baumeister. The promise and the challenges of cryo-electron tomography. *FEBS Letters*, 594(20):3243–3261, 2020. ISSN 1873-3468. DOI: [10.1002/1873-3468.13948](https://doi.org/10.1002/1873-3468.13948). (pg. 25, 40)
- [50] H. Moor, G. Bellin, C. Sandri, and K. Akert. The influence of high pressure freezing on mammalian nerve tissue. *Cell Tissue Res.*, 209(2):201–216, July 1980. ISSN 1432-0878. DOI: [10.1007/BF00237626](https://doi.org/10.1007/BF00237626). (pg. 26)
- [51] Casper Berger, Navya Premaraj, Raimond B. G. Ravelli, Kèvin Knoops, Carmen López-Iglesias, and Peter J. Peters. Cryo-electron tomography on focused ion beam lamellae transforms structural cell biology. *Nat Methods*, 20(4):499–511, April 2023. ISSN 1548-7105. DOI: [10.1038/s41592-023-01783-5](https://doi.org/10.1038/s41592-023-01783-5). (pg. 26, 146)
- [52] D C Pease and K R Porter. Electron microscopy and ultramicrotomy. *Journal of Cell Biology*, 91(3):287s–292s, February 1981. ISSN 0021-9525. DOI: [10.1083/jcb.91.3.287s](https://doi.org/10.1083/jcb.91.3.287s). (pg. 26)
- [53] Michael Marko, Chyongere Hsieh, Richard Schalek, Joachim Frank, and Carmen Mannella. Focused-ion-beam thinning of frozen-hydrated biological specimens for cryo-electron microscopy. *Nat Methods*, 4(3):215–217, March 2007. ISSN 1548-7091, 1548-7105. DOI: [10.1038/nmeth1014](https://doi.org/10.1038/nmeth1014). (pg. 26, 146)
- [54] Elizabeth Villa, Miroslava Schaffer, Jürgen M Plitzko, and Wolfgang Baumeister. Opening windows into the cell: Focused-ion-beam milling for cryo-electron tomography. *Current Opinion in Structural Biology*, 23(5):771–777, October 2013. ISSN 0959-440X. DOI: [10.1016/j.sbi.2013.08.006](https://doi.org/10.1016/j.sbi.2013.08.006). (pg. 27)
- [55] Bruce F. McEwen, Kenneth H. Downing, and Robert M. Glaeser. The relevance of dose-fractionation in tomography of radiation-sensitive specimens. *Ultramicroscopy*, 60(3):357–373, October 1995. ISSN 0304-3991. DOI: [10.1016/0304-3991\(95\)00082-8](https://doi.org/10.1016/0304-3991(95)00082-8). (pg. 28)

- [56] Wim J.H. Hagen, William Wan, and John A.G. Briggs. Implementation of a cryo-electron tomography tilt-scheme optimized for high resolution subtomogram averaging. *J Struct Biol*, 197(2):191–198, February 2017. ISSN 1047-8477. DOI: [10.1016/j.jsb.2016.06.007](https://doi.org/10.1016/j.jsb.2016.06.007). (pg. 28)
- [57] Julia Cope, John Heumann, and Andreas Hoenger. Cryo-Electron Tomography for Structural Characterization of Macromolecular Complexes. *Current Protocols in Protein Science*, 65(1):17.13.1–17.13.31, 2011. ISSN 1934-3663. DOI: [10.1002/0471140864.ps1713s65](https://doi.org/10.1002/0471140864.ps1713s65). (pg. 28)
- [58] Daniela Nicastro, Cindi Schwartz, Jason Pierson, Richard Gaudette, Mary E. Porter, and J. Richard McIntosh. The Molecular Architecture of Axonemes Revealed by Cryo-electron Tomography. *Science*, 313(5789):944–948, August 2006. DOI: [10.1126/science.1128618](https://doi.org/10.1126/science.1128618). (pg. 29, 40)
- [59] John M. Heumann, Andreas Hoenger, and David N. Mastronarde. Clustering and variance maps for cryo-electron tomography using wedge-masked differences. *Journal of Structural Biology*, 175(3):288–299, September 2011. ISSN 1047-8477. DOI: [10.1016/j.jsb.2011.05.011](https://doi.org/10.1016/j.jsb.2011.05.011). (pg. 29, 40)
- [60] Daniel Castaño-Díez, Mikhail Kudryashev, and Henning Stahlberg. Dynamo Catalogue: Geometrical tools and data management for particle picking in subtomogram averaging of cryo-electron tomograms. *Journal of Structural Biology*, 197(2):135–144, February 2017. ISSN 1047-8477. DOI: [10.1016/j.jsb.2016.06.005](https://doi.org/10.1016/j.jsb.2016.06.005). (pg. 29, 32, 50, 135)
- [61] Shawn Zheng, Georg Wolff, Garrett Greenan, Zhen Chen, Frank G. A. Faas, Montserrat Bárcena, Abraham J. Koster, Yifan Cheng, and David A. Agard. AreTomo: An integrated software package for automated marker-free, motion-corrected cryo-electron tomographic alignment and reconstruction. *Journal of Structural Biology: X*, 6:100068, January 2022. ISSN 2590-1524. DOI: [10.1016/j.jsbx.2022.100068](https://doi.org/10.1016/j.jsbx.2022.100068). (pg. 29, 40, 41, 100, 128, 136)
- [62] Alister Burt, Bogdan Toader, Rangana Warshamanage, Andriko von Kügelgen, Euan Pyle, Jasenko Zivanov, Dari Kimanius, Tanmay A. M. Bharat, and Sjors H. W. Scheres. An image processing pipeline for electron cryo-tomography in RELION-5, April 2024. (pg. 29, 126, 128, 135, 147)
- [63] Jesús G. Galaz-Montoya, John Flanagan, Michael F. Schmid, and Steven J. Ludtke. Single Particle Tomography in EMAN2. *J Struct Biol*, 190(3):279–290, June 2015. ISSN 1047-8477. DOI: [10.1016/j.jsb.2015.04.016](https://doi.org/10.1016/j.jsb.2015.04.016). (pg. 29, 40, 41, 57, 147)

- [64] Muyuan Chen, James M. Bell, Xiaodong Shi, Stella Y. Sun, Zhao Wang, and Steven J. Ludtke. A complete data processing workflow for cryo-ET and subtomogram averaging. *Nat Methods*, 16(11):1161–1168, November 2019. ISSN 1548-7091, 1548-7105. DOI: [10.1038/s41592-019-0591-8](https://doi.org/10.1038/s41592-019-0591-8). (pg. 29, 33)
- [65] Beata Turoňová, Florian K. M. Schur, William Wan, and John A. G. Briggs. Efficient 3D-CTF correction for cryo-electron tomography using NovaCTF improves subtomogram averaging resolution to 3.4Å. *Journal of Structural Biology*, 199(3): 187–195, September 2017. ISSN 1047-8477. DOI: [10.1016/j.jsb.2017.07.007](https://doi.org/10.1016/j.jsb.2017.07.007). (pg. 30, 33, 40)
- [66] Alister Burt. Teamtomo/fidder. teamtomo, July 2024. (pg. 30)
- [67] Yun-Tao Liu, Heng Zhang, Hui Wang, Chang-Lu Tao, Guo-Qiang Bi, and Z. Hong Zhou. Isotropic Reconstruction of Electron Tomograms with Deep Learning, July 2021. (pg. 30)
- [68] Haonan Zhang, Yan Li, Yanan Liu, Dongyu Li, Lin Wang, Kai Song, Keyan Bao, and Ping Zhu. A method for restoring signals and revealing individual macromolecule states in cryo-ET, REST. *Nat Commun*, 14(1):2937, May 2023. ISSN 2041-1723. DOI: [10.1038/s41467-023-38539-w](https://doi.org/10.1038/s41467-023-38539-w). (pg. 30)
- [69] Juan Nunez-Iglesias, Adam J. Blanch, Oliver Looker, Matthew W. Dixon, and Leann Tilley. A new Python library to analyse skeleton images confirms malaria parasite remodelling of the red blood cell membrane skeleton. *PeerJ*, 6:e4312, February 2018. ISSN 2167-8359. DOI: [10.7717/peerj.4312](https://doi.org/10.7717/peerj.4312). (pg. 32)
- [70] Gavin Rice, Thorsten Wagner, Markus Stabrin, Oleg Sitsel, Daniel Prumbaum, and Stefan Raunser. TomoTwin: Generalized 3D localization of macromolecules in cryo-electron tomograms with structural data mining. *Nat Methods*, 20(6):871–880, June 2023. ISSN 1548-7105. DOI: [10.1038/s41592-023-01878-z](https://doi.org/10.1038/s41592-023-01878-z). (pg. 32, 40, 147)
- [71] Guole Liu, Tongxin Niu, Mengxuan Qiu, Yun Zhu, Fei Sun, and Ge Yang. DeepET-Picker: Fast and accurate 3D particle picking for cryo-electron tomography using weakly supervised deep learning. *Nat Commun*, 15(1):2090, March 2024. ISSN 2041-1723. DOI: [10.1038/s41467-024-46041-0](https://doi.org/10.1038/s41467-024-46041-0). (pg. 32)
- [72] Lorenzo Gaifas, Moritz A. Kirchner, Joanna Timmins, and Irina Gutsche. Blik is an extensible 3D visualisation tool for the annotation and analysis of cryo-electron tomography data. *PLOS Biology*, 22(4):e3002447, April 2024. ISSN 1545-7885. DOI: [10.1371/journal.pbio.3002447](https://doi.org/10.1371/journal.pbio.3002447). (pg. 32, 71, 100, 126, 147)

- [73] Benjamin A. Himes and Peijun Zhang. emClarity: Software for high-resolution cryo-electron tomography and subtomogram averaging. *Nat Methods*, 15(11): 955–961, November 2018. ISSN 1548-7105. DOI: [10.1038/s41592-018-0167-z](https://doi.org/10.1038/s41592-018-0167-z). (pg. 33, 40, 147)
- [74] Jasenko Zivanov, Joaquín Otón, Zunlong Ke, Andriko von Kügelgen, Euan Pyle, Kun Qu, Dustin Morado, Daniel Castaño-Díez, Giulia Zanetti, Tanmay AM Bharat, John AG Briggs, and Sjors HW Scheres. A Bayesian approach to single-particle electron cryo-tomography in RELION-4.0. *eLife*, 11:e83724, December 2022. ISSN 2050-084X. DOI: [10.7554/eLife.83724](https://doi.org/10.7554/eLife.83724). (pg. 33, 40, 126, 128, 135, 147)
- [75] Jesús G. Galaz-Montoya, Corey W. Hecksel, Philip R. Baldwin, Eryu Wang, Scott C. Weaver, Michael F. Schmid, Steven J. Ludtke, and Wah Chiu. Alignment algorithms and per-particle CTF correction for single particle cryo-electron tomography. *Journal of Structural Biology*, 194(3):383–394, June 2016. ISSN 1047-8477. DOI: [10.1016/j.jsb.2016.03.018](https://doi.org/10.1016/j.jsb.2016.03.018). (pg. 33, 147)
- [76] Christopher J. Russo, Joshua L. Dickerson, and Katerina Naydenova. Cryomicroscopy in situ : What is the smallest molecule that can be directly identified without labels in a cell? *Faraday Discussions*, 240(0):277–302, 2022. DOI: [10.1039/D2FD00076H](https://doi.org/10.1039/D2FD00076H). (pg. 34)
- [77] Russo. Electron cryomicroscope hardware: Past, present, and future - Chris Russo, December 2023. (pg. 35, 146)
- [78] The napari Community. Napari: A multi-dimensional image viewer for Python, 2024. (pg. 37, 41, 129, 141)
- [79] Florian KM Schur. Toward high-resolution in situ structural biology with cryo-electron tomography and subtomogram averaging. *Current Opinion in Structural Biology*, 58:1–9, October 2019. ISSN 0959-440X. DOI: [10.1016/j.sbi.2019.03.018](https://doi.org/10.1016/j.sbi.2019.03.018). (pg. 40)
- [80] Alister Burt, Lorenzo Gaifas, Tom Dendooven, and Irina Gutsche. A flexible framework for multi-particle refinement in cryo-electron tomography. *PLOS Biology*, 19 (8):e3001319, August 2021. ISSN 1545-7885. DOI: [10.1371/journal.pbio.3001319](https://doi.org/10.1371/journal.pbio.3001319). (pg. 40, 50, 55)
- [81] Stefano Scaramuzza and Daniel Castaño-Díez. Step-by-step guide to efficient subtomogram averaging of virus-like particles with Dynamo. *PLOS Biology*, 19(8): e3001318, August 2021. ISSN 1545-7885. DOI: [10.1371/journal.pbio.3001318](https://doi.org/10.1371/journal.pbio.3001318). (pg. 40)

- [82] James R. Kremer, David N. Mastronarde, and J. Richard McIntosh. Computer Visualization of Three-Dimensional Image Data Using IMOD. *Journal of Structural Biology*, 116(1):71–76, January 1996. ISSN 1047-8477. DOI: [10.1006/jsbi.1996.0013](https://doi.org/10.1006/jsbi.1996.0013). (pg. 40, 56)
- [83] Thomas Hrabe, Yuxiang Chen, Stefan Pfeffer, Luis Kuhn Cuellar, Ann-Victoria Mangold, and Friedrich Förster. PyTom: A python-based toolbox for localization of macromolecules in cryo-electron tomograms and subtomogram analysis. *Journal of Structural Biology*, 178(2):177–188, May 2012. ISSN 1047-8477. DOI: [10.1016/j.jsb.2011.12.003](https://doi.org/10.1016/j.jsb.2011.12.003). (pg. 40)
- [84] Marten L. Chaillet, Gijs van der Schot, Ilja Gubins, Sander Roet, Remco C. Veltkamp, and Friedrich Förster. Extensive Angular Sampling Enables the Sensitive Localization of Macromolecules in Electron Tomograms. *International Journal of Molecular Sciences*, 24(17):13375, January 2023. ISSN 1422-0067. DOI: [10.3390/ijms241713375](https://doi.org/10.3390/ijms241713375). (pg. 40)
- [85] J. M. de la Rosa-Trevín, A. Quintana, L. del Cano, A. Zaldívar, I. Foche, J. Gutiérrez, J. Gómez-Blanco, J. Burguet-Castell, J. Cuenca-Alba, V. Abrishami, J. Vargas, J. Otón, G. Sharov, J. L. Vilas, J. Navas, P. Conesa, M. Kazemi, R. Marabini, C. O. S. Sorzano, and J. M. Carazo. Scipion: A software framework toward integration, reproducibility and validation in 3D electron microscopy. *Journal of Structural Biology*, 195(1): 93–99, July 2016. ISSN 1047-8477. DOI: [10.1016/j.jsb.2016.04.010](https://doi.org/10.1016/j.jsb.2016.04.010). (pg. 41, 136, 147)
- [86] Eric F. Pettersen, Thomas D. Goddard, Conrad C. Huang, Elaine C. Meng, Gregory S. Couch, Tristan I. Croll, John H. Morris, and Thomas E. Ferrin. UCSF ChimeraX: Structure visualization for researchers, educators, and developers. *Protein Sci*, 30 (1):70–82, January 2021. ISSN 1469-896X. DOI: [10.1002/pro.3943](https://doi.org/10.1002/pro.3943). (pg. 41, 57)
- [87] The MathWorks Inc. MATLAB version: 9.13.0 (r2022b). The MathWorks Inc., 2022. (pg. 41)
- [88] Alister Burt, C. Keith Cassidy, Peter Ames, Maria Bacia-Verloop, Meghane Baulard, Karine Huard, Zaida Luthey-Schulten, Ambroise Desfosses, Phillip J. Stansfeld, William Margolin, John S. Parkinson, and Irina Gutsche. Complete structure of the chemosensory array core signalling unit in an *E. coli* minicell strain. *Nat Commun*, 11(1):743, February 2020. ISSN 2041-1723. DOI: [10.1038/s41467-020-14350-9](https://doi.org/10.1038/s41467-020-14350-9). (pg. 45, 47)
- [89] Dask Development Team. *Dask: Library for Dynamic Task Scheduling*, 2016. (pg. 48)

- [90] Thermofisher. Amira Software | Life Science Research - FR. <https://www.thermofisher.com/fr/fr/home/electron-microscopy/products/software-em-3d-vis/amira-software.html>, 1999. (pg. 56)
- [91] Jonathan Schwartz, Chris Harris, Jacob Pietryga, Huihuo Zheng, Prashant Kumar, Anastasiia Visheratina, Nicholas A. Kotov, Brianna Major, Patrick Avery, Peter Ercius, Utkarsh Ayachit, Berk Geveci, David A. Muller, Alessandro Genova, Yi Jiang, Marcus Hanwell, and Robert Hovden. Real-time 3D analysis during electron tomography using tomviz. *Nat Commun*, 13(1):4458, August 2022. ISSN 2041-1723. DOI: [10.1038/s41467-022-32046-0](https://doi.org/10.1038/s41467-022-32046-0). (pg. 57)
- [92] Utz H. Ermel, Serena M. Arghittu, and Achilleas S. Frangakis. ArtiaX: An electron tomography toolbox for the interactive handling of sub-tomograms in UCSF ChimeraX. *Protein Science*, 31(12):e4472, 2022. ISSN 1469-896X. DOI: [10.1002/pro.4472](https://doi.org/10.1002/pro.4472). (pg. 57, 137, 140, 147)
- [93] Dmitry Tegunov. Dtegunov/membranorama, February 2024. (pg. 57, 130)
- [94] Wojciech Wietrzynski, Mirosława Schaffer, Dimitry Tegunov, Sahradha Albert, Atsuko Kanazawa, Jürgen M Plitzko, Wolfgang Baumeister, and Benjamin D Engel. Charting the native architecture of Chlamydomonas thylakoid membranes with single-molecule precision. *eLife*, 9:e53740, April 2020. ISSN 2050-084X. DOI: [10.7554/elife.53740](https://doi.org/10.7554/elife.53740). (pg. 57)
- [95] Antonio Martinez-Sanchez, Inmaculada Garcia, Shoh Asano, Vladan Lucic, and Jose-Jesus Fernandez. Robust membrane detection based on tensor voting for electron tomography. *Journal of Structural Biology*, 186(1):49–61, April 2014. ISSN 1047-8477. DOI: [10.1016/j.jsb.2014.02.015](https://doi.org/10.1016/j.jsb.2014.02.015). (pg. 58)
- [96] Lorenz Lamm, Ricardo D. Righetto, Wojciech Wietrzynski, Matthias Pöge, Antonio Martinez-Sánchez, Tingying Peng, and Benjamin D. Engel. MemBrain: A Deep Learning-aided Pipeline for Automated Detection of Membrane Proteins in Cryo-electron Tomograms, March 2022. (pg. 58)
- [97] Lorenz Lamm, Simon Zufferey, Ricardo D. Righetto, Wojciech Wietrzynski, Kevin A. Yamauchi, Alister Burt, Ye Liu, Hanyi Zhang, Antonio Martinez-Sánchez, Sebastian Ziegler, Fabian Isensee, Julia A. Schnabel, Benjamin D. Engel, and Tingying Peng. MemBrain v2: An end-to-end tool for the analysis of membranes in cryo-electron tomography, January 2024. (pg. 58, 147)
- [98] Maria Salfer, Javier F. Collado, Wolfgang Baumeister, Rubén Fernández-Busnadio, and Antonio Martínez-Sánchez. Reliable estimation of membrane curvature for

- cryo-electron tomography. *PLOS Computational Biology*, 16(8):e1007962, August 2020. ISSN 1553-7358. DOI: [10.1371/journal.pcbi.1007962](https://doi.org/10.1371/journal.pcbi.1007962). (pg. 58)
- [99] Benjamin A. Barad, Michaela Medina, Daniel Fuentes, R. Luke Wiseman, and Danielle A. Grotjahn. Quantifying organellar ultrastructure in cryo-electron tomography using a surface morphometrics pipeline. *Journal of Cell Biology*, 222(4):e202204093, February 2023. ISSN 0021-9525. DOI: [10.1083/jcb.202204093](https://doi.org/10.1083/jcb.202204093). (pg. 58)
- [100] Kevin A. Yamauchi, Lorenz Lamm, Lorenzo Gaifas, Ricardo D. Righetto, Daniil Litvinov, Benjamin D. Engel, and Kyle Harrington. Surforama: Interactive exploration of volumetric data by leveraging 3D surfaces, June 2024. (pg. 64, 130)
- [101] Lorenzo Gaifas. Waretomo. Zenodo, August 2024. (pg. 65, 128)
- [102] Elizabeth Harry, Leigh Monahan, and Lyndal Thompson. Bacterial Cell Division: The Mechanism and Its Precision. In *International Review of Cytology*, volume 253, pages 27–94. Academic Press, January 2006. DOI: [10.1016/S0074-7696\(06\)53002-5](https://doi.org/10.1016/S0074-7696(06)53002-5). (pg. 68)
- [103] Harold P. Erickson. How bacterial cell division might cheat turgor pressure – a unified mechanism of septal division in Gram-positive and Gram-negative bacteria. *BioEssays*, 39(8):1700045, 2017. ISSN 1521-1878. DOI: [10.1002/bies.201700045](https://doi.org/10.1002/bies.201700045). (pg. 68, 89, 99)
- [104] Paula P. Navarro, Andrea Vettiger, Virly Y. Ananda, Paula Montero Llopis, Christoph Allolio, Thomas G. Bernhardt, and Luke H. Chao. Cell wall synthesis and remodelling dynamics determine division site architecture and cell shape in *Escherichia coli*. *Nat Microbiol*, pages 1–14, September 2022. ISSN 2058-5276. DOI: [10.1038/s41564-022-01210-z](https://doi.org/10.1038/s41564-022-01210-z). (pg. 68, 90)
- [105] Terry J. Beveridge and Valério R. F. Matias. Ultrastructure of Gram-Positive Cell Walls. In *Gram-Positive Pathogens*, chapter 1, pages 3–11. John Wiley & Sons, Ltd, 2006. ISBN 978-1-68367-182-4. DOI: [10.1128/9781555816513.ch1](https://doi.org/10.1128/9781555816513.ch1). (pg. 68)
- [106] Peter Giesbrecht, Thomas Kersten, Heinrich Maidhof, and Jörg Wecke. Staphylococcal Cell Wall: Morphogenesis and Fatal Variations in the Presence of Penicillin. *Microbiology and Molecular Biology Reviews*, 62(4):1371–1414, December 1998. DOI: [10.1128/mmbr.62.4.1371-1414.1998](https://doi.org/10.1128/mmbr.62.4.1371-1414.1998). (pg. 68, 90)
- [107] Valério R. F. Matias and Terry J. Beveridge. Native Cell Wall Organization Shown by Cryo-Electron Microscopy Confirms the Existence of a Periplasmic Space in *Staphylococcus aureus*. *Journal of Bacteriology*, 188(3):1011–1021, February 2006. DOI: [10.1128/jb.188.3.1011-1021.2006](https://doi.org/10.1128/jb.188.3.1011-1021.2006). (pg. 68)

- [108] Valério R. F. Matias and Terry J. Beveridge. Cryo-electron microscopy of cell division in *Staphylococcus aureus* reveals a mid-zone between nascent cross walls. *Molecular Microbiology*, 64(1):195–206, 2007. ISSN 1365-2958. DOI: [10.1111/j.1365-2958.2007.05634.x](https://doi.org/10.1111/j.1365-2958.2007.05634.x). (pg. 68, 90)
- [109] Benoît Zuber, Marisa Haenni, Tânia Ribeiro, Kathrin Minnig, Fátima Lopes, Philippe Moreillon, and Jacques Dubochet. Granular Layer in the Periplasmic Space of Gram-Positive Bacteria and Fine Structures of *Enterococcus gallinarum* and *Streptococcus gordonii* Septa Revealed by Cryo-Electron Microscopy of Vitreous Sections. *Journal of Bacteriology*, 188(18):6652–6660, September 2006. DOI: [10.1128/jb.00391-06](https://doi.org/10.1128/jb.00391-06). (pg. 68)
- [110] Danielle L. Sexton, Steffen Burgold, Andreas Schertel, and Elitza I. Tocheva. Super-resolution confocal cryo-CLEM with cryo-FIB milling for *in situ* imaging of *Deinococcus radiodurans*. *Current Research in Structural Biology*, 4:1–9, January 2022. ISSN 2665-928X. DOI: [10.1016/j.crstbi.2021.12.001](https://doi.org/10.1016/j.crstbi.2021.12.001). (pg. 68, 86, 125)
- [111] R. G. E. Murray, M. Hall, and B. G. Thompson. Cell division in *Deinococcus radiodurans* and a method for displaying septa. *Can. J. Microbiol.*, 29(10):1412–1423, October 1983. ISSN 0008-4166. DOI: [10.1139/m83-217](https://doi.org/10.1139/m83-217). (pg. 68, 69, 70, 91)
- [112] B Westling-Häggström, T Elmros, S Normark, and B Winblad. Growth pattern and cell division in *Neisseria gonorrhoeae*. *Journal of Bacteriology*, 129(1):333–342, January 1977. DOI: [10.1128/jb.129.1.333-342.1977](https://doi.org/10.1128/jb.129.1.333-342.1977). (pg. 68)
- [113] Thomas J. Smith, Steve A. Blackman, and Simon J. Foster. Autolysins of *Bacillus subtilis*: Multiple enzymes with multiple functions. *Microbiology*, 146(2):249–262, 2000. ISSN 1465-2080. DOI: [10.1099/00221287-146-2-249](https://doi.org/10.1099/00221287-146-2-249). (pg. 68)
- [114] João M. Monteiro, Pedro B. Fernandes, Filipa Vaz, Ana R. Pereira, Andreia C. Tavares, Maria T. Ferreira, Pedro M. Pereira, Helena Veiga, Erkin Kuru, Michael S. VanNieuwenhze, Yves V. Brun, Sérgio R. Filipe, and Mariana G. Pinho. Cell shape dynamics during the staphylococcal cell cycle. *Nat Commun*, 6(1):8055, August 2015. ISSN 2041-1723. DOI: [10.1038/ncomms9055](https://doi.org/10.1038/ncomms9055). (pg. 68)
- [115] Xiaoxue Zhou, David K. Halladin, Enrique R. Rojas, Elena F. Koslover, Timothy K. Lee, Kerwyn Casey Huang, and Julie A. Theriot. Mechanical crack propagation drives millisecond daughter cell separation in *Staphylococcus aureus*. *Science*, 348 (6234):574–578, May 2015. DOI: [10.1126/science.aaa1511](https://doi.org/10.1126/science.aaa1511). (pg. 68)
- [116] Xiaoxue Zhou, David K. Halladin, and Julie A. Theriot. Fast Mechanically Driven Daughter Cell Separation Is Widespread in Actinobacteria. *mBio*, 7(4):10.1128/mbio.00952-16, August 2016. DOI: [10.1128/mbio.00952-16](https://doi.org/10.1128/mbio.00952-16). (pg. 68)

- [117] Shambhavi Garde, Pavan Kumar Chodisetti, and Manjula Reddy. Peptidoglycan: Structure, Synthesis, and Regulation. *EcoSal Plus*, 9(2):ecosalplus.ESP-0010–2020, December 2021. ISSN 2324-6200. DOI: [10.1128/ecosalplus.ESP-0010-2020](https://doi.org/10.1128/ecosalplus.ESP-0010-2020). (pg. 68)
- [118] Lam T. Nguyen, Catherine M. Oikonomou, H. Jane Ding, Mohammed Kaplan, Qing Yao, Yi-Wei Chang, Morgan Beeby, and Grant J. Jensen. Simulations suggest a constrictive force is required for Gram-negative bacterial cell division. *Nat Commun*, 10(1):1259, March 2019. ISSN 2041-1723. DOI: [10.1038/s41467-019-09264-0](https://doi.org/10.1038/s41467-019-09264-0). (pg. 69)
- [119] André Zapun, Thierry Vernet, and Mariana G. Pinho. The different shapes of cocci. *FEMS Microbiology Reviews*, 32(2):345–360, March 2008. ISSN 0168-6445. DOI: [10.1111/j.1574-6976.2007.00098.x](https://doi.org/10.1111/j.1574-6976.2007.00098.x). (pg. 69)
- [120] Mariana G. Pinho, Morten Kjos, and Jan-Willem Veening. How to get (a)round: Mechanisms controlling growth and division of coccoid bacteria. *Nat Rev Microbiol*, 11(9):601–614, September 2013. ISSN 1740-1534. DOI: [10.1038/nrmicro3088](https://doi.org/10.1038/nrmicro3088). (pg. 69)
- [121] Alexander J. F. Egan, Jeff Errington, and Waldemar Vollmer. Regulation of peptidoglycan synthesis and remodelling. *Nat Rev Microbiol*, 18(8):446–460, August 2020. ISSN 1740-1534. DOI: [10.1038/s41579-020-0366-3](https://doi.org/10.1038/s41579-020-0366-3). (pg. 69)
- [122] Alexander J. F. Egan, Robert M. Cleverley, Katharina Peters, Richard J. Lewis, and Waldemar Vollmer. Regulation of bacterial cell wall growth. *The FEBS Journal*, 284 (6):851–867, 2017. ISSN 1742-4658. DOI: [10.1111/febs.13959](https://doi.org/10.1111/febs.13959). (pg. 69)
- [123] Shishen Du and Joe Lutkenhaus. Assembly and activation of the Escherichia coli divisome. *Molecular Microbiology*, 105(2):177–187, 2017. ISSN 1365-2958. DOI: [10.1111/mmi.13696](https://doi.org/10.1111/mmi.13696). (pg. 69)
- [124] Tanneke den Blaauwen, Leendert W Hamoen, and Petra Anne Levin. The divisome at 25: The road ahead. *Current Opinion in Microbiology*, 36:85–94, April 2017. ISSN 1369-5274. DOI: [10.1016/j.mib.2017.01.007](https://doi.org/10.1016/j.mib.2017.01.007). (pg. 69)
- [125] Jennyfer Trouve, André Zapun, Christopher Arthaud, Claire Durmort, Anne Marie Di Guilmi, Bill Söderström, Anais Pelletier, Christophe Grangeasse, Dominique Bourgeois, Yung-Sing Wong, and Cecile Morlot. Nanoscale dynamics of peptidoglycan assembly during the cell cycle of *Streptococcus pneumoniae*. *Current Biology*, 31(13):2844–2856.e6, July 2021. ISSN 0960-9822. DOI: [10.1016/j.cub.2021.04.041](https://doi.org/10.1016/j.cub.2021.04.041). (pg. 69, 80, 90, 96)

- [126] Amilcar J. Perez, Michael J. Boersma, Kevin E. Bruce, Melissa M. Lamanna, Sidney L. Shaw, Ho-Ching T. Tsui, Atsushi Taguchi, Erin E. Carlson, Michael S. Van-Nieuwenhze, and Malcolm E. Winkler. Organization of peptidoglycan synthesis in nodes and separate rings at different stages of cell division of *Streptococcus pneumoniae*. *Molecular Microbiology*, 115(6):1152–1169, 2021. ISSN 1365-2958. DOI: [10.1111/mmi.14659](https://doi.org/10.1111/mmi.14659). (pg. 69)
- [127] Daniel Pérez-Núñez, Romain Briandet, Blandine David, Céline Gautier, Pierre Renault, Bernard Hallet, Pascal Hols, Rut Carballido-López, and Eric Guédon. A new morphogenesis pathway in bacteria: Unbalanced activity of cell wall synthesis machineries leads to coccus-to-rod transition and filamentation in ovococci. *Molecular Microbiology*, 79(3):759–771, 2011. ISSN 1365-2958. DOI: [10.1111/j.1365-2958.2010.07483.x](https://doi.org/10.1111/j.1365-2958.2010.07483.x). (pg. 69, 91)
- [128] Victoria A Lund, Katarzyna Wacnik, Robert D Turner, Bryony E Cotterell, Christa G Walther, Samuel J Fenn, Fabian Grein, Adam JM Wollman, Mark C Leake, Nicolas Olivier, Ashley Cadby, Stéphane Mesnage, Simon Jones, and Simon J Foster. Molecular coordination of *Staphylococcus aureus* cell division. *eLife*, 7:e32057, February 2018. ISSN 2050-084X. DOI: [10.7554/eLife.32057](https://doi.org/10.7554/eLife.32057). (pg. 69, 90)
- [129] Kevin Floc'h, Françoise Lacroix, Pascale Servant, Yung-Sing Wong, Jean-Philippe Kleman, Dominique Bourgeois, and Joanna Timmins. Cell morphology and nucleoid dynamics in dividing *Deinococcus radiodurans*. *Nat Commun*, 10(1):3815, August 2019. ISSN 2041-1723. DOI: [10.1038/s41467-019-11725-5](https://doi.org/10.1038/s41467-019-11725-5). (pg. 70, 80, 90, 112)
- [130] Ksenija Zahradka, Dea Slade, Adriana Bailone, Suzanne Sommer, Dietrich Averbeck, Mirjana Petranovic, Ariel B. Lindner, and Miroslav Radman. Reassembly of shattered chromosomes in *Deinococcus radiodurans*. *Nature*, 443(7111):569–573, October 2006. ISSN 1476-4687. DOI: [10.1038/nature05160](https://doi.org/10.1038/nature05160). (pg. 70)
- [131] Margaret J. Thornley, R. W. Horne, and Audrey M. Glauert. The fine structure of *micrococcus radiodurans*. *Archiv. Mikrobiol.*, 51(3):267–289, September 1965. ISSN 1432-072X. DOI: [10.1007/BF00408143](https://doi.org/10.1007/BF00408143). (pg. 70, 76, 92)
- [132] Andriko von Kügelgen, Sofie van Dorst, Vikram Alva, and Tanmay A. M. Bharat. A multidomain connector links the outer membrane and cell wall in phylogenetically deep-branching bacteria. *Proceedings of the National Academy of Sciences*, 119(33): e2203156119, August 2022. DOI: [10.1073/pnas.2203156119](https://doi.org/10.1073/pnas.2203156119). (pg. 73, 88, 89)
- [133] U. B. Sleytr, M. Kocur, A. M. Glauert, and M. J. Thornley. A study by freeze-etching of the fine structure of *Micrococcus radiodurans*. *Archiv. Mikrobiol.*, 94(1):77–87, March 1973. ISSN 1432-072X. DOI: [10.1007/BF00414079](https://doi.org/10.1007/BF00414079). (pg. 76, 92)

- [134] Henrik Strahl, Frank Bürmann, and Leendert W. Hamoen. The actin homologue MreB organizes the bacterial cell membrane. *Nat Commun*, 5:3442, March 2014. ISSN 2041-1723. DOI: [10.1038/ncomms4442](https://doi.org/10.1038/ncomms4442). (pg. 77)
- [135] Jennyfer Trouve, Oleksandr Glushonkov, and Cecile Morlot. Metabolic biorthogonal labeling and dSTORM imaging of peptidoglycan synthesis in *Streptococcus pneumoniae*. *STAR Protoc*, 2(4):101006, December 2021. ISSN 2666-1667. DOI: [10.1016/j.xpro.2021.101006](https://doi.org/10.1016/j.xpro.2021.101006). (pg. 80, 96)
- [136] Eric Sauvage and Mohammed Terrak. Glycosyltransferases and Transpeptidases/Penicillin-Binding Proteins: Valuable Targets for New Antibacterials. *Antibiotics*, 5(1):12, March 2016. ISSN 2079-6382. DOI: [10.3390/antibiotics5010012](https://doi.org/10.3390/antibiotics5010012). (pg. 83)
- [137] Zhuo Li, Michael J Trimble, Yves V Brun, and Grant J Jensen. The structure of FtsZ filaments in vivo suggests a force-generating role in cell division. *The EMBO Journal*, 26(22):4694–4708, November 2007. ISSN 0261-4189. DOI: [10.1038/sj.emboj.7601895](https://doi.org/10.1038/sj.emboj.7601895). (pg. 88, 117)
- [138] Piotr Szwedziak, Qing Wang, Tanmay A M Bharat, Matthew Tsim, and Jan Löwe. Architecture of the ring formed by the tubulin homologue FtsZ in bacterial cell division. *eLife*, 3:e04601, December 2014. ISSN 2050-084X. DOI: [10.7554/eLife.04601](https://doi.org/10.7554/eLife.04601). (pg. 88, 117)
- [139] Elizabeth Work and Hilary Griffiths. Morphology and Chemistry of Cell Walls of *Micrococcus radiodurans*. *Journal of Bacteriology*, 95(2):641–657, February 1968. DOI: [10.1128/jb.95.2.641-657.1968](https://doi.org/10.1128/jb.95.2.641-657.1968). (pg. 88)
- [140] Heather Rothfuss, Jimmie C. Lara, Amy K. Schmid, and Mary E. Lidstrom. Involvement of the S-layer proteins Hpi and SlpA in the maintenance of cell envelope integrity in *Deinococcus radiodurans* R1. *Microbiology*, 152(9):2779–2787, 2006. ISSN 1465-2080. DOI: [10.1099/mic.0.28971-0](https://doi.org/10.1099/mic.0.28971-0). (pg. 88)
- [141] Andriko von Kügelgen, Sofie van Dorst, Keitaro Yamashita, Danielle L. Sexton, Elitza I. Tocheva, Garib Murshudov, Vikram Alva, and Tanmay A. M. Bharat. Interdigitated immunoglobulin arrays form the hyperstable surface layer of the extremophilic bacterium *Deinococcus radiodurans*. *Proceedings of the National Academy of Sciences*, 120(16):e2215808120, April 2023. DOI: [10.1073/pnas.2215808120](https://doi.org/10.1073/pnas.2215808120). (pg. 88, 89)
- [142] Domenica Farci, André T. Graça, Luca Iesu, Daniele de Sanctis, and Dario Piano. The SDBC is active in quenching oxidative conditions and bridges the cell envelope

- layers in *Deinococcus radiodurans*. *Journal of Biological Chemistry*, 299(1), January 2023. ISSN 0021-9258, 1083-351X. DOI: [10.1016/j.jbc.2022.102784](https://doi.org/10.1016/j.jbc.2022.102784). (pg. 88)
- [143] Domenica Farci, Patrycja Haniewicz, and Dario Piano. The structured organization of *Deinococcus radiodurans*' cell envelope. *Proceedings of the National Academy of Sciences*, 119(45):e2209111119, November 2022. DOI: [10.1073/pnas.2209111119](https://doi.org/10.1073/pnas.2209111119). (pg. 88)
- [144] Domenica Farci, Patrycja Haniewicz, Daniele de Sanctis, Luca Iesu, Sami Kereïche, Mathias Winterhalter, and Dario Piano. The cryo-EM structure of the S-layer deinoxanthin-binding complex of *Deinococcus radiodurans* informs properties of its environmental interactions. *Journal of Biological Chemistry*, 298(6), June 2022. ISSN 0021-9258, 1083-351X. DOI: [10.1016/j.jbc.2022.102031](https://doi.org/10.1016/j.jbc.2022.102031). (pg. 88)
- [145] Domenica Farci, Sami Kereïche, Sushil Pargani, Patrycja Haniewicz, Igor V. Bodrenko, Matteo Ceccarelli, Mathias Winterhalter, and Dario Piano. Structural analysis of the architecture and in situ localization of the main S-layer complex in *Deinococcus radiodurans*. *Structure*, 29(11):1279–1285.e3, November 2021. ISSN 0969-2126. DOI: [10.1016/j.str.2021.06.014](https://doi.org/10.1016/j.str.2021.06.014). (pg. 88)
- [146] W. Baumeister, M. Barth, R. Hegerl, R. Guckenberger, M. Hahn, and W. O. Saxton. Three-dimensional structure of the regular surface layer (HPI layer) of *Deinococcus radiodurans*. *Journal of Molecular Biology*, 187(2):241–250, January 1986. ISSN 0022-2836. DOI: [10.1016/0022-2836\(86\)90231-7](https://doi.org/10.1016/0022-2836(86)90231-7). (pg. 88)
- [147] W. Baumeister, O. Kübler, and H. P. Zingsheim. The structure of the cell envelope of *Micrococcus radiodurans* as revealed by metal shadowing and decoration. *Journal of Ultrastructure Research*, 75(1):60–71, April 1981. ISSN 0022-5320. DOI: [10.1016/S0022-5320\(81\)80100-1](https://doi.org/10.1016/S0022-5320(81)80100-1). (pg. 88)
- [148] Radhey S. Gupta. Origin of diderm (Gram-negative) bacteria: Antibiotic selection pressure rather than endosymbiosis likely led to the evolution of bacterial cells with two membranes. *Antonie van Leeuwenhoek*, 100(2):171–182, August 2011. ISSN 1572-9699. DOI: [10.1007/s10482-011-9616-8](https://doi.org/10.1007/s10482-011-9616-8). (pg. 89)
- [149] Aurore Vermassen, Sabine Leroy, Régine Talon, Christian Provot, Magdalena Popowska, and Mickaël Desvaux. Cell Wall Hydrolases in Bacteria: Insight on the Diversity of Cell Wall Amidases, Glycosidases and Peptidases Toward Peptidoglycan. *Front Microbiol*, 10:331, 2019. ISSN 1664-302X. DOI: [10.3389/fmicb.2019.00331](https://doi.org/10.3389/fmicb.2019.00331). (pg. 89)
- [150] Sandra P. Santos, Yang Yang, Margarida T. G. Rosa, Mafalda A. A. Rodrigues, Claire Bouthier De La Tour, Suzanne Sommer, Miguel Teixeira, Maria A. Carrondo,

- Peter Cloetens, Isabel A. Abreu, and Célia V. Romão. The interplay between Mn and Fe in *Deinococcus radiodurans* triggers cellular protection during paraquat-induced oxidative stress. *Sci Rep*, 9(1):17217, November 2019. ISSN 2045-2322. DOI: [10.1038/s41598-019-53140-2](https://doi.org/10.1038/s41598-019-53140-2). (pg. 89)
- [151] Adrian D. Land, Ho-Ching T. Tsui, Ozden Kocaoglu, Stephen A. Vella, Sidney L. Shaw, Susan K. Keen, Lok-To Sham, Erin E. Carlson, and Malcolm E. Winkler. Requirement of essential Pbp2x and GpsB for septal ring closure in *Streptococcus pneumoniae* D39. *Mol Microbiol*, 90(5):939–955, December 2013. ISSN 1365-2958. DOI: [10.1111/mmi.12408](https://doi.org/10.1111/mmi.12408). (pg. 91)
- [152] Ozden Kocaoglu, Ho-Ching T. Tsui, Malcolm E. Winkler, and Erin E. Carlson. Profiling of  $\beta$ -lactam selectivity for penicillin-binding proteins in *Streptococcus pneumoniae* D39. *Antimicrob Agents Chemother*, 59(6):3548–3555, 2015. ISSN 1098-6596. DOI: [10.1128/AAC.05142-14](https://doi.org/10.1128/AAC.05142-14). (pg. 91)
- [153] André Zapun, Carlos Contreras-Martel, and Thierry Vernet. Penicillin-binding proteins and beta-lactam resistance. *FEMS Microbiol Rev*, 32(2):361–385, March 2008. ISSN 0168-6445. DOI: [10.1111/j.1574-6976.2007.00095.x](https://doi.org/10.1111/j.1574-6976.2007.00095.x). (pg. 91)
- [154] Atsushi SUGANUMA. Studies on the Fine Structure of *Staphylococcus aureus*. *Journal of Electron Microscopy*, 15(4):257–261, January 1966. ISSN 0022-0744. DOI: [10.1093/oxfordjournals.jmicro.a049532](https://doi.org/10.1093/oxfordjournals.jmicro.a049532). (pg. 92)
- [155] R. D. Pontefract, G. Bergeron, and F. S. Thatcher. Mesosomes in *Escherichia coli*. *Journal of Bacteriology*, 97(1):367–375, January 1969. DOI: [10.1128/jb.97.1.367-375.1969](https://doi.org/10.1128/jb.97.1.367-375.1969). (pg. 92)
- [156] A Ryter. Contribution of new cryomethods to a better knowledge of bacterial anatomy. *Annales de l'Institut Pasteur / Microbiologie*, 139(1):33–44, January 1988. ISSN 0769-2609. DOI: [10.1016/0769-2609\(88\)90095-6](https://doi.org/10.1016/0769-2609(88)90095-6). (pg. 92)
- [157] J Dubochet, A W McDowall, B Menge, E N Schmid, and K G Lickfeld. Electron microscopy of frozen-hydrated bacteria. *Journal of Bacteriology*, 155(1):381–390, July 1983. DOI: [10.1128/jb.155.1.381-390.1983](https://doi.org/10.1128/jb.155.1.381-390.1983). (pg. 92)
- [158] Janine Liedtke, Jamie S. Depelteau, and Ariane Briegel. How advances in cryo-electron tomography have contributed to our current view of bacterial cell biology. *Journal of Structural Biology: X*, 6:100065, January 2022. ISSN 2590-1524. DOI: [10.1016/j.jsbx.2022.100065](https://doi.org/10.1016/j.jsbx.2022.100065). (pg. 92)
- [159] Jordan M. Barrows and Erin D. Goley. FtsZ dynamics in bacterial division: What, how, and why? *Current Opinion in Cell Biology*, 68:163–172, February 2021. ISSN 0955-0674. DOI: [10.1016/j.ceb.2020.10.013](https://doi.org/10.1016/j.ceb.2020.10.013). (pg. 93, 116, 118)

- [160] Ryan McQuillen and Jie Xiao. Insights into the Structure, Function, and Dynamics of the Bacterial Cytokinetic FtsZ-Ring. *Annual Review of Biophysics*, 49(Volume 49, 2020):309–341, May 2020. ISSN 1936-122X, 1936-1238. DOI: [10.1146/annurev-biophys-121219-081703](https://doi.org/10.1146/annurev-biophys-121219-081703). (pg. 93, 116, 125)
- [161] Todd A. Cameron and William Margolin. Insights into the assembly and regulation of the bacterial divisome. *Nat Rev Microbiol*, 22(1):33–45, January 2024. ISSN 1740-1534. DOI: [10.1038/s41579-023-00942-x](https://doi.org/10.1038/s41579-023-00942-x). (pg. 93)
- [162] Pierre Vauclare, Jip Wulffelé, Françoise Lacroix, Pascale Servant, Fabrice Con-falonieri, Jean-Philippe Kleman, Dominique Bourgeois, and Joanna Timmins. Stress-induced nucleoid remodeling in *Deinococcus radiodurans* is associated with major changes in Heat Unstable (HU) protein dynamics. *Nucleic Acids Research*, 52(11): 6406–6423, June 2024. ISSN 0305-1048. DOI: [10.1093/nar/gkae379](https://doi.org/10.1093/nar/gkae379). (pg. 94)
- [163] Martin Ovesný, Pavel Křížek, Josef Borkovec, Zdeněk Svindrych, and Guy M. Hagen. ThunderSTORM: A comprehensive ImageJ plug-in for PALM and STORM data analysis and super-resolution imaging. *Bioinformatics*, 30(16):2389–2390, August 2014. ISSN 1367-4811. DOI: [10.1093/bioinformatics/btu202](https://doi.org/10.1093/bioinformatics/btu202). (pg. 98)
- [164] Johannes Schindelin, Ignacio Arganda-Carreras, Erwin Frise, Verena Kaynig, Mark Longair, Tobias Pietzsch, Stephan Preibisch, Curtis Rueden, Stephan Saalfeld, Benjamin Schmid, Jean-Yves Tinevez, Daniel James White, Volker Hartenstein, Kevin Eliceiri, Pavel Tomancak, and Albert Cardona. Fiji: An open-source platform for biological-image analysis. *Nat Methods*, 9(7):676–682, June 2012. ISSN 1548-7105. DOI: [10.1038/nmeth.2019](https://doi.org/10.1038/nmeth.2019). (pg. 98, 100)
- [165] Cécilia Hognon, Simon Garaude, Joanna Timmins, Christophe Chipot, François Dehez, and Antonio Monari. Molecular Bases of DNA Packaging in Bacteria Revealed by All-Atom Molecular Dynamics Simulations: The Case of Histone-Like Proteins in *Borrelia burgdorferi*. *J. Phys. Chem. Lett.*, 10(22):7200–7207, November 2019. DOI: [10.1021/acs.jpclett.9b02978](https://doi.org/10.1021/acs.jpclett.9b02978). (pg. 111, 112)
- [166] Michal Hammel, Dhar Amlanjyoti, Francis E. Reyes, Jian-Hua Chen, Rochelle Parpana, Henry Y. H. Tang, Carolyn A. Larabell, John A. Tainer, and Sankar Adhya. HU multimerization shift controls nucleoid compaction. *Sci. Adv.*, 2(7):e1600650, July 2016. ISSN 2375-2548. DOI: [10.1126/sciadv.1600650](https://doi.org/10.1126/sciadv.1600650). (pg. 112)
- [167] Maria A. Oliva, Suzanne C. Cordell, and Jan Löwe. Structural insights into FtsZ protofilament formation. *Nat Struct Mol Biol*, 11(12):1243–1250, December 2004. ISSN 1545-9985. DOI: [10.1038/nsmb855](https://doi.org/10.1038/nsmb855). (pg. 116, 117)

- [168] Martin Loose and Timothy J. Mitchison. The bacterial cell division proteins FtsA and FtsZ self-organize into dynamic cytoskeletal patterns. *Nat Cell Biol*, 16(1): 38–46, January 2014. ISSN 1476-4679. DOI: [10.1038/ncb2885](https://doi.org/10.1038/ncb2885). (pg. 117)
- [169] Alexandre W. Bisson-Filho, Yen-Pang Hsu, Georgia R. Squyres, Erkin Kuru, Fabai Wu, Calum Jukes, Yingjie Sun, Cees Dekker, Seamus Holden, Michael S. VanNieuwenhze, Yves V. Brun, and Ethan C. Garner. Treadmilling by FtsZ filaments drives peptidoglycan synthesis and bacterial cell division. *Science*, 355(6326): 739–743, February 2017. DOI: [10.1126/science.aak9973](https://doi.org/10.1126/science.aak9973). (pg. 117)
- [170] Natalia Baranova, Philipp Radler, Víctor M. Hernández-Rocamora, Carlos Alfonso, Mar López-Pelegrín, Germán Rivas, Waldemar Vollmer, and Martin Loose. Diffusion and capture permits dynamic coupling between treadmilling FtsZ filaments and cell division proteins. *Nat Microbiol*, 5(3):407–417, March 2020. ISSN 2058-5276. DOI: [10.1038/s41564-019-0657-5](https://doi.org/10.1038/s41564-019-0657-5). (pg. 117)
- [171] João M. Monteiro, Ana R. Pereira, Nathalie T. Reichmann, Bruno M. Saraiva, Pedro B. Fernandes, Helena Veiga, Andreia C. Tavares, Margarida Santos, Maria T. Ferreira, Vânia Macário, Michael S. VanNieuwenhze, Sérgio R. Filipe, and Marianna G. Pinho. Peptidoglycan synthesis drives an FtsZ-treadmilling-independent step of cytokinesis. *Nature*, 554(7693):528–532, February 2018. ISSN 1476-4687. DOI: [10.1038/nature25506](https://doi.org/10.1038/nature25506). (pg. 117)
- [172] Xinxing Yang, Zhixin Lyu, Amanda Miguel, Ryan McQuillen, Kerwyn Casey Huang, and Jie Xiao. GTPase activity–coupled treadmilling of the bacterial tubulin FtsZ organizes septal cell wall synthesis. *Science*, 355(6326):744–747, February 2017. DOI: [10.1126/science.aak9995](https://doi.org/10.1126/science.aak9995). (pg. 118)
- [173] Matthew A. Gerding, Yasuyuki Ogata, Nicole D. Pecora, Hironori Niki, and Piet A. J. De Boer. The trans-envelope Tol–Pal complex is part of the cell division machinery and required for proper outer-membrane invagination during cell constriction in *E. coli*. *Molecular Microbiology*, 63(4):1008–1025, 2007. ISSN 1365-2958. DOI: [10.1111/j.1365-2958.2006.05571.x](https://doi.org/10.1111/j.1365-2958.2006.05571.x). (pg. 118)
- [174] Junso Fujita, Hiroshi Amesaka, Takuya Yoshizawa, Kota Hibino, Natsuki Kamimura, Natsuko Kuroda, Takamoto Konishi, Yuki Kato, Mizuho Hara, Tsuyoshi Inoue, Keiichi Namba, Shun-ichi Tanaka, and Hiroyoshi Matsumura. Structures of a FtsZ single protofilament and a double-helical tube in complex with a monobody. *Nat Commun*, 14(1):4073, July 2023. ISSN 2041-1723. DOI: [10.1038/s41467-023-39807-5](https://doi.org/10.1038/s41467-023-39807-5). (pg. 120, 143)
- [175] Yong Zi Tan, Philip R. Baldwin, Joseph H. Davis, James R. Williamson, Clinton S. Potter, Bridget Carragher, and Dmitry Lyumkis. Addressing preferred specimen

- orientation in single-particle cryo-EM through tilting. *Nat Methods*, 14(8):793–796, August 2017. ISSN 1548-7105. DOI: [10.1038/nmeth.4347](https://doi.org/10.1038/nmeth.4347). (pg. 121)
- [176] Lorenzo Gaifas. Blik: A Python tool for visualising and interacting with cryo-ET and subtomogram averaging data. Zenodo, March 2024. (pg. 126)
- [177] Lorenzo Gaifas. Napari-properties-plotter, September 2021. (pg. 126)
- [178] The wwPDB Consortium. EMDB—the Electron Microscopy Data Bank. *Nucleic Acids Research*, 52(D1):D456–D465, January 2024. ISSN 0305-1048. DOI: [10.1093/nar/gkad1019](https://doi.org/10.1093/nar/gkad1019). (pg. 129)
- [179] Artan Kaso. Computation of the normalized cross-correlation by fast Fourier transform. *PLOS ONE*, 13(9):e0203434, September 2018. ISSN 1932-6203. DOI: [10.1371/journal.pone.0203434](https://doi.org/10.1371/journal.pone.0203434). (pg. 130)
- [180] Zhizhen Zhao and Amit Singer. Fourier–Bessel rotational invariant eigenimages. *J. Opt. Soc. Am. A*, 30(5):871, May 2013. ISSN 1084-7529, 1520-8532. DOI: [10.1364/JOSAA.30.000871](https://doi.org/10.1364/JOSAA.30.000871). (pg. 130)
- [181] José María Almira, Harold Phelippeau, and Antonio Martinez-Sánchez. Fast normalized cross-correlation for template matching with rotations. *J. Appl. Math. Comput.*, June 2024. ISSN 1865-2085. DOI: [10.1007/s12190-024-02157-6](https://doi.org/10.1007/s12190-024-02157-6). (pg. 130)
- [182] Andrew Morin, Ben Eisenbraun, Jason Key, Paul C. Sanschagrin, Michael A. Timony, Michelle Ottaviano, and Piotr Sliz. Cutting Edge: Collaboration gets the most out of software. <https://elifesciences.org/articles/01456>, September 2013. (pg. 131)
- [183] Lorenzo Gaifas. Cs2star.py, November 2021. (pg. 131)
- [184] The napari Community. Community — napari. <https://napari.org/stable/community/index.html>, 2024. (pg. 141)
- [185] Kotaro Kelley, Ashleigh M. Raczkowski, Oleg Klykov, Pattana Jaroenlak, Daija Bobe, Mykhailo Kopylov, Edward T. Eng, Gira Bhabha, Clinton S. Potter, Bridget Carragher, and Alex J. Noble. Waffle Method: A general and flexible approach for improving throughput in FIB-milling. *Nat Commun*, 13(1):1857, April 2022. ISSN 2041-1723. DOI: [10.1038/s41467-022-29501-3](https://doi.org/10.1038/s41467-022-29501-3). (pg. 145)
- [186] Marit de Beer, Deniz Daviran, Rona Roverts, Luco Rutten, Elena Macías-Sánchez, Juriaan R. Metz, Nico Sommerdijk, and Anat Akiva. Precise targeting for 3D cryo-correlative light and electron microscopy volume imaging of tissues using a Finder-TOP. *Commun Biol*, 6(1):1–9, May 2023. ISSN 2399-3642. DOI: [10.1038/s42003-023-04887-y](https://doi.org/10.1038/s42003-023-04887-y). (pg. 146)

- [187] Sven Klumpe, Herman KH Fung, Sara K Goetz, Ievgeniia Zagoriy, Bernhard Ham-pelz, Xiaojie Zhang, Philipp S Erdmann, Janina Baumbach, Christoph W Müller, Martin Beck, Jürgen M Plitzko, and Julia Mahamid. A modular platform for automated cryo-FIB workflows. *eLife*, 10:e70506, December 2021. ISSN 2050-084X. DOI: [10.7554/eLife.70506](https://doi.org/10.7554/eLife.70506). (pg. 146)
- [188] K. Naydenova, G. McMullan, M. J. Peet, Y. Lee, P. C. Edwards, S. Chen, E. Leahy, S. Scotcher, R. Henderson, and C. J. Russo. CryoEM at 100 keV: A demonstration and prospects. *IUCrJ*, 6(6):1086–1098, November 2019. ISSN 2052-2525. DOI: [10.1107/S2052252519012612](https://doi.org/10.1107/S2052252519012612). (pg. 146)
- [189] Nikita Balyschew, Artsemi Yushkevich, Vasilii Mikirtumov, Ricardo M. Sanchez, Thiemo Sprink, and Mikhail Kudryashev. Streamlined structure determination by cryo-electron tomography and subtomogram averaging using TomoBEAR. *Nat Commun*, 14(1):6543, October 2023. ISSN 2041-1723. DOI: [10.1038/s41467-023-42085-w](https://doi.org/10.1038/s41467-023-42085-w). (pg. 147)
- [190] Hsuan-Fu Liu, Ye Zhou, Qinwen Huang, Jonathan Piland, Weisheng Jin, Justin Mandel, Xiaochen Du, Jeffrey Martin, and Alberto Bartesaghi. nextPYP: A comprehensive and scalable platform for characterizing protein variability in situ using single-particle cryo-electron tomography. *Nat Methods*, 20(12):1909–1919, December 2023. ISSN 1548-7105. DOI: [10.1038/s41592-023-02045-0](https://doi.org/10.1038/s41592-023-02045-0). (pg. 147)
- [191] Fabian Eisenstein, Yoshiyuki Fukuda, and Radostin Danev. Smart parallel automated cryo-electron tomography. *Nat Methods*, pages 1–4, August 2024. ISSN 1548-7105. DOI: [10.1038/s41592-024-02373-9](https://doi.org/10.1038/s41592-024-02373-9). (pg. 147)
- [192] Joshua Maynez, Shashi Narayan, Bernd Bohnet, and Ryan McDonald. On Faithfulness and Factuality in Abstractive Summarization, May 2020. Comment: ACL 2020, 14 pages. (pg. 147)
- [193] Tyler M. Earnest, Reika Watanabe, John E. Stone, Julia Mahamid, Wolfgang Baumeister, Elizabeth Villa, and Zaida Luthey-Schulten. Challenges of Integrating Stochastic Dynamics and Cryo-Electron Tomograms in Whole-Cell Simulations. *J. Phys. Chem. B*, 121(15):3871–3881, April 2017. ISSN 1520-6106. DOI: [10.1021/acs.jpcb.7b00672](https://doi.org/10.1021/acs.jpcb.7b00672). (pg. 148)
- [194] Rémi Vuillemot, Isabelle Rouiller, and Slavica Jonić. MDTOMO method for continuous conformational variability analysis in cryo electron subtomograms based on molecular dynamics simulations. *Sci Rep*, 13(1):10596, June 2023. ISSN 2045-2322. DOI: [10.1038/s41598-023-37037-9](https://doi.org/10.1038/s41598-023-37037-9). (pg. 148)

- [195] Fengyu Li, Yuwei Zhang, Fei Xia, and Xin Xu. Development of multiscale ultra-coarse-grained models for the SARS-CoV-2 virion from cryo-electron microscopy data. *Phys. Chem. Chem. Phys.*, 25(18):12882–12890, May 2023. ISSN 1463-9084.  
DOI: [10.1039/D3CP00093A](https://doi.org/10.1039/D3CP00093A). (pg. 148)

## END NOTE

The code used to generate figures (where applicable), the figures themselves, and the  $\text{\LaTeX}$  source code for this manuscript are all available at <https://github.com/brisvag/thesis/>.

Much of the software mentioned in this thesis (and more) can be found at <https://github.com/brisvag/> under open-source licenses.